OREGON HEALTH & SCIENCE UNIVERSITY
SCHOOL OF MEDICINE - GRADUATE STUDIES

PANRETINAL OPTICAL COHERENCE TOMOGRAPHY

by

Shuibin Ni

A DISSERTATION
Presented to the Department of Biomedical Engineering
of the Oregon Health & Science University
School of Medicine
in partial fulfillment of
the requirement for the degree of Doctor of Philosophy

September 2024

TABLE OF CONTENTS

LIST OF FIGURES

LIST OF TABLES

LIST OF ABBREVIATIONS

AL	Axial Length
AMD	Age-related Macular Degeneration
AR	Anti-Reflection
CCD	Charge-coupled Device
CPAP	Continuous Positive Airway Pressure
CR-OCT	Circular-Ranging Optical Coherence Tomography
DR	Diabetic Retinopathy
ERD	Exudative Retinal Detachment
FD-OCT	Fourier-Domain Optical Coherence Tomography
FDML	Fourier Domain Mode Locking
FOV	Field of View
GPU	Graphics Processing Unit
ILM	Internal Limiting Membrane
IP	Incontinentia Pigmenti
MEMS	Micro-electromechanical Systems
MRI	Magnetic Resonance Imaging
NA	Numerical Aperture
NICU	Neonatal Intensive Care Unit
OCT	Optical Coherence Tomography
OCTA	Optical Coherence Tomography Angiography
OPL	Optical Path Length
OR	Operating Room
PPV	Pars Plana Vitrectomy
PSF	Point Spread Function
PV	Peak-to-valley
RD	Retinal Detachment
RMS	Root Mean Square
ROP	Retinopathy of Prematurity
RPE	Retinal Pigment Epithelium
RRD	Rhegmatogenous Retinal Detachment

SD-OCT	Spectral-Domain Optical Coherence Tomography
SLO	Scanning Laser Ophthalmoscope
SNR	Signal-to-Noise Ratio
SPML	Stretched-Pulse Mode-Locked
SS-OCT	Swept-Source Optical Coherence Tomography
TRD	Tractional Retinal Detachment
TD-OCT	Time-Domain Optical Coherence Tomography
UWF	Ultra-widefield
VCSEL	Vertical Cavity Surface Emitting Laser
VEGF	Vascular Endothelial Growth Factor
WDFI	Widefield Digital Fundus Imaging
XLRS	X-linked Retinoschisis

ACKNOWLEDGEMENTS

Completing the PhD study and research has been a long journey, and I would not have been able to reach this milestone without the support and guidance of many individuals.

First and foremost, I would like to express my deepest gratitude to my advisor, Dr. Yifan Jian. Your expertise, patience, and encouragement have been invaluable throughout my research. Your insightful feedback and unwavering support have guided me through the challenges of these research projects and have been crucial in shaping the outcome. Your guidance has helped me to strengthen my skills and deepen my understanding of this area.

I am profoundly grateful to the members of my dissertation advisory committee, Dr. J. Peter Campbell, Dr. Siyu Chen, and Dr. Benjamin K. Young. Dr. Campbell and Dr. Young, as esteemed pediatricians, provided invaluable feedback on the transition of engineering work to clinical applications, thereby strengthening the practical aspects of my research. Dr. Chen, with his extensive scientific expertise, consistently provided valuable suggestions and was highly energetic in conducting experiments. I sincerely thank each of you for your advice and support in developing my dissertation.

Thank you to all the lab members of the Center for Ophthalmic Optics & Laser (COOL Lab) at Casey Eye Institute for your help during my PhD studies. A special thanks to Ringo Ng, Dr. Thanh-Tin P. Nguyen, Dr. Acner Camino, Dr. Xiang Wei, and Dr. Kai Neuhaus; your technical support and intellectual discussions have been a source of inspiration and motivation. I am particularly thankful to Shanjida Khan, Omkar Thaware, Guangru Ben Liang, Yukun Guo, Min Gao, and Siyu Song for your assistance and for making the lab a pleasant place to work. The moments we shared outside of work have been invaluable in maintaining a balanced and enjoyable PhD experience.

Finally, I would like to express my heartfelt thanks to my family. To my family, thank you for your unconditional support all the time. Your belief in me has been a constant source of strength.

This thesis is dedicated to all of you who have helped me along the way. I could not have achieved this without your support and encouragement.

ABSTRACT OF THE DISSERTATION

Optical coherence tomography (OCT) is a crucial tool for ophthalmic diagnosis due to its non-invasive, high-resolution, cross-sectional, and three-dimensional imaging capabilities. Traditional desktop OCT systems, though effective for adults, are unsuitable for infant imaging because of their size, immobility, and difficulty of keeping infants still. Commercially available portable devices for young children also struggle to capture the peripheral retina (70°) and perform OCT angiography (OCTA) due to insufficient speed (32 kHz). Comprehensive visualization of the retina morphology is vital for diagnosing and managing pediatric retinal diseases. This dissertation addresses these challenges by developing and applying advanced handheld OCT and OCTA systems specifically designed for pediatric use. The initial prototype achieved a 400 kHz imaging speed and a 55° field of view but needed improvements for comprehensive peripheral retinal visualization. Subsequent iterations expanded the field of view to 105° and 140°, introduced custom optics for enhanced performance, and adopted a contact approach to solve alignment issues. The approach provided superior image quality, reduced alignment time, and increased success rates, especially suitable for infant imaging. The latest prototype features a custom-designed lens group and two aspherical lenses, delivering superior image quality and enabling implement panretinal OCTA in pediatric retinal imaging. These prototypes have proven effective in diagnosing and monitoring pediatric retinal diseases such as retinopathy of prematurity, retinoblastoma, Coats disease, retinal detachment, *etc.* This work underscores the potential of these systems to advance pediatric ophthalmology and expand the capabilities of retinal imaging.

CHAPTER 1. INTRODUCTION

1.1 Overview

Childhood blindness remains a significant global health issue, with retinopathy of prematurity (ROP) being one of the leading causes. Despite the severe consequences, nearly all cases of ROP-related blindness can be prevented with timely diagnosis and treatment [1–4]. Traditionally, the ophthalmoscopic exam has been the gold standard for diagnosing ROP. However, this method is highly challenging and subjective, leading to inconsistent and sometimes adverse outcomes. Figure 1.1 illustrates the method of clinical documentation and the range of pathology observed in ROP. The subjective nature of ophthalmoscopic exams can result in two main issues: premature treatment, which exposes infants to the risks and morbidity associated with interventions such as laser therapy (which can cause high myopia, late retinal detachment, amblyopia, and anesthetic complications), and delayed treatment, which can lead to retinal detachment and blindness.

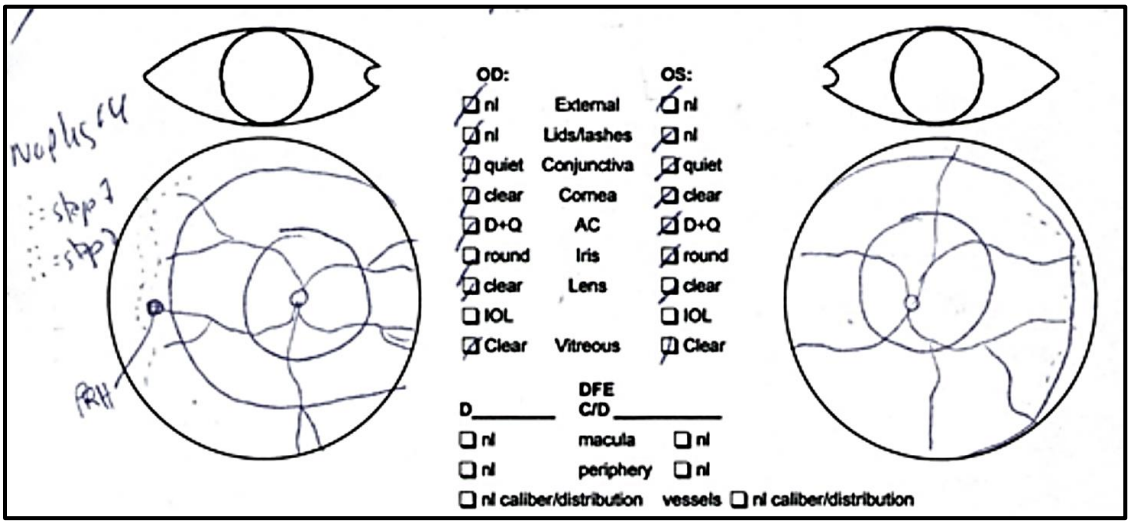

Figure 1.1 Clinical documentation (fundus drawing) derived from indirect ophthalmoscopy.

Early detection and intervention are critical in preserving vision and preventing blindness in ROP patients. Current imaging techniques, such as indirect ophthalmoscopy and fundus cameras, have limitations including prolonged imaging times, low resolution, and restricted field of view. In contrast, optical coherence tomography (OCT), a non-invasive, high-speed, and micrometer-scale imaging technique, offers significant promise in addressing these challenges [5]. Several important lessons from adopting OCT in adult retinal diseases suggest that ultra-widefield OCT/OCT angiography (OCTA) may become essential not only for ROP but for all pediatric retinal diseases in the future. (1) OCT surpasses ophthalmoscopic exams in diagnosing macular disease and has refined the classification of diseases such as age-related macular degeneration (AMD) and diabetic retinopathy (DR), the two leading causes of vision loss in adults. (2) OCT has demonstrated the ability to detect subclinical disease (not visible on ophthalmoscopy), enabling earlier treatment in both conditions. (3) Quantitative OCT metrics have enabled objective disease monitoring. (4) The development of OCT coincided with a therapeutic shift towards using anti-vascular endothelial growth factor (anti-VEGF) drugs, with OCT being indispensable for monitoring response to treatment and determining retreatment frequency. A similar transition is gradually occurring in ROP, yet monitoring treatment response and disease recurrence remains a pivotal unsolved problem due to the lack of objective disease metrics. Traditional OCT devices are typically bucky, desktop-based systems requiring patients to be positioned in front of the device (Figure 1.2), posing significant challenges when examining young children and infants [6].

Figure 1.2 “Flying baby” position using Heidelberg Spectralis Spectral Domain OCT. Images were obtained with the infant in the “flying baby” position. From reference [6].

To address this issue, several groups have developed handheld OCT prototypes for imaging patients in the supine position [7–16]. The introduction of handheld OCT devices provides a potential solution, enabling clinicians to diagnose pediatric diseases without causing additional discomfort or pain to the patients. However, most of these portable prototypes still have limitations in imaging speed, axial imaging range, and field of view. These limitations restrict their effectiveness in diagnosing ROP.

My PhD research focuses on developing and validating handheld OCT/OCTA imaging systems to enhance the diagnosis of pediatric diseases, particularly ROP. Developing handheld OCT systems with ultrahigh-speed and ultra-widefield capabilities would represent a significant advancement in pediatric ophthalmology. Such a device would enable clinicians to capture larger retinal areas faster, facilitating real-time monitoring of retinal pathologies and enhancing the ability to detect potential issues in difficult-to-reach regions. These innovations could significantly improve the early diagnosis and management of ROP, ultimately reducing the incidence of childhood blindness. This dissertation begins with an introduction to the fundamentals of OCT and

OCTA, establishing the foundation for understanding the significance and potential impact of these advanced imaging technologies in pediatric ophthalmology.

1.2 Optical Coherence Tomography

OCT is a non-invasive imaging technology that utilizes light waves to produce high-resolution, cross-sectional images of biological tissues [5]. Since its inception in the early 1990s, OCT has become an essential diagnostic tool, especially in ophthalmology. This introduction outlines the principles of OCT, its technological advancements, and its ophthalmic applications.

OCT operates on the principle of low-coherence interferometry, which uses light wave interference to create detailed images of tissue structures. The main components of an OCT system are a broadband light source, an interferometer, a detector, and a scanning system. Broadband light sources, like super luminescent diodes (SLDs) or vertical cavity surface emitting laser (VCSEL), provide the coherence length needed for high axial resolution. The interferometer splits the light beam into two paths: one toward the sample and the other toward a reference mirror. Commonly used interferometers in OCT systems include the Michelson interferometer and Mach-Zehnder interferometer. When the reflected light from both paths is recombined, it forms interference patterns that reveal the sample's optical properties. Detectors such as charge-coupled devices (CCDs) and photodiodes convert them into electrical signals, which are processed to generate cross-sectional images. The scanning system moves the light beam across the sample to create two-dimensional (2D) and three-dimensional (3D) images, often using a galvanometer scanner or microelectromechanical systems (MEMS).

Since its development, OCT technology has seen significant advancements, enhancing imaging capabilities and broadening its applications. The first generation, Time-Domain OCT (TD-OCT), used a mechanically scanned reference mirror to create depth profiles (A-scans) of the

sample, as illustrated in Figure 1.3. Combining multiple A-scans produces a 2D cross-sectional image (B-scan). TD-OCT systems achieved axial resolutions of 10-20 µm, suitable for many medical applications but less detailed than later technologies. The mechanical scanning of the reference mirror limited TD-OCT's imaging speed and sensitivity, making it slower and less capable of detecting weak reflections from deeper tissues than subsequent technologies.

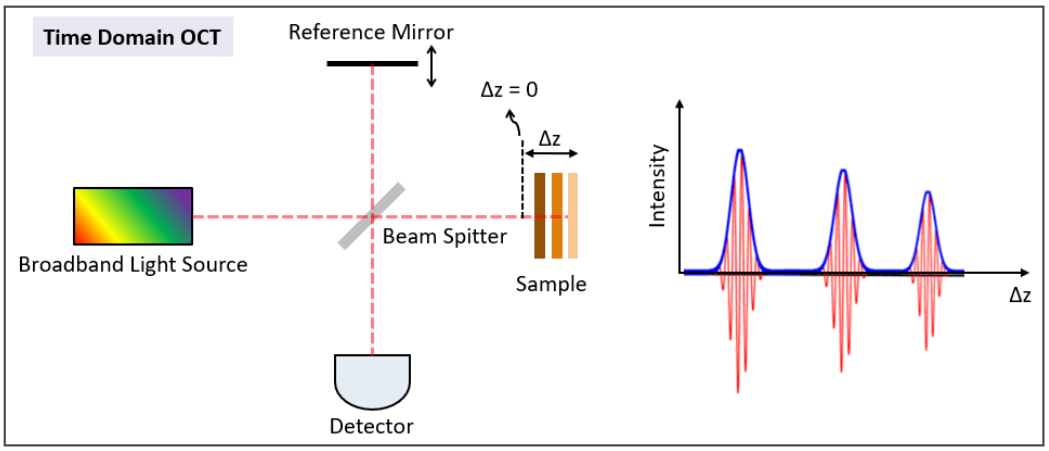

Figure 1.3 Schematic illustration of basic Time-Domain OCT (TD-OCT) setup.

Fourier-Domain OCT (FD-OCT), also known as Spectral-Domain OCT (SD-OCT), marked a major improvement over TD-OCT. FD-OCT employs a stationary reference mirror and a spectrometer to measure the interference spectrum, eliminating the need for mechanical scanning, as illustrated in Figure 1.4(A). This innovation significantly increases acquisition speed and sensitivity. FD-OCT systems typically achieve higher axial resolutions of 5-10 µm, offering more detailed images than TD-OCT. Using a stationary reference mirror and spectrometer-based detection allows FD-OCT to capture images much faster, facilitating real-time imaging. Additionally, FD-OCT's higher sensitivity enables the detection of weak reflections from deeper tissues.

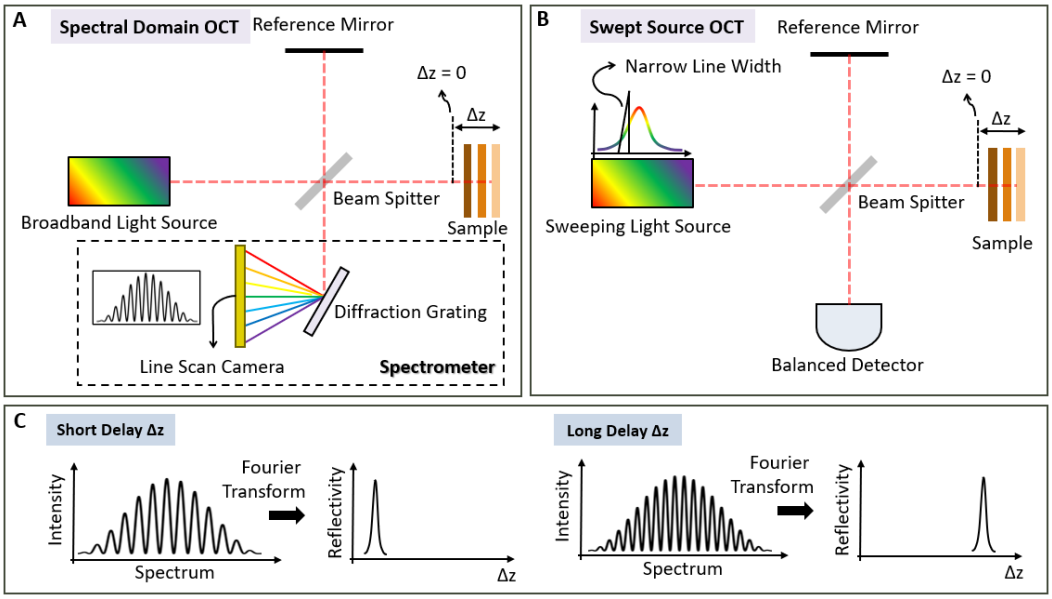

Figure 1.4 Schematic depiction of basic Fourier-Domain OCT. (A) Diagram of Spectral-Domain OCT (SD-OCT). Light backscattered from the sample interferes with reference light following a known path delay, and the resulting spectrum is captured using a spectrometer and line scan camera. (B) Diagram of Swept-Source OCT (SS-OCT). The backscattered light versus delay is measured by Fourier transforming the interferometer detector signal over one frequency sweep, with each sweep producing one A-scan. (C) Delay is represented as different frequency oscillations, and A-scans are obtained by Fourier transforming the spectrum. The A-scan rate in SD-OCT is determined by the camera's readout rate, while in SS-OCT, it is determined by the laser's sweep repetition rate.

Swept-source OCT (SS-OCT) is an FD-OCT variant that uses a tunable laser source to sweep through different wavelengths sequentially, as represented in Figure 1.4(B). SS-OCT provides deeper tissue penetration and faster imaging speeds than SD-OCT, making it suitable for high-speed and deep-tissue imaging applications. SS-OCT systems achieve axial resolutions similar to SD-OCT, around 5-10 µm. The tunable laser source enables SS-OCT to acquire images at even higher speeds, allowing ultrafast imaging. SS-OCT can penetrate deeper into tissues due to its longer wavelength light source, providing detailed images of thicker biological structures. In SS-OCT, the tunable laser source sweeps through a range of wavelengths, detecting the

interference pattern for each one. The data is processed using Fourier transformation to generate depth profiles [Figure 1.4(C)]. The combinations of the high-speed tunable laser and advanced detection techniques allow SS-OCT to capture detailed real-time images of deep tissue structures.

OCT has transformed ophthalmic imaging, offering unparalleled resolution and non-invasive imaging capabilities. From its early development to its advanced state today, OCT has become a vital tool in ophthalmology, providing detailed images of the retina, optic nerve, and other ocular structures. This technology significantly aids in diagnosing and managing various eye conditions.

1.3 Optical Coherence Tomography Angiography

OCTA is an advanced extension of OCT that allows for the visualization of both retinal and choroidal vasculature [17,18]. The technique involves transverse scanning of the optical beam rapid acquisition of A-scans to create a B-scan. Each A-scan captures optical back reflection or backscattering as a function of depth. For stationary structures, repeated measurements at the same retinal location yield identical A-scans. However, blood flow causes temporal variations in back reflection or backscattering, leading to differences in repeated A-scans. If the blood flow speed (ν) or the time interval (Δt) between repeated scans increases, blood cells will move a greater distance, $\Delta L = \nu \times \Delta t$ [Figure 1.5]. These differences, influenced by blood flow speed and scanning intervals, alter the amplitude or phase of the OCT signal. By continuously acquiring B-scans at the same location, OCTA utilizes these temporal changes to generate images. This method requires minimal hardware modifications while preserving the non-invasiveness and depth resolution advantages of OCT.

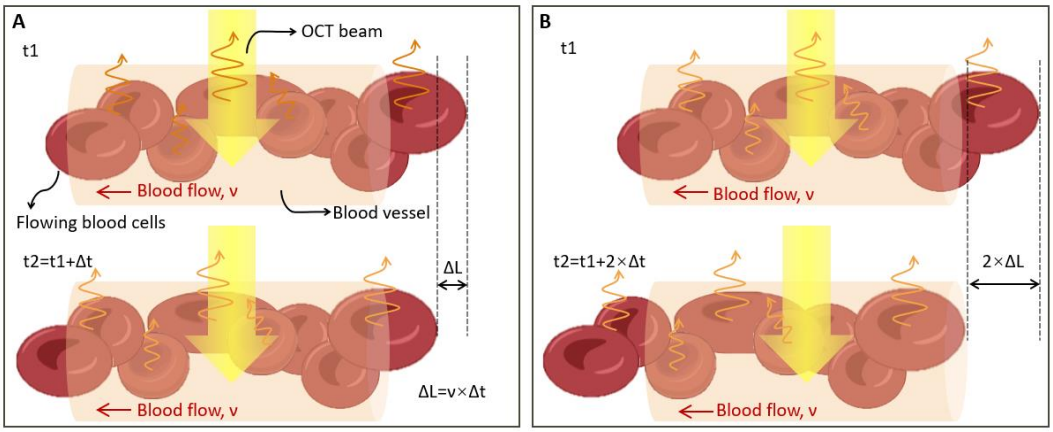

Figure 1.5 Optical coherence tomography angiography motion contrast from blood flow. (A) At t1, an OCT beam (yellow arrow) is directed at a blood vessel with moving blood cells. At t2, a second OCT is performed at the same location. If v represents the blood cell speed and Δt is the interscan time, the cells move a distance $\Delta L = v \times \Delta t$, resulting in a change in OCT signals between t1 and t2. (B) When the interscan time is increased from Δt to 2Δt, the blood cells travel a greater distance. Similarly, doubling the blood cell speed has the same effect as doubling the interscan time.

OCTA operates by repeating B-scans of the same retinal location and using algorithms to detect temporal variations in the OCT signal caused by blood flow. Typically, two to five B-scans are repeated, with the beam moved perpendicularly to image a volume. The acquisition time for a B-scan, or interscan time, is determined by the number of A-scans per B-scan. Eye motion is corrected, and B-scans are compared pixel-by-pixel using algorithms that apply subtraction, division, or decorrelation of OCT amplitude and/or phase. However, OCTA is effectively only strong OCT signals. In low-signal areas such as the vitreous or choroid, noise can create false OCTA signals, which can be masked or thresholded [19]. It is crucial to inspect structural OCT images to ensure sufficient signal strength when interpreting OCTA data.

The interscan time (Δt) is crucial in OCTA. Blood cell speeds (v) in the retinal and choriocapillaris vasculatures range from millimeters per second to tens of millimeters per second.

For example, with a blood cell speed of v=6 mm/s and an interscan time of Δt=3 ms, the displacement is $\Delta L = v \times \Delta t = 6 \times 3 = 18$ μm. Given that the typical OCT beam spot size is around 20 μm, this displacement significantly alters the OCT signal. The interscan time (Δt) depends on the A-scan rate and the number of A-scans per B-scan. Longer interscan times increase sensitivity to blood flow but fail to distinguish faster flows and are more susceptible to eye motion. Conversely, shorter interscan times reduce sensitivity to flow but lessen the impact of eye motion and can differentiate faster flows [20,21]. These factors should be considered when analyzing OCTA data.

OCTA presents several challenges. Contrast derived from B-scan fluctuations can be affected by patient movements or changes in fixation, leading to false OCTA signals. The need for repeated B-scans also extends imaging time. Evaluating angiograms in an *en face* view requires isotropic scanning, which significantly lengthens imaging time compared to structural imaging. Projection artifacts occur when the OCT beam penetrates deeper tissues, passing through superficial tissues twice and causing fluctuations that affect deeper signals [22]. Forward scattering in blood vessels elongates the optical path length, creating contrast outside the vessels and resulting in projection artifacts. These artifacts make superficial vessels appear in deeper tissues, complicating the imaging of the deep capillary plexus or choroidal vasculature.

OCTA is an innovative OCT processing method that creates high-resolution, three-dimensional angiograms by identifying differences between stationary tissues and moving red blood cells in sequential B-scans. Stationary tissues exhibit minimal variance across B-scans, whereas signals from blood vessels fluctuate due to the movement of red blood cells, resulting in higher variances. These variances are highlighted to construct angiograms. The OCT signal consists of amplitude and phase components, both of which can be extracted for the OCTA signal. OCTA algorithms can be categorized as amplitude-based, phase-based, or complex-based.

Amplitude-based techniques, such as speckle variance OCTA (SV-OCTA), utilize only the amplitude component, calculating speckle variations to generate images [23]. Split spectrum amplitude-decorrelation angiography (SSADA), introduced in 2012, enhances OCTA signals by employing a split-spectrum mechanism to suppress bulk motion, producing high-quality images with increased sensitivity to blood flow while reducing motion-induced noise [24]. Phase-variance OCTA (PV-OCTA) relies solely on phase signals, enhancing motion contrast [25]. Complex-based methods incorporate both amplitude and phase components of the OCT signal, allowing for the detection of very slow motion and improving OCTA image quality. Optical microangiography (OMAG) is a complex-based OCTA algorithm that is highly sensitive to capillaries, resulting in high-quality retinal OCTA images [26].

1.4 Outline

The subsequent chapters of this dissertation are organized as follows: Chapter 2 details the development of the initial handheld prototype, featuring a 400 kHz imaging speed and a 55° field of view. This prototype, combined with the scleral depression, allowed peripheral area visualization, though it did not provide an adequate field of view for peripheral retinal visualization. Chapter 3 describes the second handheld prototype iteration, which integrated an aspherical lens to extend the field of view to 105°, the widest in non-contact OCT retinal imaging systems. Additionally, a novel spiral scanning pattern improved scanning efficiency. However, this version encountered beam wandering and alignment challenges due to a limited working distance (5 mm). Chapter 4 addresses these issues by presenting a non-mydriatic imaging system with custom optics, offering a similar field of view, maintaining a lateral resolution of 20 μm, and providing a working distance of 16 mm – significantly longer than previous ultra-widefield OCT imaging systems. Chapter 5 introduces the third handheld prototype iteration with a contact-based

design, achieving a 140° field of view, reducing alignment time, enhancing image quality, and increasing success rates, especially for infant imaging. Chapter 6 presents the fourth handheld prototype iteration, which used a custom-designed lens group instead of off-the-shelf lenses in the relay section and incorporated two aspherical lenses to enhance the optical performance. This design, coupled with an 800 kHz imaging speed, re-enabled the OCTA mode, delivering superior image quality. Chapter 7 discusses the various applications of handheld OCT/OCTA imaging systems in pediatric diseases such as ROP, retinoblastoma, incontinentia pigmenti, Coats disease, and retinal detachment. Finally, Chapter 8 explores future research directions for handheld OCT/OCTA imaging systems and concludes the dissertation.

CHAPTER 2. HIGH-SPEED AND WIDEFIELD HANDHELD SWEPT-SOURCE OCT ANGIOGRAPHY WITH A VCSEL LIGHT SOURCE

2.1 Abstract

Optical coherence tomography (OCT) and OCT angiography (OCTA) enable noninvasive structural and angiographic imaging of the eye. Portable handheld OCT/OCTA systems are required for imaging patients in the supine position. Examples include infants in the neonatal intensive care unit (NICU) and operating room (OR). The speed of image acquisition plays a pivotal role in acquiring high-quality OCT/OCTA images, particularly with the handheld system, since both the operator's hand tremor and subject motion can cause significant motion artifacts. In addition, having a large field of view and the ability of real-time data visualization are critical elements in rapid disease screening, reducing imaging time, and detecting peripheral retinal pathologies. The arrangement of optical components is less flexible in the handheld system due to the limitation of size and weight. In this paper, we introduce a 400 kHz, 55° field of view handheld OCT/OCTA system that has overcome many technical challenges as a portable OCT system as well as a high-speed OCTA system. We demonstrate imaging premature infants with retinopathy of prematurity in the NICU, a patient with Incontinentia Pigmenti, and a patient with X-linked retinoschisis in the OR using our handheld OCT system. Our design may potentially improve the diagnosis of retinal diseases and help provide practical guidelines for designing a flexible and portable OCT system.

This work has been published in Biomedical Optics Express.

Shuibin Ni, Xiang Wei, Ringo Ng, Susan Ostmo, Michael F. Chiang, David Huang, Yali Jia, J. Peter Campbell, and Yifan Jian, "High-speed and widefield handheld swept-source OCT angiography with a VCSEL light source," Biomed. Opt. Express 12(6), 3553–3570 (2021).

2.2 Introduction

Optical coherence tomography (OCT) and OCT angiography (OCTA) have become an essential tool for the health evaluation of the retina in adults and are being explored as a noninvasive method that can produce objective biomarkers, which leads to earlier and more objective diagnoses in adult retinal diseases. OCT has also become part of the standard of care in adult retinal practices due to the value added by the ability to identify subclinical disease features and objectively track disease progress in many of the leading causes of blindness [5,27–29]. Treatment paradigms for diabetic retinopathy (DR) and age-related macular degeneration (AMD) now integrate OCT findings into the disease management. OCTA is based on detecting flow-related amplitude and/or phase variation/decorrelation in successive B-frames acquired at the same location. The intrinsic motion contrast obviates the need to inject any extrinsic contrast agent. OCTA research and clinical applications are expanding greatly due to the ability to noninvasively visualize the retinal and choroidal circulation in adults [30–33]. Although OCTA has been demonstrated since 2006 [34], clinical applications require many technical improvements to enhance practicality. Most of the OCTA methods require at least two repeated OCT B-scans at the same transverse location to detect blood flow, which significantly increases the image acquisition time and motion artifacts. Also, OCTA is more sensitive to transverse digital resolution, optical resolution, a large imaging spot size, and low sampling rate may result in OCTA images with poor contrast and signal-to-noise ratio (SNR). In the commercial OCT/OCTA systems, the OCT A-scan rate is typically lower than 100 kHz, thus a compromise must be made between acquisition time and field of view. Most commercial OCT/OCTA imaging devices are desktop systems that are limited in speed and designed for adults who can fixate. The benefits of OCTA have yet to extend to the general pediatric retina as it is difficult and impractical to image unanesthetized and

uncooperative infants with a desktop OCTA system. Even the commercially available portable devices for young children are unsuitable for OCTA due to insufficient speed.

Several groups, including our own, have developed prototype handheld OCT systems that can be used to image patients in the supine position [11,14,15,35]. The improved portability allows screening to be done within primary care settings or in the operating room (OR). The development of swept-source OCT sparked a rapid increase in OCT imaging speed from several tens of kHz to more than one MHz, making OCTA with a handheld probe feasible. Campbell *et al.*, Viehland *et al.*, and Song *et al.* demonstrated handheld OCTA for imaging neonates with retinopathy of prematurity (ROP) [12,14,15], a retinal vasculature disease that affects premature babies and could lead to permanent vision loss if not diagnosed and treated in time. Several clinical studies showed the potential of using OCT and OCTA to study ROP [36–39]. Nadiarnykh *et al.* showed the clinical utility of a handheld OCTA system for diagnostic imaging of pediatric retinoblastoma as well as monitoring disease progression and response to treatment [13]. These prototype handheld systems did not have the field of view that is needed for visualizing the peripheral retina where the pathologies in diseases such as ROP occur. We are the only group to have demonstrated the ability to obtain ultra-widefield (UWF) OCT images on non-sedated babies with ROP [12]. Due to the challenges of imaging a non-fixating and non-sedated neonate, it has been difficult to consistently obtain high-quality data for biomarker evaluation in ROP. In addition to the hardware constraints, most research and commercial handheld OCT systems cannot currently visualize the retina volumetrically in real time due to the intensive computational requirement for OCT image processing. Acquisition of volumetric OCT images at video rate is possible with high-speed OCT systems, but without adequate processing power, these raw interferometric data cannot be converted to images fast enough to meet the acquisition rate. However, for the desktop OCT

systems for imaging adults, a simple preview of selected OCT B-scans is often sufficient to evaluate and optimize image quality. Patient alignment and locating landmarks on the ocular fundus can be easily accomplished with the help of a fixation target and a secondary fast fundus imaging modality such as a scanning laser ophthalmoscope or a near-infrared fundus camera. In handheld OCT, the pupil camera and on-probe display have been integrated to facilitate alignment [14,16,40]. However, these features may add complexity and weight to the handheld system. Real-time visualization of the OCT *en face* and cross-sectional scans on the imaging probe could be instrumental in guiding the imaging procedure, confirming the areas of interest captured, and reducing imaging time for the most fragile patient populations.

There is a need for a dedicated portable handheld OCT/OCTA retina scanner for the pediatric population that extends the field of view to the peripheral retina and displays the cross-sectional and *en face* views of the targeted area in real-time. In this manuscript, we demonstrate a 400 kHz, 55° field of view handheld OCT/OCTA system that has overcome many technical challenges in high-speed OCTA imaging as well as in pediatric retinal imaging in general and shows its potential to improve diagnosis of retinal diseases and provide clinical validation.

2.3 Methods

2.3.1 OCT System Design

The schematic of the high-speed and widefield handheld OCTA system is shown in Figure 2.1. The swept-source laser used in our system was a vertical cavity surface emitting laser (VCSEL) (SVM10F-0210, Thorlabs, Inc., USA). This laser has an A-scan sweep rate of 400 kHz, a center wavelength of 1060 nm, and 100 nm bandwidth, corresponding to a theoretical axial resolution of 4.94 μm in the air. The high output power of this VCSEL source allows us to optimize the fiber-based interferometer so that we could deliver a sufficient and safe amount of imaging

beam power to the sample arm while maximizing collection efficiency. The 4-coupler interferometer in this system consisted of a 10/90 fiber coupler, a 20/80 coupler, and two 50/50 fiber couplers. The OCT sample arm was connected to a set of 10/90 coupler and a set of 20/80 coupler. The 10/90 coupler split 90% of the laser output power to the 20/80 coupler, and the 20/80 coupler split 20% of its input power to the sample arm. The 10% laser output power that was split by the 10/90 fiber coupler was delivered into the reference arm through a 50/50 fiber coupler. 80% of the light collected from the sample arm and 50% of the light reflected from the reference arm were combined within the 50/50 fiber coupler and detected with a balanced detector (PDB482C-AC, Thorlabs Inc., USA).

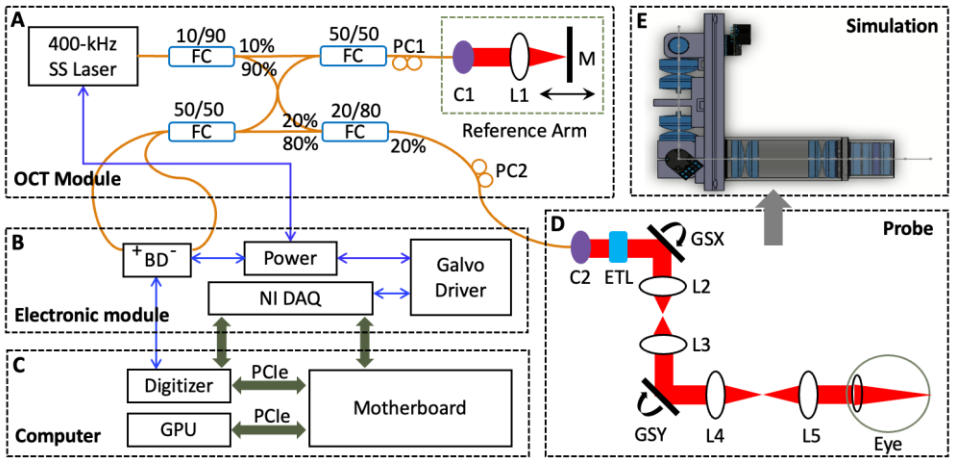

Figure 2.1 Schematic diagram of the handheld OCTA system. (A) OCT module, including the laser source, the spectrometer, and the motorized reference arm. (B) Electronic module, including the VCSEL source, the balanced detector, data acquisition, control module (BNC-2110, National Instrument Inc., USA), and digital servo driver for galvanometer scanner (Pangolin Laser System Inc., USA). (C) Custom-built computer integrated with GPU and digitizer (ATS9373, Alazar Technologies Inc., Canada) via PCI Express (PCIe) link. (D) Optical layout of the probe. (E) Opto-mechanical simulation of the probe in SolidWorks. M: mirror; PC1-PC2: polarization controller; FC: fiber coupler; BD: balanced detector; GPU: graphics processing unit. GSX: the fast axis of the galvanometer scanner; GSY: the slow axis of the galvanometer scanner; L1-L5: lens; C1-C2: collimator; ETL: electrically tunable lens.

A 3 m fiber patch cord was connected to the sample arm for flexible handheld operation and a 3.3 m fiber patch cord was connected to the reference arm to match the optical path length and dispersion of the sample arm. In addition to matching the optical path length, the polarization state between the sample and reference arm needed to be matched for interferometry. Bending of the optical fiber patch cord in the sample arm would alter the polarization state, and the polarization mismatch between the sample and reference arm would decrease the OCT SNR significantly. A two-paddle manual fiber polarization controller with a loop diameter of 18 mm (FPC020, Thorlabs Inc., USA) and a two-paddle motorized fiber polarization controller (MPC220, Thorlabs Inc., USA) were installed in the path of the sample arm and reference arm, respectively. A custom-built motorized reference arm with a tunable range of 100 mm was implemented to adjust the optical delay when switching between adult and neonate scanning.

2.3.2 Optical Design of the Handheld OCTA Probe

The optical design of the handheld OCTA probe is shown in Figure 2.2. The sample arm optics were designed and optimized in OpticStudio (Zemax LLC, USA), and assembled with off-the-shelf optical components. The distances between the optical elements in the sample arm were optimized by minimizing the spot radius on the focal plane and the imaging beam wandering on the pupil plane. Starting from the 20/80 fiber coupler, the beam entered through a 3 m single mode custom patch cable and was collimated into a 2 mm beam by a reflective collimator (RC02APC-P01, Thorlabs Inc., USA). It then passed through an electrically focus tunable lens (EL-3-10, Optotune, Switzerland), a pair of separated galvanometer mirrors (Saturn 1B, Pangolin Laser Systems Inc., USA) with a set of achromatic lenses set up in the 4f configuration in between to relay the beam. The scanning beam after the slow axis of the galvanometer scanner [GSY, Figure 2.2(B)] entered a pair of achromatic doublet lenses with 30 mm diameter and 100 mm focal length

as scan lens [L5-L6, Figure 2.2(B)], and then entered a 5-lens group that together to form an ocular lens [L7-L11, Figure 2.2(B)]. The 5-lens group consisted of a pair of 30 mm positive achromatic doublet lenses with 100 mm focal length, 1-inch negative achromatic doublets lens with -100 mm focal length, and a pair of 1-inch positive achromatic doublet lenses with 50 mm focal length. The scan lens and ocular lens worked as a 1.6× telescope, which amplified the scanning angle from 34° to 55°. The imaging beam was also demagnified from 2.1 mm in the slow axis of the galvanometer scanner to 1.3 mm at the pupil plane. The working distance of the handheld probe was 9.8 mm, which was reasonable for imaging both the adults and neonates.

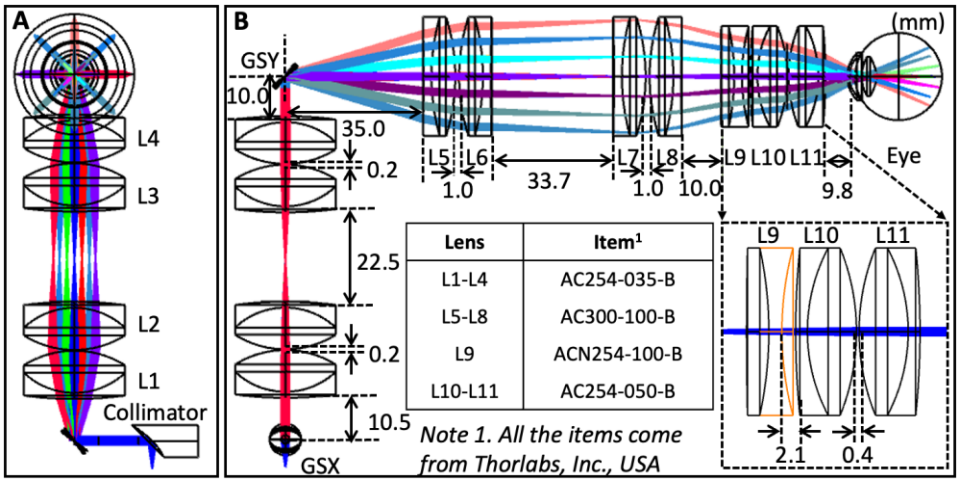

Figure 2.2 (A) Side view of 3D layout in OpticStudio. (B) Front view of 3D layout in OpticStudio. All the lenses' configurations in the probe and the distance between components were illustrated.

The fast and slow axis of the galvanometer scanning mirrors were separated to reduce the vignetting artifacts and the imaging beam wandering on the pupil plane a technique often used in adaptive optics retinal imaging systems [41,42]. The ocular lens was made up of a group of 5 lenses with different diameters to increase the scanning angle and improve the optical performance. For comparison, we simulated a second optical design, which was referred to as the 'conventional handheld OCT system' [Figure 2.3(B) and Figure 2.3(D)]. In this classical optical design of retinal OCT system, the galvanometer scanning mirrors were not separated and the ocular

lens (5-lens group) was replaced with a pair of achromatic doublet lenses with a 30 mm effective focal length to ensure the same beam size at the pupil plane compared to our design. In the current study, we evaluated our optical design with an adult model instead of an infants' model, because there is no well-developed and accepted infant eye optical model in the literature, and the anatomic relationships in the infant's eye are not proportional to the adult. Specifically, the lens takes up a relatively larger volume than in the adult eye, and as a result, most infants are hyperopic for the first few years of life. Figure 2.3(A) and Figure 2.3(B) show the comparison of multi-configuration spot diagrams in these two optical designs with the same field of view. These figures demonstrated that the aberration at large scanning angles was significantly reduced after implementing the design improvement. The root mean square (RMS) of the spot radius of the upper left corner (the purple ray) in Figure 2.3(A) and Figure 2.3(B) was decreased from 21.5 μm to 15.8 μm after optimization. In addition to the focused spot radius on the imaging plane which represents the transverse resolution, the imaging beam wandering on the pupil plane is also a critical and yet often omitted metric in evaluating the optical performance of a retinal OCT imaging system. It is especially important in widefield OCT systems as the vignetting and aberration are introduced significantly at larger scanning angles [43]. Figure 2.3(C) and Figure 2.3(D) show the comparison of imaging beam wandering on the pupil plane in these two optical designs with 0°, 20°, and 38° scanning angles. The 20° angle translates to a 6×6 mm field of view in an adult normal eye. 38° is the maximum angle in the conventional handheld OCT system. The results of the comparison indicated that the integrated galvanometer scanning mirrors layout had a great impact on the beam footprint on the pupil plane. The maximum diameter of the footprint diagram in the optimized handheld OCT system and the conventional handheld OCT system was 1.88 mm and 2.41 mm, respectively. The amount of imaging beam wandering on the pupil plane was reduced significantly

after separating the galvanometer scanning mirrors because both galvanometer mirrors are optically conjugated on the pupil plane. To further increase the scanning angle, 30 mm diameters rather were selected over typical 1-inch lenses for L5-L8. The larger the diameter of the lenses close to the scanner with the same effective focal length, the wider scanning angle was achieved. One trade-off for using larger lenses was that it increased the weight of the probe, which may cause operator fatigue. Another disadvantage of implementing larger lenses was that it disrupted the ergonomics of the handheld probe, making it more difficult to hold steady and maneuver. A shorter effective focal length at this position could also increase the scanning angle, but the imaging beam size on the pupil plane would be further demagnified, which would reduce the system's numerical aperture and transverse optical resolution. This issue could be solved by choosing a collimator with a longer focal length; however, corresponding larger aperture galvanometer mirrors are needed to accommodate the increased beam diameter. Because this system's B-scan frame rate is in the order of kHz, it demands high performance from the galvanometer scanning mirror, and in general smaller aperture galvanometers are faster.

The primary application of our handheld OCT/OCTA system is screening retinal disease for infants whose eyes are significantly shorter than adults' and there is a large variance between premature babies and babies that were born later in the pregnancy terms. Our sample arm's optical design aims for a balance between the field of view, transverse optical resolution, and performance of the galvanometers. The final beam size on the pupil plane was 1.3 mm, and when imaging an infant with an axial eye length of 17 mm, it results in a focused spot of approximately 12.6 μm in diameter ($1/e^2$) on the retinal plane.

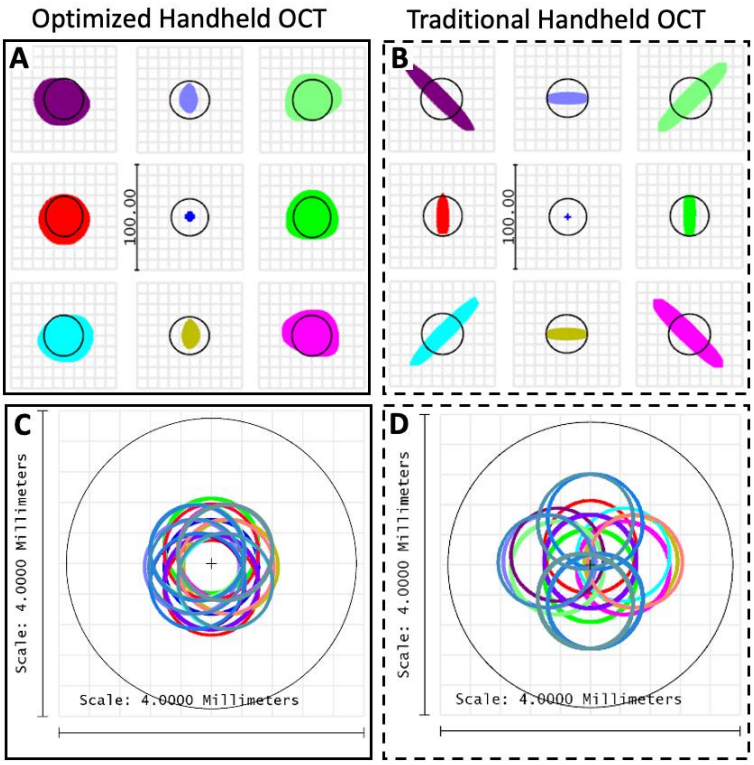

Figure 2.3 Comparison of multi-configuration spot diagrams for the optimized optical design (A) and conventional optical design (B) of handheld OCT system with a 28° field of view, which is equivalent to 9×9 mm. The radius of Airy Disk (black circle) is 19.0 μm (A) and 19.6 μm (B). Comparison of imaging beam wandering on the pupil plane with the combination of 0°, 20° (6× 6 mm), and 38° (maximum scanning angle of the conventional handheld OCT system) field of view for the optimized optical design (C) and conventional optical design (D) of handheld OCT system. The maximum radius of the footprint diagram is 0.94 mm (C) and 1.21 mm (D).

2.3.3 Mechanical Design of the Handheld OCTA Probe

The optical simulation of sample arm optics was exported to CAD software (SolidWorks, Dassault Systèmes, France) for the mechanical design, where the precise locations of each optical component were specified according to the optical simulation. Since the measurement of OCTA was based on the change of blood flow signal, the subtle motion of the system or the subject could affect the results. Compared to the conventional desktop-based OCT system, the motion of the

operator's hand is an extra source of motion artifacts that could corrupt the OCTA signals in the handheld system. Our mechanical design of the handheld imaging probe is ergonomic. With a single hand, the operator could hold the lens tube instead of the body of the probe, which allowed the operator to rest parts of their palm gently on the infant's forehead and manipulate the eye position using a depressor with their other hand when necessary. The grip permitted the operator to align the target area with a slight rotation of the wrist. The mechanical design for the probe is shown in Figure 2.4.

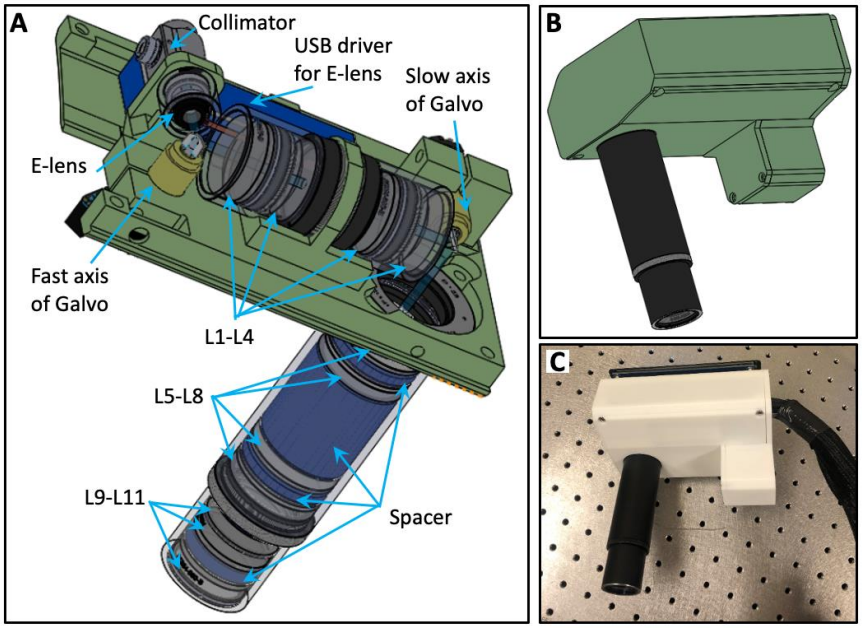

Figure 2.4 (A) Mechanical layout of the key components of the probe. (B) Appearance of the fully assembled probe in SolidWorks. (C) Photograph of the probe with 3D printed enclosure. E-lens: electrically tunable lens.

To ensure precise alignment of the lenses, the lens tube with the required length was customized by the manufacturer (Thorlabs Inc., USA). The spacers between the lenses were designed and fabricated according to the optical simulation. Multiple positioning slots were designed on the enclosure to make sure that the components were assembled in the specified location. The enclosures and spacers were fabricated by a 3D printer (S5, Ultimaker B.V.,

Netherlands) with a resolution of ±0.1 mm. The collimator and galvanometer scanners were directly mounted onto the high-resolution 3D-printed enclosure without the aluminum heatsink to reduce the bulk and weight of the probe. The last group of lenses required frequent cleaning; therefore, an adapter was used to connect two lens tubes so that it could easily be if necessary. Figure 2.4(C) shows a photograph of the fully assembled handheld probe. The handheld probe, excluding the fiber and electrical cables, weighed about 700 grams and had the dimensions of 148×97×175 mm (length × width × height). A 5.5-inch AMOLED display was integrated on top of the probe to facilitate alignment. Two separate imaging windows, B-scan and *en face* OCT, were shown on the screen [Figure 2.5(C)]. All the electrical cables and optical fiber were wrapped into a nylon protective sleeve sheath, which provided some minor strain relief on the cables and protected them from abrasion.

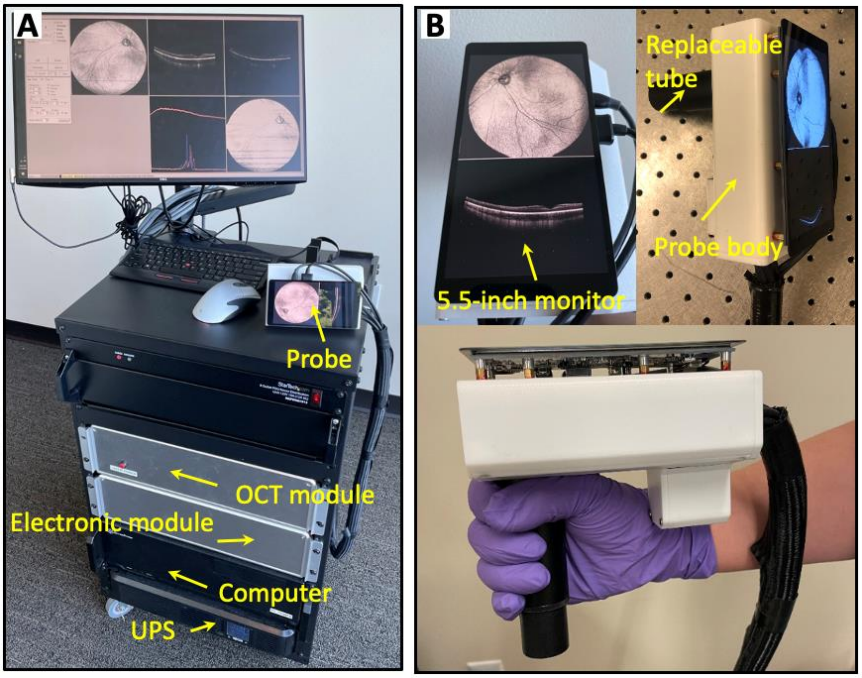

Figure 2.5 (A) Photograph of the front of fully assembled handheld OCTA system in portable cart. (B) Photograph of the handheld probe.

2.3.4 System Assembly

The imaging system consisted of an OCT module, an electronic module, a computer, and a handheld probe. The OCT module and electronic module were separately assembled into two 19-inch rack enclosures of 3 rack units (U) in height (EC3U, Thorlabs Inc., USA). The computer was assembled in a 19-inch rack enclosure of 4U height. The three enclosures were communicated through detachable cables and installed in a 16U server rack with lockable caster wheels [Figure 2.5(A)], which could be transported easily between different sites for imaging. The fully assembled system is shown in Figure 2.5. The uninterruptible power supply (UPS), with line-interactive topology, provided backup power to keep the system running during transportation from one ward to another and protected the system from power fluctuations. The smart cooling fan mounted on the back of the portable cart took feedback from a temperature sensor placed near the VCSEL (laser) module to maintain its temperature below 50 degrees Celsius. To help maintain the proper airflow, panel spacers with perforated venting were installed on the back of the cart.

2.3.5 Image Acquisition Protocol

The output of the balanced detector was digitized by a 12-bit waveform digitizer board with an external k-clock provided by the laser. The VCSEL source has a long coherence length of over 100 mm, so the limiting factor for the OCT imaging depth in our system is the interferogram sampling density. To increase the imaging depth, which is critical in ultra-widefield imaging, we used the dual-edge sampling feature of the digitizer. This feature allowed us to sample the spectrum at both rising and falling edges of the sampling clock (external k-clock). The 400 kHz VCSEL swept-source laser used in our system has a 50% duty cycle and each raw A-scan spectrum was sampled with 2048 points corresponding to a peak sampling frequency of 1720 MHz and a maximum imaging depth of 6 mm in air. The sensitivity of the system is 102.9 dB and the signal

roll-off is 2.4 dB across the 6 mm imaging depth. The total round trip optical path length in our system is 12.97 m in air, which created a 43.22 ns delay between the external k-clock signal and the interferometric signal when it was sampled at the digitizer. To counteract this delay, a 25-foot coaxial cable was added between the output of the k-clock signal on the laser module and the input external clock port on the digitizer. The remaining mismatch was fine-tuned by the laser's software.

High-speed swept-source OCT significantly reduces motion artifacts for *in vivo* clinical imaging. It is especially critical to handheld clinical imaging applications. OCTA is based on detecting flow-related amplitude and/or phase variation/decorrelation in successive B-frames acquired at the same location. The intrinsic motion contrast obviates the need for the injection of any extrinsic contrast agent; however, a 3-5 ms interval [20] between the repeated B-scans is desired for OCTA to detect sufficient blood flow coming from motion contrast. In high-speed OCT, the interval between consecutive B-frames at the same position is too short to detect moving red blood cells. Furthermore, the B-frame rate is limited by the frequency of the scanner (<500 Hz at large scanning angles). Instead of slowing the system to achieve the desired 3-5 ms interval [20] to detect capillary blood flow with OCTA, we recently developed a stepped bidirectional scanning pattern [44,45] that enables a faster B-frame rate (up to 1 kHz at 30°). In this project, we designed an OCTA scanning pattern (Figure 2.6) that performs three repeated B-scans at the same location with 500 A-scans per B-scan and a 5 ms interval between the repeated B-scans, leading to a total of 1500 B-scans per volume. Each volume acquisition time was 1.875 seconds. OCTA B-scans were generated by the split-spectrum amplitude-decorrelation algorithm (SSADA) [24,46], computed from the three repeated B-scans acquired at each position. *En face* OCTA images were generated after manual retinal layer segmentation. The *en face* OCTA image was then processed

using the medium subtraction method to remove small motion artifacts, a Gabor filter was also applied to enhance the OCTA signal [47,48]. A customized color map was applied for each *en face* image to improve the OCTA visibility. In SSADA, the speckle decorrelation of OCT B-scans generated for different spectral bands of interferometric signal yielding the OCT B-scan images is averaged, improving the SNR of flow detection over full-bandwidth speckle decorrelation measurement.

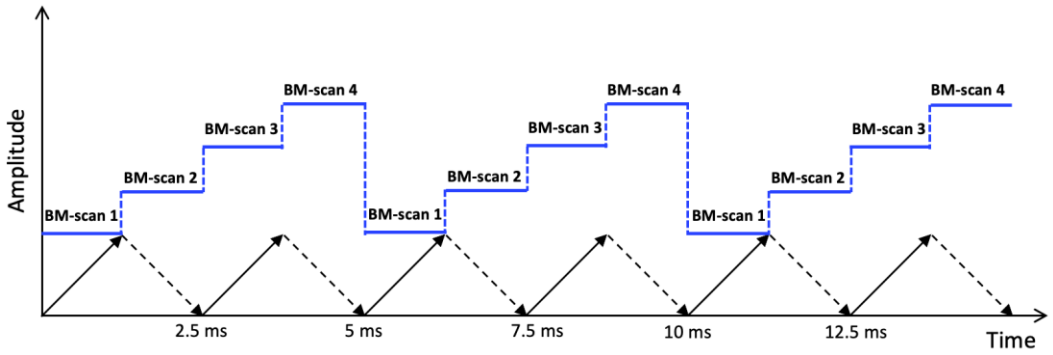

Figure 2.6 Stepped bidirectional scanning pattern with three repeated B-scans. Solid and dashed arrows represent fast scan (B-scan). Here, three repeated B-scans were used to detect OCTA. The interval between the repeated B-scans was 5 ms.

2.3.6 Software Operation and Data Visualization

OCT and OCTA images were acquired and processed in real-time continuously by our custom-written GPU-accelerated software OCTViewer, providing an immediate evaluation of the image quality [49,50]. The data acquisition computer consisted of an Intel Core i9 9900k CPU, an NVIDIA Titan RTX GPU, a multifunction I/O DAQ (PCIe 6353, National Instrument Inc., USA), and a high-speed digitizer (ATS9373, Alazar Technologies, Inc., Canada). In addition to the 5.5-inch display installed on the handheld probe, a 24-inch monitor was also mounted on the imaging cart to display more information, including OCTA *en face*, cross-sectional views, and selected raw and processed A-scans. There were two scanning modes available on the handheld OCTA system.

One mode was the warp scan, which was a high-speed alignment mode and used to identify and align the target area. A sinusoidal scanning pattern was used for the fast axis galvanometer scanner, and the *en face* view of the aiming area was desinusoided and displayed continuously in real-time. The acquisition time of each volume was 120 ms with 400 A-scans per B-scan and 120 B-scans per volume, which provided real-time feedback in optimizing images. Once the target area on the ocular fundus was located, the focus could be optimized automatically based on the brightness of the *en face* images with a hill-climbing algorithm within 1 second [51]. The second scanning mode was the OCTA mode, which was used to acquire high-resolution OCTA volume. A secondary keyboard was connected to the computer with 6 shortcut keys programmed to save data, toggle scanning modes, auto-focus, auto-polarization control, and adjust reference arm length.

2.3.7 Study Subjects

Handheld OCT/OCTA retinal imaging was performed on adults, sedated infants, and fully awake neonates. These patients were recruited from the Casey Eye Institute at the Oregon Health & Science University (OHSU). Written informed consent from the patient or parent/guardian in case of minor patients was obtained before initiating the study. The research was approved by the Institutional Review Board/Ethics Committee of OHSU under the Declaration of Helsinki. The imaging for the non-sedated infants was conducted with pharmacological dilation per standard protocols in the OR and neonatal intensive care unit (NICU). The optical power incident on the subject cornea was set to less than 1.8 mW, which is within the American National Standards Institute (ANSI) Z80.36-2021 standards for the safe ocular laser exposure limit at 1060 nm [52].

2.4 Results

In this study, 3 healthy adult volunteers, 16 awake neonates in the NICU, and 7 pediatric patients under general anesthesia before retinal surgery in the OR were imaged. Prior to the

imaging session, the subjects were dilated with cyclomydril, an eyelid speculum was used to keep the eye open, and a balanced salt solution was applied regularly to prevent the eye from drying. The operator began by sitting close to the head of the neonate and positioned the device close to the eye with the lens cap attached then initiated the automated polarization state matching based on the brightness of the lens cap *en face* image. Next, the imaging session began, starting in warp scan mode, which offers an *en face* view at a high refresh rate allowing the operator to quickly align the system to the retina. The reference arm length was predetermined based on the age of the subject and fine-tuned during the imaging procedure. The warp scan mode provided the *en face* view from the front of the eye into the retina as the operator adjusted the working distance. Ocular fundus would start to appear in the *en face* view as the probe got closer to the eye, and the operator can identify the larger vascular structures and any extraretinal pathology within an approximately 100×100-degree window by pivoting the probe. Once the desired region of interest was located, autofocusing was performed in 1 second based on the brightness of the *en face* view. We then switched to OCTA mode which continuously acquired volumes every 1.875 seconds. The OCT *en face* and B-scan were viewed in the on-probe display and desired volumes were saved in an independent thread so that the image acquisition and processing did not halt during the saving process. Figure 2.7 indicates a screen capture of the external monitor on the imaging cart demonstrating the data acquisition process described above.

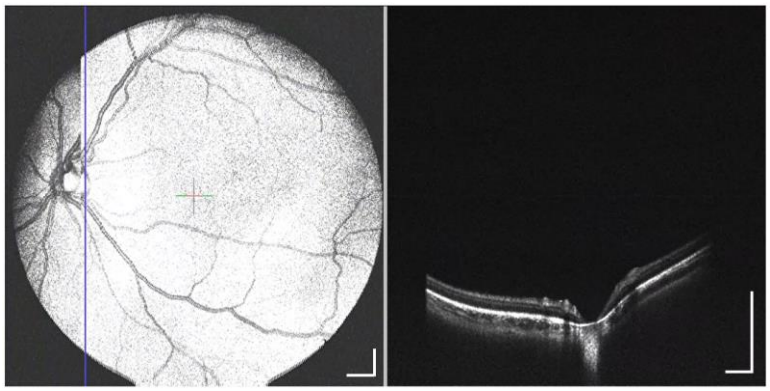

Figure 2.7 Screen capture of the OCTViewer software representing the data acquisition process. Scale bars are 1 mm.

The retinal OCT/OCTA images from two representative cases - a patient with ROP a patient with X-linked retinoschisis (XLRS) - are shown in Figure 2.8 and Figure 2.9 separately. Figure 2.8 shows the *en face* OCT image and corresponding OCTA image of the inner retina from a premature infant with ROP after laser treatment. While laser treatment is often effective in inducing regression of extraretinal neovascularization, in some cases vitreoretinal traction can worsen leading to vascular dragging, retinoschisis, and retinal detachment [53]. These changes are much easier to appreciate on OCT compared to the clinical exam, and early detachment of the retina is typically located in the retinal periphery, out of the field of view of traditional OCT even in adults. Therefore, an imaging system with a wide field of view and can visualize the peripheral retina is needed, to follow up after the treatment. Figure 2.8(A) indicates the *en face* OCT image in the peripheral retina. The area indicated by the red arrow [Figure 2.8(A)] is the chorioretinal scar left by the laser treatment, without evidence of residual neovascularization, fibrosis, or traction.

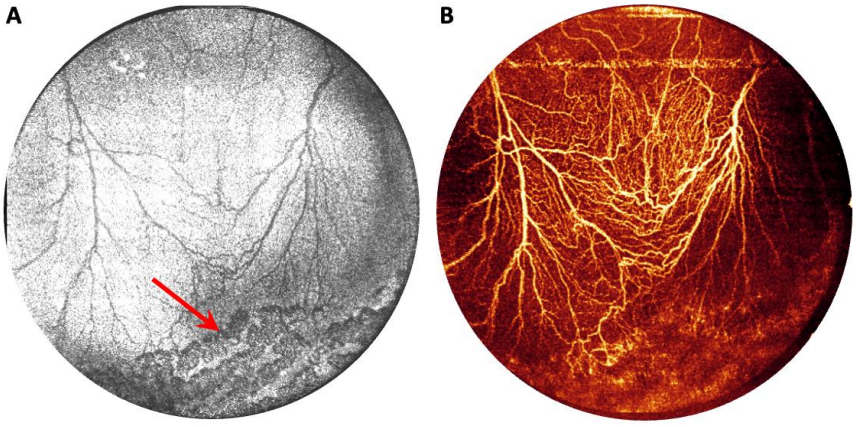

Figure 2.8 (A) *En face* OCT image from an infant with retinopathy of prematurity (ROP) after laser therapy. Laser scars are shown with the red arrow. (B) Corresponding OCTA *en face* image of the inner retina.

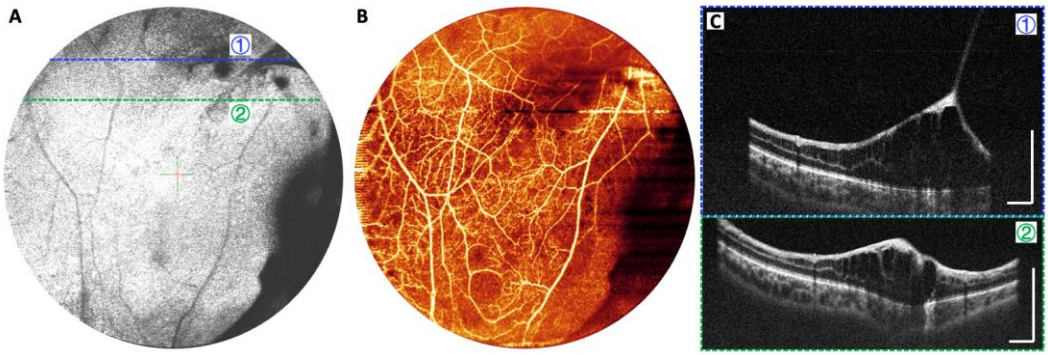

Figure 2.9 (A) *En face* OCT image from a patient with XLRS. (B) Corresponding OCTA of the inner retina. (C) Two selected B-scans with the symptoms of retinal detachment. Scale bars are 1 mm.

Figure 2.9 shows *en face* OCT image, a corresponding OCTA *en face* image of the inner retina, and two selected B-scans from a patient with XLRS imaged in the OR before surgery. The locations of selected B-scans in Figure 2.9(C) are indicated by the blue (①) and green (②) dashed lines in *en face* OCT image [Figure 2.9(A)]. XLRS is a kind of congenital retinal disease, which caused by a genetic mutation on the X chromosome that prevents encoding the protein necessary for cell-to-cell adhesion throughout retinal development [54]. Two selected B-scans demonstrate the typical findings of intraretinal schisis and vitreoretinal traction from a large schisis cavity. One of the key management decisions is based on the distinction between retinoschisis and retinal detachment. Our present system could be used to examine the suspected area and visualize the pathology in real-time and with higher resolution than is available with other modalities such as ultrasound.

2.5 Discussion

Aligning and imaging uncooperative, non-sedated, and non-fixating neonatal patients is difficult, and due to their medical comorbidities, it is critical to be able to obtain high-quality images within 1-2 minutes. Thus, real-time visualization is a highly desirable function for a

mission critical handheld imaging device, and commercial handheld fundus cameras (RetCam) that are used routinely in ROP screening have implemented this function. Unlike conventional 2D imaging modalities, OCT requires optical path length matching between the reference and sample arms, which causes the alignment of OCT to be more challenging. Moreover, real-time OCT data processing and visualization is more computation intensive, and real-time *en face* OCT requires a high-speed OCT system to achieve a usable refresh rate. Several excellent publications have demonstrated impressive progress on handheld OCT/OCTA with improved ergonomics and clinical utility [7,8,11,12,15,55–58]. The major effort in this study is to leverage the recent advances in laser light source, high-performance computing, and optical design to improve a handheld OCT/OCTA system's usability in pediatric retinal imaging. Compared to previous work, we were able to improve image quality while maintaining a field of view and ergonomics and reduce time required for imaging sessions.

With the combination of the two scanning modes and GPU-accelerated OCT processing software, we believe we were able to balance the design trade-offs between imaging speed, field of view, and resolution. Warp scan mode has high *en face* imaging speed and is used for initial alignment and locating regions of interest. OCTA mode has a large volumetric field of view and offers a panoramic view of the retinal layers and vasculature. Although our OCTA scan pattern does not satisfy the Nyquist sampling theorem, we were still able to acquire high-quality OCTA images that provide sufficient angiographic information for disease diagnosis. We could increase the sampling density of the OCTA scans; however, it would result in a longer imaging time and more severe motion artifacts. We found that with our current OCTA scanning pattern, motion artifacts caused by the operator's hand tremor was minimal. The prevalent motion artifacts were introduced by the subjects' eye motion. The 400 kHz VCSEL light source was instrumental in this

study, as not only did it provide fast imaging speed, but also a long depth range. Due to time constraints when imaging uncooperative infants, it is not always possible to adjust the reference arm position so that the retina is placed close to DC. Therefore, having good imaging quality over the entire imaging depth is critical to improving the imaging success rate.

The optical design of the OCT sample arm in this study significantly enhanced performance by effectively controlling system aberrations and minimizing the beam wandering on the pupil plane. The representative images in the results section showed no vignetting artifacts, and a high-quality OCTA signal was observed over the entire field of view, evidence of high-performance optical design as the OCTA signal is more sensitive to optical aberrations. Images with a reduced field of view showed exquisite details of the retinal capillaries and neovascularization indicating that our optical design provided sufficient transverse resolution down to the capillaries level. The optimized interferometer increases the collection efficiency which is important in the high-speed OCT system. Our lightweight and ergonomic mechanical design allowed the operator to pivot the imaging probe to locate the region of interest on the ocular fundus.

In handheld imaging applications, a MEMS scanner is appealing as it is significantly lighter than galvanometer scanners, and using a two-axis MEMS scanner does not require a set of telescopes as was in our system with galvanometer scanners. In this study, we chose to use galvanometer scanners because they offer high scanning speed, better linearity, and repeatability which are all critical in high-speed OCTA imaging. Instead of using a heavy metal mounting block for the galvanometer scanners, we designed a rigid and stable 3D-printed base plate that mounted the scanners and lenses. The imaging system described in this report has been used in the NICU and OR weekly for more than 8 months, and we didn’t experience any optical performance degradation or structural integrity issues with the 3D-printed baseplate and enclosure.

Despite the overall improved design and excellent OCTA image quality, there are some limitations of our handheld OCT imaging probe. The 55° field of view of our imaging system in this study is still not wide enough to cover the entire peripheral retina extending beyond zone II in one snapshot. An ultra-widefield of view retinal imaging system with over 100° field of view is desired. OCTA with a 100° field of view would require an even faster laser of over 1 MHz and a contact lens-based sample arm design, which cannot be assembled from off-the-shelf optical components. Our OCT imaging system cannot yet resolve all the capillaries, and further increasing the transverse resolution may require adaptive optics to compensate for the system and ocular aberrations especially at the peripheral retina [59,60]. And with high-speed swept-source OCT, a sensorless adaptive optics approach might be feasible in handheld imaging systems [61–65]. It is also possible to average several OCTA *en face* images to improve the image quality and remove any residual motion artifacts [66]. The GPU OCT processing software and the on-probe display offer the operator real-time *en face* and cross-sectional views of the retina being imaged, but it does not display the *en face* OCTA images which could be more informative in disease diagnosis. Our GPU processing software is fast enough to calculate the OCTA B-scans, but real-time retinal layer segmentation is needed to generate meaningful *en face* OCTA images. We have demonstrated a deep learning based retina layer segmentation software that can segment 7 retina layers in an OCT B-scan in 3.5 ms [67], and we will improve and adapt this software for the handheld OCT in the future.

There are several compelling lessons learned from the adoption of OCT in adult retinal diseases that suggest OCT/OCTA may become essential not only for ROP but also for all pediatric retinal diseases in the future. OCT is superior to ophthalmoscopic exams for the diagnosis of macular diseases and has changed the way diseases such as AMD and DR, the two leading causes

of vision loss in adults, are classified. OCT has demonstrated the ability to detect subclinical diseases that are not visible on ophthalmoscopy, enabling earlier treatment in both conditions. Quantitative OCT metrics have enabled objective disease monitoring. The development of OCT coincided with a therapeutic transition towards the use of anti-vascular endothelial growth factor (anti-VEGF) drugs, where OCT is indispensable for monitoring response to treatment and determining retreatment frequency. A similar transition is slowly occurring in ROP; however, the monitoring of treatment response and disease recurrence is an unsolved problem due to the lack of objective disease metrics. The widefield high-speed handheld OCTA presented provides evidence that with real-time visualization and high-speed, OCT/OCTA has the potential to be used as a screening tool for general pediatric retinal diseases.

2.6 Conclusion

We have demonstrated widefield (55°) OCT and OCTA retinal imaging, with a 400 kHz handheld SS-OCT prototype that was custom designed for imaging infants. The novel optical design of the OCT sample arm significantly increases the scanning angle and minimizes the beam wandering on the pupil plane without introducing excessive aberration. Our handheld imaging system overcame several obstacles in terms of imaging time constraints and system alignment to achieve good image quality. The OCT/OCTA images presented in this study clearly showed retinal structures and microvascular abnormalities. We believe that with the aid of our system, we can improve the capability of diagnosis and help make therapeutic decisions for pediatric retinal diseases.

CHAPTER 3. 105° FIELD OF VIEW NON-CONTACT HANDHELD SWEPT-SOURCE OPTICAL COHERENCE TOMOGRAPHY

3.1 Abstract

We demonstrated a handheld swept-source optical coherence tomography (OCT) system with a 400 kHz VCSEL light source, a non-contact approach, and an unprecedented single shot 105° field of view (FOV). We also implemented a spiral scanning pattern allowing real-time visualization with improved scanning efficiency. To the best of our knowledge, this is the widest FOV achieved in a portable non-contact OCT retinal imaging system to date. Improvements to FOV may aid the evaluation of retinal diseases such as retinopathy of prematurity, where important vitreoretinal changes often occur in the peripheral retina.

3.2 Introduction

Ultra-widefield (UWF) optical coherence tomography (OCT) imaging technology has the potential to improve the detection and management of many diseases involving the peripheral retina. This includes retinopathy of prematurity (ROP), one of the leading causes of blindness and vision impairment in children [68], where adequate visualization of the peripheral retina is important for diagnosis and staging. While it is possible to achieve a larger field of view (FOV) by montaging smaller images together, this requires more time, and complex imaging processing, and may limit the ability of future algorithms to do automated segmentation of retinal structures and biomarkers. An expanded FOV allows the clinician to obtain more complete, continuous

---

This work has been published in Optics Letters.

Shuibin Ni, Thanh-Tin P. Nguyen, Ringo Ng, Shanjida Khan, Susan Ostmo, Yali Jia, Michael F. Chiang, David Huang, J. Peter Campbell, and Yifan Jian, "105° field of view non-contact handheld swept-source optical coherence tomography," Opt. Lett. 46(23), 5878–5881 (2021).

imaging of posterior and peripheral retinal pathology in a single capture. In the past, it has proven challenging to design a high-speed, wider FOV OCT system in a portable format owing to the weight and size constraints of the probe. Several experimental prototype handheld OCT systems were developed for various clinical applications over the past decade; however, there are no portable OCT systems that can acquire images from the posterior pole to the peripheral retina in a single, non-contact capture. We summarized the A-line rate and FOV of existing handheld OCT systems designed for retinal imaging from the literature as well as commercial devices (labeled with *) in Table 3.1, ordered by the date of publication. In this letter, we present a high-speed handheld swept-source OCT system with an unprecedented 105° FOV that extends the imaging area to the peripheral retina based on a non-contact approach. To the best of our knowledge, this is currently the widest FOV for a portable non-contact OCT system.

Table 3.1: Comparison of published handheld OCT system, designed for retinal imaging, listed by the date of publication.

Previous publications	A-line rate	Field of view
Woonggyu Jung, *et al.* [7]	140 kHz	10°
Chen D. Lu, *et al.* [8]	350 kHz	43°
Derek Nankivil, *et al.* [9]	100 kHz	22°
Francesco Larocca, *et al.* [10]	20 kHz	8.8°
Jianlong Yang, *et al.* [11]	100 kHz	40°
J. Peter Campbell, *et al.* [12]	100 kHz	100°
Oleg Nadiarnykh, *et al.* [13]	350 kHz	28°
Shaozhen Song, *et al.* [14]	200 kHz	72°
Christian Viehland, *et al.* [15]	200 kHz	30°
Joseph D. Malone, *et al.* [16]	400 kHz	40°
Shuibin Ni, *et al.* [69]	400 kHz	55°

*ENVISU C2300 OCT	32 kHz	70°

*Note: ENVISU C2300 OCT (Leica Microsystems GmbH)

3.3 Methods

In this letter, the novel optical design [Figure 3.1(A)] shares the same mechanical parts with the established 400 kHz and 55° FOV handheld OCT/OCTA system [69] except for the telescope design after the slow axis of the galvanometer scanner. The tuning range of the VCSEL source is 100 nm, which corresponds to an axial resolution of 4.94 μm in air. The sensitivity of the system was 102.9 dB and the signal roll-off across the full imaging depth of 6 mm in air was 2.4 dB [Figure 3.1(B)]. The scan lens consisted of a paired achromatic doublet lens with 30 mm diameter and 80 mm focal length (AC300-080-B, Thorlabs Inc., USA). The combination of a 1-inch negative achromatic doublets lens with -100 mm focal length (ACN254-100-B, Thorlabs Inc., USA) and an advanced double aspheric lens (Digital Wide Field, VOLK Optical Inc., USA) was used as the ocular lens. The scan lens and ocular lens worked as a 3.68× telescope, which amplified the scanning angle from 29° out of the scanner to 105° on the pupil. The working distance from the last lens surface to the cornea was ~5 mm, which is significantly shorter than the previously reported handheld OCT retinal imaging systems. The beam size on the pupil plane was 0.58 mm resulting in a theoretical focused spot size of 28.1 μm ($1/e^2$ diameter) on the retinal plane when imaging an infant with an axial eye length of 17 mm. The incident power on the cornea was 1.68 mW, which is within the ANSI Z80.36-2021 standards for 1060 nm light [52].

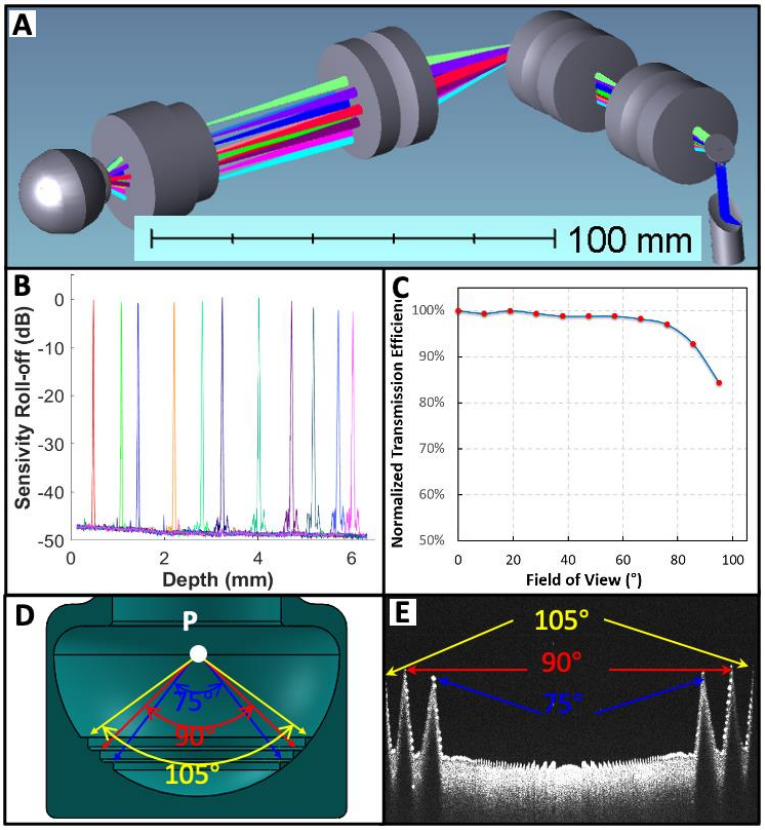

Figure 3.1 (A) 3D layout of handheld UWF OCT probe in OpticStudio. (B) Sensitivity roll-off of 2.4 dB across the full imaging range of 6 mm in air. (C) FOV dependence of measured normalized transmission efficiency. (D) Cross-sectional view of 3D rendered half sphere angle target with three concentric ring markers at angles of 75°, 90°, and 105°. (E) Cross-sectional scan of the angle target with maximum FOV.

The advanced double aspheric lens from Volk Optical had 90 diopters of refraction power with 30 mm diameter, which was commonly used in clinical exams. The lens was made with Volk's patented double aspheric design with minimized peripheral image distortion. Inspired by the characteristic, we sought to further explore the possibility of integrating the lens into our handheld OCT system. The original Volk lens had an anti-reflection (AR) coating for the visible wavelength range, which when used in OCT imaging at 1060nm would result in significant attenuation of the incidence power and the reduced collection of backscattered signals from the sample. Custom AR coating (reflectivity <0.5% from 950nm ~ 1150nm) was applied to both

optical surfaces of the double aspheric lens to improve the transmission in the infrared wavelength range. The incident power at different FOVs was measured to characterize the transmission efficiency of the AR coating, as shown in Figure 3.1(C).

A customized 3D printed target [Figure 3.1(D)] was used to calibrate the working distance and FOV. This target consisted of three concentric ring markers at angles of 75°, 90°, and 105°. The probe was moved along the axial direction so that the scanning pivot point is positioned on the center of the sphere, point 'P', in Figure 3.1(D), and the cross-sectional scan appeared close to flat [Figure 3.1(E)]. The cross-sectional scan with the maximum FOV captured all the markers, as seen in Figure 3.1(E), which implied the maximum FOV was 105°.

The sample arm of the OCT system was simulated and optimized in OpticStudio (Zemax LLC, USA). The metrics of the spot diagram and Strehl ratio were used here to evaluate the optical performance of the handheld UWF OCT system. Figure 3.2 shows the optical performance comparison between our previous design of 55° FOV [69] and the UWF OCT imaging system at 0°, 40°, and 55° FOV. The spot diagram and Strehl ratio of the UWF OCT system with the FOV from 60° to 100° are also presented in the last row of Figure 3.2(B). The Strehl ratio is shown in the upper left of Huygens PSF diagram. The spot diagram is commonly used in the evaluation of OCT system optical performance. The spread of rays and the type of aberrations could be easily observed in the shape of the spot diagram. However, the main problems of this metric were that it could not convey the intensity of the spot and the collected rays did not consider the diffraction-limited response. Unlike the handheld OCT/OCTA system at the FOV of 40° and 55° in which the geometrical aberration dominated compared to the diffraction limit response, the spot diagrams in the UWF OCT system at the FOV of ≤60° were diffraction-limited or near diffraction-limited. Therefore, to evaluate the optical performance of the UWF OCT system more accurately, the Strehl

ratio and Huygens PSF with consideration of diffraction were also analyzed here. In the Strehl ratio, the peak intensity of PSF was normalized to unity. In the handheld OCT/OCTA system with 55° FOV, the optical aberrations would severely degrade the transverse resolution and compromise the image quality when the FOV was larger than 40° as shown in Figure 3.2(A). Employing adaptive optics into the probe was difficult due to the size constraint. For this reason, the OCT imaging system with lower system aberrations at the wide FOV became more desirable. As shown in Figure 3.2(B), although we started noticing the aberrations at ≥60°, they were not as severe as the 55° FOV system. The UWF OCT imaging system with the novel optical design proposed in the letter not only reduced the aberration at the same FOV but also enlarged the FOV remarkably.

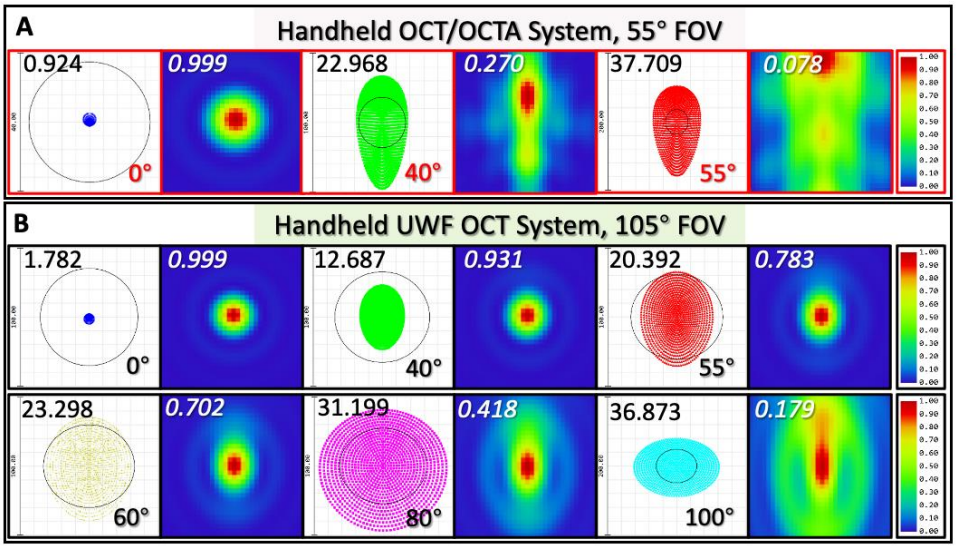

Figure 3.2 Spot diagrams and Huygens point spread functions (PSF) from our established system [12] (A) and the UWF OCT system (B) with different FOV. The scale is 200 μm in the spot diagram for both systems. The radius of the Airy Disk (black circle) is 17.06 μm (55° FOV), and 31.77 μm (105° FOV). The FOV configuration is shown in the bottom right corner of each spot diagram. The Strehl ratio is shown in the upper left of each Huygens PSF.

Although the bidirectional raster scan has less scanning distortion than the unidirectional raster scanning approach [44], it cannot skip scanning the four empty corners in UWF. To fully

utilize the scanner for UWF, we used a spiral scanning pattern that was first introduced by Oscar *et al.* for intraoperative OCT [70]. The spiral scan at constant linear velocity was performed with 608,400 A-scans (with equal radian and azimuthal spacing at 24.4 μm) per volume in this study. Each volume acquisition time was 1.52 seconds.

OCT images were acquired, processed, and displayed in real-time with our GPU-accelerated software OCTViewer [49], which facilitated the alignment process and provided immediate data quality assessment. The imaging sessions were conducted after the patients were dilated with cyclomydril and the whole session was completed within 5 minutes to minimize discomfort for the subjects. Each session started in high-speed alignment mode with a 10 Hz volume rate to locate and align the area of interest. Once the target area was on the ocular fundus, autofocusing was performed in 1 second based on the brightness of the *en face* images with a hill-climbing algorithm [51]. Then, we switched to the spiral scan to acquire OCT data. Remapping of the spiral scanning *en face* images was implemented by nearest-neighbor algorithm in real-time, and by cubic scattered data interpolation in post processing (function griddata in MATLAB).

3.4 Results and Discussion

In this study, 3 healthy adult volunteers (24-34 years old) and 31 pediatric patients (less than 6 months old) were imaged with the handheld UWF OCT system. All the subjects were recruited from the Casey Eye Institute at the Oregon Health & Science University (OHSU). The research was approved by the Institutional Review Board/Ethics Committee of OHSU following the Declaration of Helsinki.

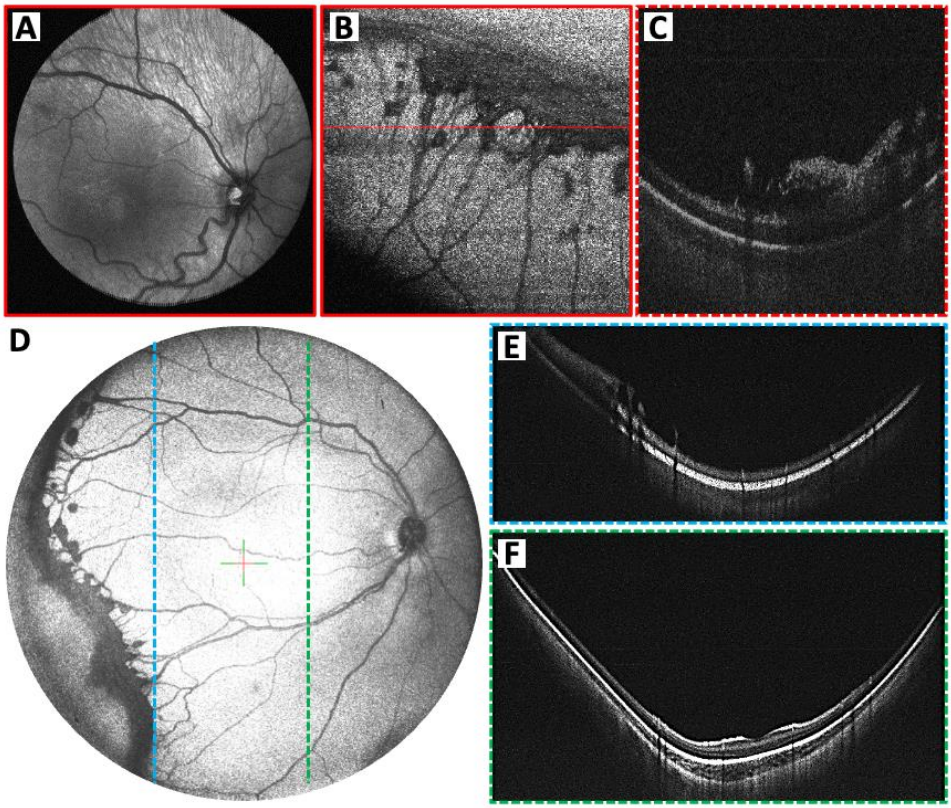

Figure 3.3 The *en face* OCT images of the retina posterior pole from an awake neonate (A) and peripheral retina (B) using scleral depression acquired by 55° handheld OCT/OCTA system [69]. (C) Selected B-scan [red line in (B)] reveals neovascularization. (D) *En face* OCT image with clear demarcation line from another infant (ROP stage 3) with extraretinal neovascularization acquired by the handheld UWF OCT. (E) Selected B-scan with neovascularization [cyan dashed line in (D)]. (F) Another selected B-scan across the macular region [green dashed line in (D)].

Imaging the peripheral retina is essential to evaluate the severity of ROP. Peripheral pathology can be difficult, if not impossible to fully appreciate with standard FOV OCT. Previously, our clinical team has been able to visualize the retinal periphery using scleral depression with our 55° handheld OCT/OCTA system [71], as shown in Figure 3.3(A)-Figure 3.3(C), but the ability to acquire imaging of the posterior pole and peripheral retina in a single, continuous scan could greatly improve the diagnosis of retinal diseases [Figure 3.3(D) - Figure 3.3(F)]. Using the handheld UWF OCT, we screened a similar area of a patient presented with

ROP stage 3 by both bidirectional raster scans (800 A-scans/B-scan, 780 B-scans/Volume, total of 624,000 A-scans/Volume) [Figure 3.4(A)] and spiral scan (608,400 A-scans/Volume) [Figure 3.4(B)]. In the bidirectional raster scan, we noticed the scanning artifacts shown in red arrowheads in the zoomed-in inset of Figure 3.4(A). These scanning artifacts were produced by sharp change of directions in the fast axis (vertical direction) and hysteresis of the scanners. The distortion was not present when using the spiral scan, as seen in the zoomed-in inset of Figure 3.4(B). The bidirectional raster scan protocol usually scanned the entire square area; thus, 21.5% of A-lines allocated in the four corners [white arrows in Figure 3.4(A)] would be wasted. In contrast, all A-lines were allocated to the sample using the spiral scan. With the same number of A-lines per volume, the sampling density in the spiral scan is higher than in the bidirectional raster scan. Assuming that the infant eye length was 17 mm, the scan region with approximately 21.5 mm diameter could be obtained with the 105° FOV. If 608,400 A-lines per volume were implemented in these two scanning protocols, then the scan interval for spiral scan and raster scan would be 24.4 μm and 27.5 μm respectively.

Figure 3.5 shows the RetCam color fundus image [Figure 3.5(A)], fluorescence angiogram image [Figure 3.5(B)], *en face* OCT image [Figure 3.5(C)] and two represented B-scans [Figure 3.5(D) and Figure 3.5(E)] obtained by our handheld UWF OCT system from a premature infant with ROP after laser treatment. The *en face* OCT image covered an area of the retina comparable to the RetCam fundus image, which is stated to have a 130° FOV. Laser treatment is often effective in reducing neovascularization, but some patients may experience recurrence, resulting in vascular dragging, retinoschisis, and retinal detachment [53], all of which are more easily appreciated on OCT images.

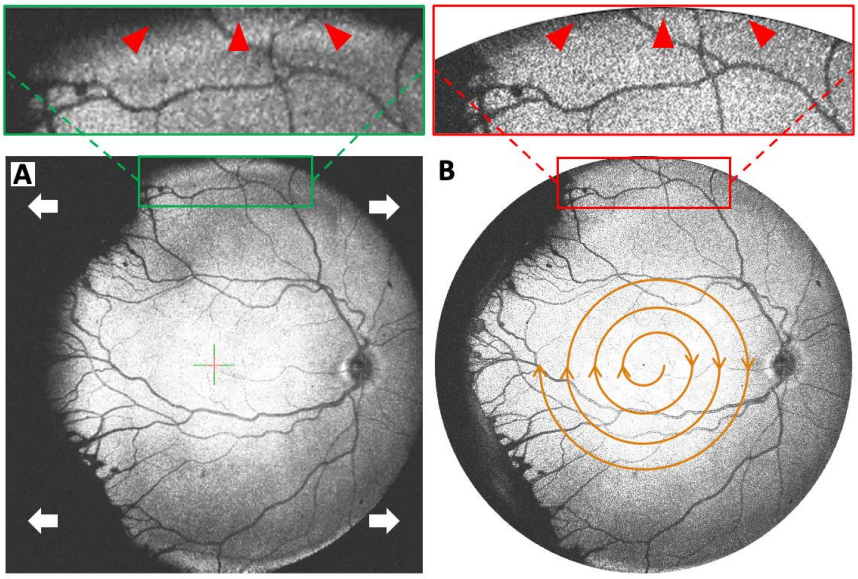

Figure 3.4 (A) *En face* OCT image acquired by bidirectional raster scan. The white arrows denote the four empty corners unavoidable in the bidirectional raster scan. (B) *En face* OCT image acquired by spiral scan. The zoomed-in insets show the comparison of the edge of the scanning area. Note that the fast scan direction is vertical in the raster scan (A), and the galvanometer scanner turning points are at the top and bottom of the image.

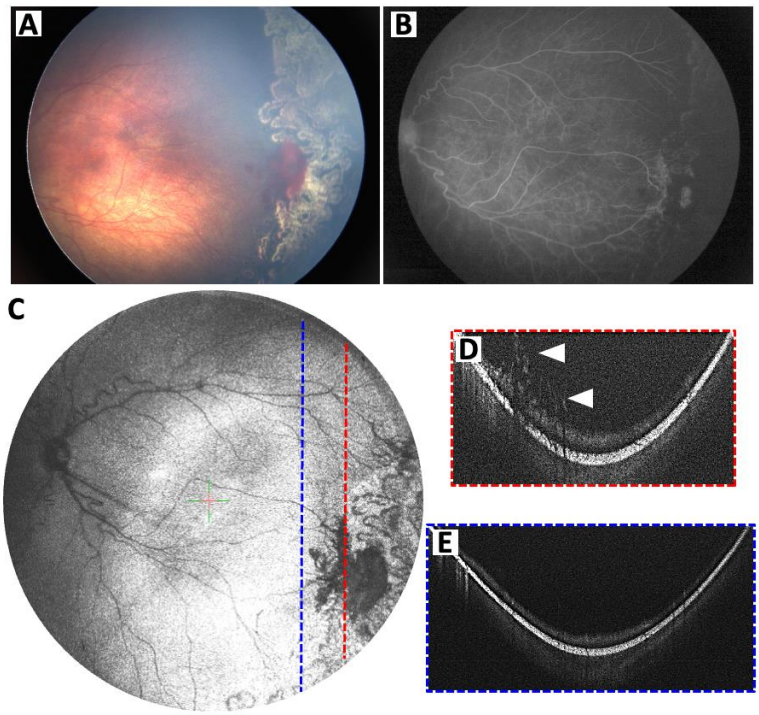

Figure 3.5 (A) RetCam color fundus image from an infant with ROP stage 3 after laser treatment. (B) RetCam fluorescein angiogram image. (C) *En face* OCT image acquired by handheld UWF OCT. (D) Selected B-scan [red dashed line in (C)] reveals neovascularization. (E) Selected B-scan [blue dashed line in (C)] without apparent neovascularization.

The novel optical design of the probe in this letter significantly improved the optical performance in terms of extending the FOV and controlling the system's aberrations. In the representative *en face* OCT images shown above, there were no pronounced motion artifacts. Although our UWF OCT imaging system was able to acquire a larger area in a single shot compared to our previously published handheld OCT/OCTA system, we did not implement the OCTA scanning pattern in the UWF OCT system due to the constraints of speed and transverse resolution. Resolving capillaries with OCTA requires higher sampling density and higher transverse resolution, which are not currently available in our system. Volume acquisition time within 1~2 seconds is practical in clinical application. A higher sampling density would lead to a longer volume acquisition time and more severe motion artifacts, which can be mitigated by using a faster-swept source laser. However, the SNR of the OCT signal inevitably decreases with increasing speed; under the current 1.8 mW laser safety protocol, an OCT system with a speed above 1 MHz might only lead to diminishing returns [72]. In addition, a larger beam on the pupil will in theory provide better transverse resolution; however, without a better optical design, further increasing the numerical aperture will only lead to larger optical aberrations and possibly lower transverse resolution.

Although the current imaging range of 6 mm in the air was sufficient in most cases, careful adjustment was required to avoid aliasing artifacts during scanning. A longer imaging range without appreciable sensitivity roll-off is desired as it facilitates the alignment process, particularly in the UWF imaging application because of the larger retinal curvature compared to the regular

FOV imaging. Moreover, the UWF design further shortens the working distance. With these limitations, the operators have reported that the UWF design is more challenging to align.

3.5 Conclusion

Nevertheless, in this study, we achieved the widest FOV among all portable retinal OCT imaging research prototypes and commercial systems. Compared to the 100-degree desktop retinal imaging system with MHz FDML light source [73], our solution has significantly higher SNR, longer imaging range, and higher quality optics close to the diffraction limit across the entire FOV. The *en face* images presented show the microvascular abnormalities extending from the posterior pole to the peripheral retina in a single capture without pronounced motion artifacts. The spiral scan with real-time visualization was employed here to acquire UWF OCT images. Handheld UWF OCT imaging technology with a non-contact approach and fast acquisition time has the potential to be widely used in the evaluation of pediatric retinal diseases.

CHAPTER 4. NON-MYDRIATIC ULTRA-WIDEFIELD DIFFRACTION-LIMITED RETINAL IMAGING

4.1 Abstract

We demonstrate a new non-mydriatic ultra-widefield optical coherence tomography retinal imaging system, designed with custom optics to improve the imaging field of view (FOV), lateral resolution, and patient comfort. The key motivation is to address the challenge with conventional systems which require pupillary dilation, adding time, expense, discomfort, and medical risk to the examination of the retina. Our system provides an ultra-wide 100° FOV (visual angle measured from the pupil plane) and maintains a lateral resolution of 20 μm on the center. It also allows a generous working distance of 16 mm, 2-3 times longer than existing ultra-widefield OCT imaging systems. This advanced system was able to avoid iris vignetting artifacts without pharmacological dilation and ensure diffraction-limited ultra-widefield imaging. This enables comprehensive evaluation of retina diseases, especially those affecting the peripheral regions.

4.2 Introduction

Optical coherence tomography (OCT) has revolutionized the field of ophthalmology, offering high-resolution, cross-sectional images of the retina, thereby significantly enhancing diagnostic capabilities [5,74]. The integration of ultra-widefield imaging in OCT is transformative for comprehensive retinal assessments, especially in the diagnosis and management of peripheral retinal pathologies such as retinal tears, retinal detachment, and retinopathy of prematurity [12,75–

This work has been published in Optics Letters.

Shuibin Ni, Ringo Ng, David Huang, Siyu Chen, Benjamin K. Young, J Peter Campbell, and Yifan Jian, "Non-mydriatic ultra-widefield diffraction-limited retinal imaging," Opt. Lett. 49(14), 3902-3905 (2024).

78]. Traditionally, OCT systems have a restricted field of view (FOV), limiting peripheral retinal evaluations. The gap in this imaging capability has led to a growing interest among both commercial and research groups in developing OCT systems with an expanded FOV [73,79,80]. One of the most prevalent challenges encountered with ultra-widefield ophthalmic devices is iris vignetting due to the beam wandering on the pupil plane when the scanning angles increase [81], which the conventional designs with off-the-shelf optics fail to effectively address [79,80]. Conventional ocular examinations, including both ophthalmoscopic evaluation and fundus imaging, typically necessitate pupil dilation. However, this practice entails additional risks for the patients, as well as increased procedural time and costs. Mydriatic medications result in photophobia and blurry vision for patients for several hours and are rarely associated with a spectrum of systemic side effects - such as compromised gastrointestinal motility, tachycardia, and psychological agitation - owing to their non-selective anticholinergic properties [82].

In this study, we proposed an innovative optical design with custom optics for an ultra-widefield OCT imaging system to work effectively without the need for pharmacological dilation, facilitating the safe and effective implementation of ultra-widefield imaging. The system, with an extensive FOV of 100° (visual angle measured from the pupil plane) and a high lateral resolution of 20 µm, provides an effective approach to retinal imaging, particularly in assessing peripheral retinal pathologies.

4.3 Methods

In an OCT retinal imaging system, two orthogonal scanners are typically separated by 5 to 10 mm. This separation causes beam wondering on the pupil plane, and this effect is exacerbated in ultra-widefield laser scanning retinal imaging systems [69,79]. The telecentric relay lens system between the scanners, as indicated in Figure 4.1(A), can ensure the galvo scanners are optically

conjugated, therefore eliminating the gap between the scanners. We custom-designed a telecentric relay lens system with a multi-element combination, which has proven effective in managing beam wandering on the pupil plane [83].

There are several well-known challenges and trade-offs in the design and manufacture of ultra-widefield eyepiece optics. In macular imaging, where scanning angles are typically within ~40° (±20°), beam wandering on the pupil plane is negligible even without separating the two galvo scanners, therefore most macular OCT scanners do not require pupil dilation [Figure 4.2(C)]. However, at larger angles over 80°, beam wandering becomes apparent, leading to iris vignetting when patients are not dilated under natural lighting conditions. Another key issue with larger angles is that the Petzval field curvature does not align with the retinal curvature. Petzval field curvature is a type of optical aberration that occurs in imaging systems and causes the image plane, where all the points of focus converge, to have a curved shape rather than being perfectly flat. Typical photography lens design strives to eliminate the Petzval field curvature due to the flat imaging sensor. However, in ultra-widefield retinal imaging, ideally, the Petzval field curvature should overlap with the retina curvature, a challenging task that most widefield retinal imaging system fails to deliver, as illustrated in Figure 4.2(A). Additionally, in previous designs, larger scanning angles caused beam shape alterations from circular to elliptical on the pupil plane, particularly at scanning angles over 80° [Figure 4.2(C)], resulting in decreased beam quality and resolution.

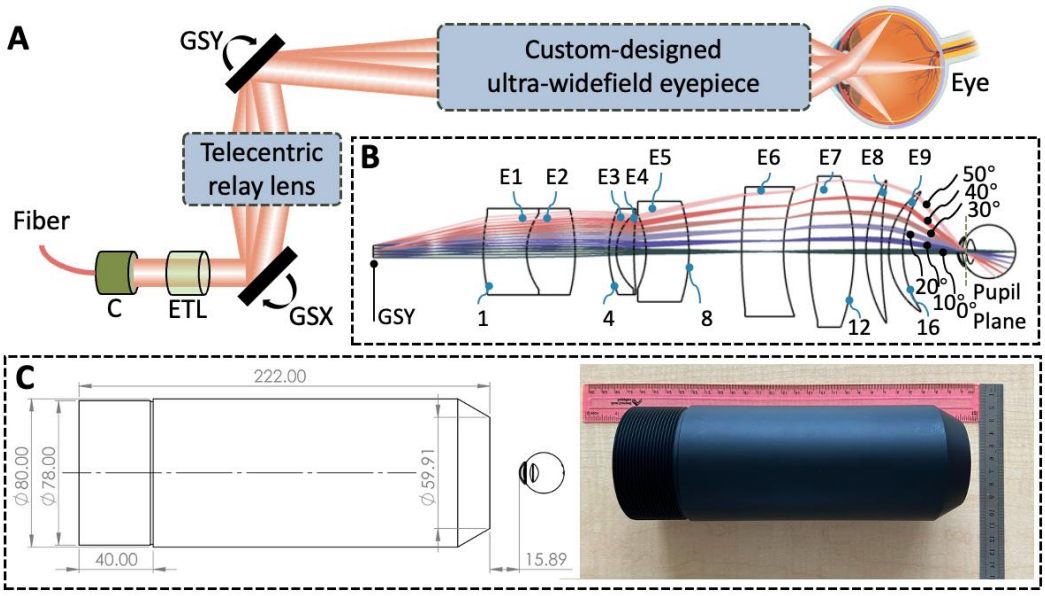

Figure 4.1 Optical design of sample arm. (A) Schematic of the portable probe, showing components C (collimator), ETL (electrically tunable lens), and GSX/GSY (galvo scanners for fast/slow axes). The electrically tunable lens is mounted horizontally to avoid the gravity effect on the lens shape and its optical performance. (B) Ultra-widefield eyepiece design, with surface specifications and materials for elements E1-E9 in Table 4.1. Scanning angles represent half of the total FOV. The telecentric relay lens design was described in our previous work [83]. For clarity, only the ultra-widefield eyepiece design is depicted in the current optical layout. Note that the evaluations of optical performance were conducted on the complete system, not solely on the ultra-widefield eyepiece component. (C) Left: Mechanical design of eyepiece lenses, optimized for maximum working distance to avoid eye socket contact. Right: Photograph of eyepiece lenses produced by Avantier Inc., USA, with dimensions in millimeters.

To extend the FOV while maintaining excellent optical performance, a specialized ultra-widefield eyepiece was developed, as depicted in Figure 4.1(A). The optical design was developed and optimized using Zemax OpticStudio software (Ansys Inc., USA). The eyepiece magnification determines the beam diameter on the pupil plane and the required scanning angles of the galvo mirrors. Increased magnification is inversely proportional to the beam size on the pupil, resulting in a decrease in the lateral resolution, therefore impacting the ability to resolve fine retinal

structures. In contrast, reduced magnification demands wider scanning angles from the galvo scanners. The wider angular range requires lenses with larger diameters, and further limits the galvo scanning speed. Hence, a critical design trade-off is imperative in the development of the ultra-widefield eyepiece. In our specific design, the eyepiece magnification is set at 3.6×, amplifying the optical angle from 28° (provided by the galvo scanners) to 100° before entering the pupil, with the maximum lens aperture less than 60 mm in diameter [E7 in Figure 4.1(B)]. With a 4.2 mm beam diameter from the collimator (RC04APC-P01, Thorlabs Inc., USA), the beam size is reduced to 1.1 mm on the pupil plane. This leads to a theoretically focused spot size of 20.5 μm ($1/e^2$ diameter) on the retinal plane, achieving a balance between expansive FOV with high-resolution imaging. Moreover, the ultra-widefield eyepiece has a Petzval field curvature aligned with the retinal curvature, ensuring uniform image resolution over the entire FOV. We used the Gullstrand-LeGrand eye model for simulation, tailoring the curvature to match an adult human eye [84]. The tailored design effectively reduces elliptical distortion in beam bundles from off-axis angles, enhancing performance at maximum scanning angles [Figure 4.2(D)]. The specifications for the ultra-widefield eyepiece lenses are detailed in Table 4.1.

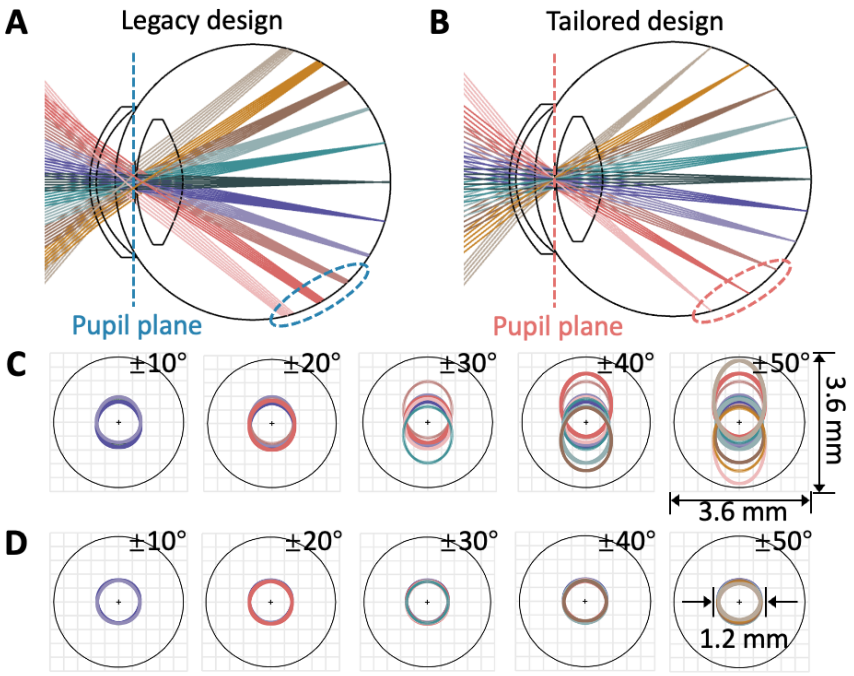

Figure 4.2 Beam wandering at the pivot point on the pupil plane. (A) Footprint details on the pupil plane for the previous design targeting 100° FOV. (B) Footprint details on the pupil plane using the current optical design with custom optics. Beam wandering on the pupil plane for legacy design (C) and for tailored design (D) across increasing scan angles. The tailored design restricts beam wandering within a 1.2 mm aperture, whereas the legacy design shows beam wandering up to 3.4 mm. Scale bars denote 3.6 mm (aperture diameter of 3.4 mm).

Table 4.1: Lens data of the custom eyepiece lenses (unit: mm)

Surface	Radius	Thickness	Material	Mech-Diameter
1	70.648	17.836	BAH26 (E1)	32.460
2	26.525	20.000	S-TIM6 (E2)	32.460
3	-72.643	13.956		
4	43.726	3.000	L-LAH94 (E3)	32.172
5	19.875	7.282	H-K7 (E4)	32.172
6	169.860	5.000		
7	-34.905	17.622	H-LAK3 (E5)	38.244
8	-67.624	21.705		

9	194.524	17.283	LACL1 (E6)	50.076
10	80.086	10.474		
11	115.272	18.494	CSBR (E7)	58.852
12	-91.886	5.000		
13	56.298	6.362	LAK9G15 (E8)	56.636
14	191.791	3.000		
15	29.896	5.785	ZNSE (E9)	47.506
16	42.764	22.460		

In practical optical systems, energy dispersion of an imaged spot often extends beyond the Airy disc, reducing the irradiance at the center of the point spread function (PSF). The Strehl ratio (SR) is particularly useful in assessing lens systems across various field angles, complementing wavefront aberration parameters. According to the Rayleigh Criterion, image quality is not significantly degraded if the peak-to-valley (PV) wavefront error does not exceed λ/4, corresponding to a root mean square (RMS) wavefront error of λ/14 or less, and a Strehl ratio of at least 0.8. Figure 4.3 illustrates the system's optical performance on the retinal plane across a range of scan angles. The system consistently operates within the diffraction limit for wavelengths from 1010 nm to 1100 nm at all scanning angles [Figure 4.3(A)].

To assess the stability of the pivot point across scan angles, we utilized a beam profiler (Beam Profiler 4M, Edmund Optics Inc., USA) at the estimated pivot point. Initial positioning was based on the working distance [Figure 4.1(C)], with adjustments made to reduce beam wandering during galvo mirror scanning. Figure 4.4(A) shows the beam intensity distribution on the sensor along the x-axis, y-axis, and at 45° to these axes, adjusted through galvo scanner offsets. The bottom right image in Figure 4.4(A) presents an aggregated beam profile, demonstrating minimal wandering and confirming the simulation results [Figure 4.2(D)]. The sensor's scale, cropping to

1.5×1.5 mm, is compatible with average adult constricted pupil size [85], supporting the system's applicability for non-dilated retinal imaging. Optically, combining multiple low-power lenses reduces aberrations and increases design flexibility but also adds reflective surfaces. To mitigate reflective losses, a custom anti-reflection coating was applied to all lens surfaces, reducing reflectivity to below 0.5% for 980 to 1200 nm wavelength. Transmission efficiency measurements [Figure 4.4(C)] showed over 85% efficiency across all field angles for the relay lenses [83] and eyepiece lenses.

A custom-designed aluminum mounting plate houses the reflective collimator and aligns the relay lenses between the galvo scanners and eyepiece under the optimized optical design. Figure 4.5(A) displays the fully assembled system, equipped for *in vivo* imaging. The system utilizes swept-source OCT technology, described in detail in [69,79,80]. The optical power on the cornea is 2.0 mW, adhering to the ANSI Z80.36-2021 standards [52]. Volumetric captures comprise 1680 B-scans, each with 1600 A-scans, and the total acquisition time is 6.7 seconds. Images were acquired and processed using our specialized GPU-accelerated OCTViewer software, facilitating real-time qualify assessment [49,51].

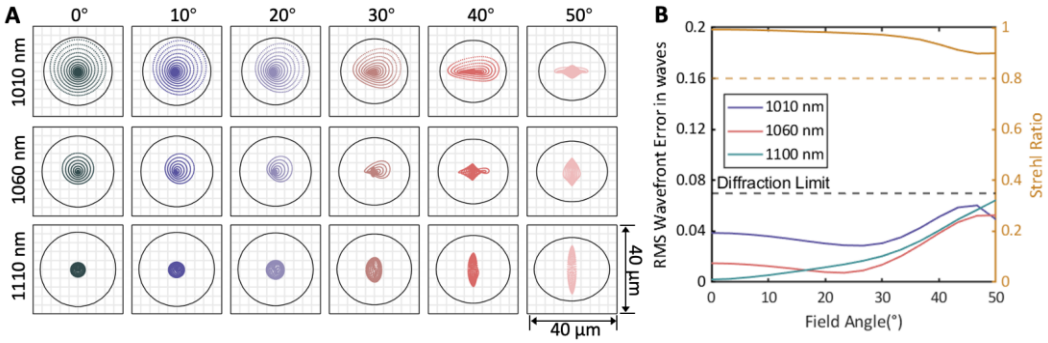

Figure 4.3 Optical performance simulation on the retinal plane. (A) Matrix spot diagrams at 1010 nm, 1060 nm, and 1110 nm for different scan angles. Black circles represent the Airy disk, with Airy radii in different wavelengths of 13.86 μm, 14.55 μm, and 15.24 μm, respectively. Scale bars are 40 μm. (B) Field angle with associated wavefront aberrations, measured by RMS and SR values. The field angle is oriented along the +y direction.

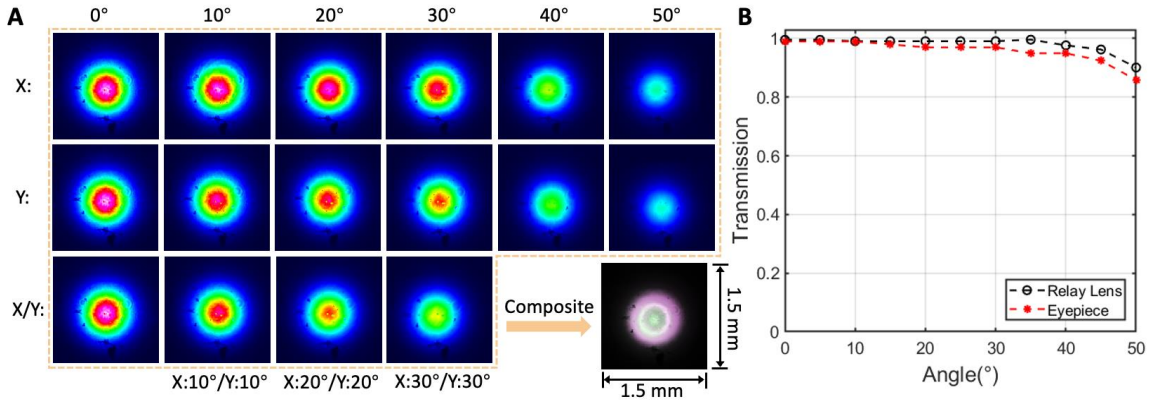

Figure 4.4 Pivot point stability and transmission efficiency. (A) Two-dimensional beam intensity distribution at various galvo positions, sensor size 1.5×1.5 mm. A composite beam profile was created by integrating all offsets from the galvo scanner. (B) Transmission efficiency across FOV for custom relay lenses (black circle) and eyepiece lenses (red star).

4.4 Results and Discussion

Seven healthy adults and one patient were recruited from the Casey Eye Institute at Oregon Health & Science University (OHSU) for a pilot study. The OHSU Institutional Review Board/Ethics Committee-approved study conformed to the Declaration of Helsinki, with participants providing informed consent. The group included 5 males and 3 females, aged 23 to 44 years, with an average age of 32.5±5.2 years. Of these, five (3 males, 2 females) had myopia ranging from -6.5 to -1.5 diopters. Imaging was conducted without pharmacological dilation, yielding comprehensive ultra-widefield images without pupillary vignetting artifacts.

Figure 4.5(B)-Figure 4.5(G) demonstrate *en face* OCT images at different retinal depths within a healthy subject. The *en face* projection OCT image reveals individual nerve fibers, as shown in Figure 4.5(B). Figure 4.5(D) provides an enlarged view highlighting the temporal nerve fiber raphe on the fovea. Figure 4.5(E) shows three averaged B-scans focused on the fovea, with the scan location indicated by the gray dashed line in Figure 4.5(B). Two vortex ampullas are identified in Figure 4.5(F), marked by blue arrowheads. These depth-specific, color-coded

structural images are merged in Figure 4.5(G), resulting in a composite that closely resembles a color fundus photograph.

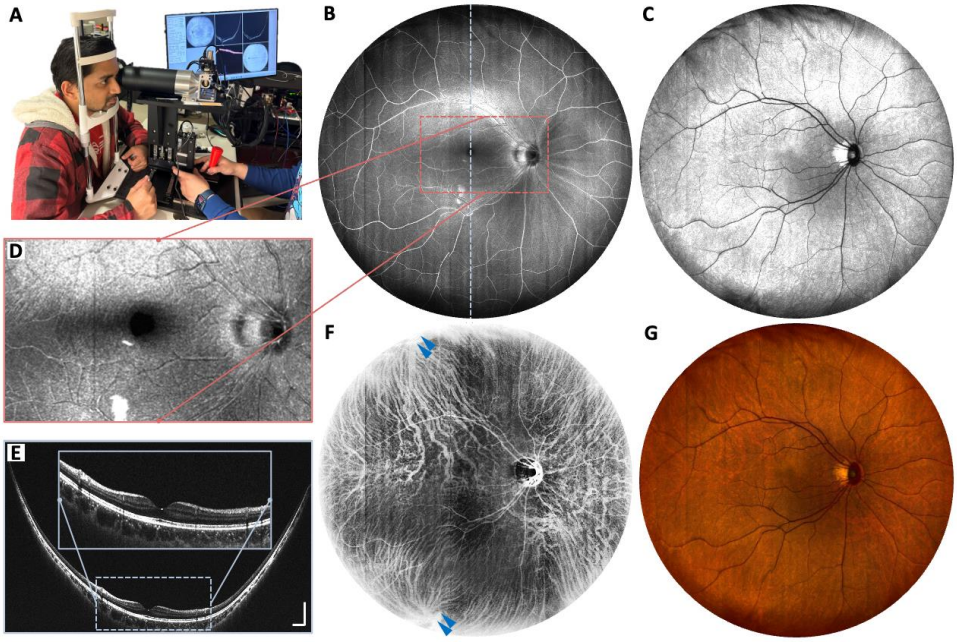

Figure 4.5 Non-mydriatic ultra-widefield OCT imaging in a healthy adult. (A) The assembled system during *in vivo* imaging. (B) Nerve fiber layer *en face* projection. (C) Outer retina OCT *en face* structural image. (D) Enlarged view of the nerve fiber layer projection within the red dashed box in (B). (E) Fovea-centered, averaged (3 frames) B-scan indicated by the gray dashed line in (B). Scale bars: vertical 500 µm; horizontal 1 mm. (F) Inverse choroidal OCT *en face* structural image with vortex ampullas (blue arrowheads). (G) Color-coded OCT *en face* image.

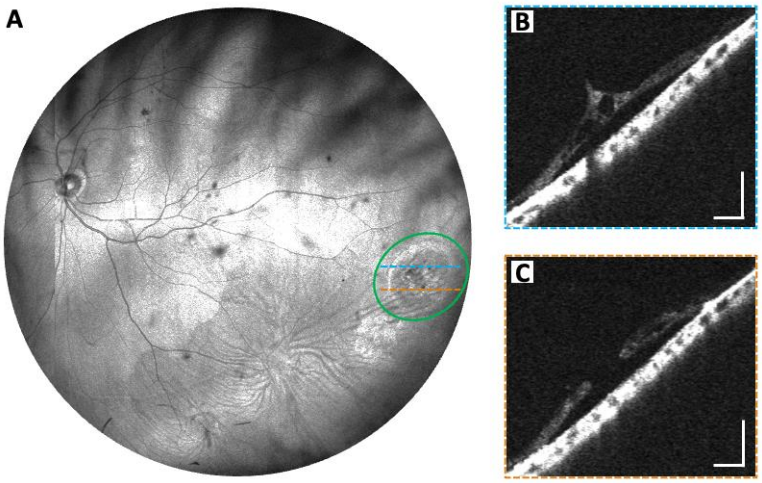

Figure 4.6 Non-mydriatic ultra-widefield OCT imaging in a patient (-6.0 diopters) with a treated retinal hole. (A) OCT *en face* image (B) B-scan showing vitreous traction, not previously identified in clinical exams. (C) B-scan of a full thickness hole with subretinal fluid. Scale bars: 500 µm.

Figure 4.6 provides *en face* OCT images from a patient with myopia of -6.0 diopters, who was treated for a retinal hole. While serial clinical exams had not previously identified any traction, the prototype utilized in this study revealed clear vitreous traction and a full-thickness hole with subretinal fluid, as depicted in Figure 4.6(B) and Figure 4.6(C), highlighting the significant clinical value of our system.

In OCT, aberrations impact not only resolution but also collection efficiency, leading to a reduced signal-to-noise ratio [86]. This effect is exacerbated at larger scanning angles [73,79]. Our OCT *en face* structural image [Figure 4.5(B)] exhibits minimal signal intensity reduction at the edges, indicating effective mitigation of angle-dependent optical aberrations and nearly isotropic backscattering properties of retinal tissue. However, we cannot compensate for individual ocular aberrations due to anatomical variability, with subject axial lengths in our study ranging from 22.5 to 26 mm, where adaptive optics technology is needed [60,62,87]. Panretinal imaging up to 140° FOV has been achieved [80], but requires a contact lens, making it challenging for awake adult patients. Our non-contact approach improves patient comfort. However, increasing the FOV non-invasively may impact working distance or necessitate larger lenses.

Despite advancements, our system faces limitations. The Gullstrand-LeGrand eye model employed in our simulation exhibits inherent simplicity, which limits its efficacy, particularly in the simulation of the eye's peripheral regions. In contrast, the Polans widefield model offers a more detailed and realistic depiction of the human eye, potentially making it better suited for our application [88]. Future studies will involve comparative analyses between these models to further assess their applicability and performance. Additionally, maintaining both high lateral optical

resolution and Nyquist sampling density is critical for high-quality imaging. This requires an OCT system with an A-scan speed of 1.2 MHz, enabling an acquisition time of 6.5 seconds with a 100° FOV, 20 µm transverse resolution, 2800 A-scan/B-scan, and 2800 B-scans/Volume. At a 400 kHz A-scan rate, the system is suboptimal for OCT angiography without pupil tracking, and the current scan duration is too long for practical clinical use, with the potential for motion artifacts. Rapid, isotropic sampling is crucial for clinical application, and the current speed may be insufficient for this purpose. Moreover, the advantages of aligning Petzval curvature with retinal curvature have not been conclusively demonstrated, as the efficacy of this approach may vary with axial eye length. Ongoing clinical trials are being conducted to assess the practical feasibility and effectiveness of the method.

4.5 Conclusion

In conclusion, our prototype achieves an FOV up to 100° with a 16 mm working distance, without requiring mydriasis. Custom optics in relay and eyepiece lenses enable diffraction-limited performance across all field angles, with a lateral resolution of 20 µm. This enhances peripheral retina visualization, offering a more comprehensive assessment of retina health.

CHAPTER 5. PANRETINAL OPTICAL COHERENCE TOMOGRAPHY

5.1 Abstract

We introduce a new concept of panoramic retinal (panretinal) optical coherence tomography (OCT) imaging system with a 140° field of view (FOV). To achieve this unprecedented FOV, a contact imaging approach was used which enabled faster, more efficient, and quantitative retinal imaging with measurement of axial eye length. The utilization of the handheld panretinal OCT imaging system could allow earlier recognition of the peripheral retinal disease and prevent permanent vision loss. In addition, adequate visualization of the peripheral retina has a great potential for better-understanding disease mechanisms regarding the periphery. To the best of our knowledge, the panretinal OCT imaging system presented in this manuscript has the widest FOV among all the retina OCT imaging systems and offers significant value in both clinical ophthalmology and basic vision science.

5.2 Introduction

Many vitreoretinal disorders can manifest with morphological abnormalities in both the posterior pole and the peripheral retinal capillary network at an early stage [71,76,89–92]. In the adult retina, most tractional and rhegmatogenous retinal detachment are due to peripheral pathology, such as extraretinal neovascularization, membranes, and retinal breaks. In addition, much of the pathology in common retinal vascular diseases such as diabetic retinopathy involves the peripheral retina. Infants with diseases that affect the peripheral retina, such as retinopathy of

---

This work has been published in IEEE Transactions on Medical Imaging.

Shuibin Ni, Thanh-Tin P. Nguyen, Ringo Ng, Mani Woodward, Susan Ostmo, Yali Jia, Michael F. Chiang, David Huang, Alison H. Skalet, J. Peter Campbell, and Yifan Jian, "Panretinal Optical Coherence Tomography," IEEE Trans. Med. Imaging 42(11), 3219–3228 (2023).

prematurity (ROP), Coats disease, retinoblastoma, *etc.*, are often not noticed until their vision in one or both eyes is severely impaired. Imaging technology with adequate visualization of both central and peripheral regions of the retina is desirable for early diagnosis and treatment of these eye diseases, may prevent visual impairment, and could even improve mortality rates such as in patients with retinoblastoma. However, capturing images of the peripheral retina has been challenging, especially in pediatric populations. In addition to visualization of the retinal periphery, ocular biometry (measurement of axial eye length) is required for quantitative measurement of anatomic features on the retina and may aid the understanding of retinal disease and evaluating eye health.

There are very limited commercially available retinal imaging devices that can visualize peripheral retina. Scanning laser ophthalmoscopes (SLO) such as Optos ultra-widefield retinal imaging and Heidelberg SPECTRALIS with ultra-widefield modules have a field of view (FOV) up to 200° (measured from the center of the eyeball) and are frequently used in ophthalmic clinics. These imaging devices are in desktop format, bulky, and require patient cooperation including maintaining a steady position of gaze. It is possible to image infants with these desktop systems in the so-called “flying baby” position in which they are held by the photographer. However, this requires significant operator skills and experience, and is not widely available. Handheld fundus cameras (RetCam Envision, Natus Medical Inc., Canada) are increasingly being used in managing pediatric retinal diseases due to their portability. Compared to the SLO, fundus cameras have inherently low contrast and resolution due to the lack of confocal pinholes to reject scattered light. Another limitation of portable fundus cameras is their smaller FOV, limited by the size and illumination scheme.

Optical coherence tomography (OCT) is a non-invasive imaging technology used to acquire detailed information on ocular structures by the interferometric detection of the back-reflected light [5]. OCT has revolutionized ophthalmic imaging and transformed clinical practice in ophthalmology. However, most of OCT retinal imaging systems including both commercially available units and research prototypes do not provide imaging FOV over 100° [8,11,15,16,42,69]. In conventional implementation of a retinal OCT system, it is possible to adjust the combination of the focal length and diameter of the lens in the eyepiece to obtain a relatively large FOV [42,93]. However, the working distance limits this strategy when the FOV is over 100°. Alternatively, multiple images can be stitched together. This method relies on patient cooperation to adjust gaze toward various target points to capture the peripheral fields. This issue, together with the need for a particularly skilled operator, and extended acquisition time make the stitched image solution impractical. In general, desktop OCT retinal imaging systems require patients to fixate and maintain their postures steady, which significantly limits their use in imaging infants and small children. To address this issue, several groups have reported on handheld OCT prototypes for imaging patients in the supine position [7–16,69]; however, most of these portable prototypes cannot capture the posterior pole and peripheral retina in a single image, significantly limiting their clinical applications.

Beyond the challenges in acquiring useable widefield retinal images, another limitation of the above-mentioned retinal imaging devices is that these devices cannot accurately measure the anatomical features on the retina, due to the lack of eye axial length (AL) measurement. AL measurement allows for reliable quantitative analysis of ocular structures, which is important for accurate diagnosis and monitoring of eye diseases. A-scan ultrasound biometry has traditionally been the most used method for AL measurement but comes with the limitation of poor image

resolution [94,95]. OCT imaging technology can provide much higher image resolution and has been used in ocular biometry measurement including axial eye length [96,97]. However, conventional OCT is not suitable for AL measurement due to the limited imaging depth and displacement error of the scanning pivot point during image acquisition.

The inability to capture the peripheral retina efficiently and reliably and the absence of quantitative evaluation of changes in the peripheral retina have limited the thorough investigation and diagnosis of peripheral retinal diseases. In this manuscript, we introduce a contact handheld swept-source OCT (SS-OCT) system with an unprecedented single shot 140° FOV and demonstrate its use in a variety of retinal diseases. Imaging with a contact-based approach allows maximal control over eye position, eliminates the need to manually adjust the scanner's working distance, and is familiar to photographers and clinicians who manage pediatric retinal diseases and utilize fundus photography. With the new contact imaging probe design, we were able to significantly reduce the time needed for alignment, improve image quality, and achieve higher success rate than our previous handheld OCT imaging systems [11,69,79]. Importantly, the utilization of a contact approach also allows quantitative analyses of retinal pathology to further our understanding of morphologic and functional aspects of various retinal diseases. To the best of our knowledge, this is currently the widest FOV achieved among all retinal OCT research prototypes and commercial systems in desktop and portable format.

5.3 Methods

5.3.1 System Setup

The swept-source laser in the system had an A-scan sweep rate of 400 kHz, 50% duty cycle, a center wavelength of 1060 nm, and ~70 nm bandwidth (6dB), which corresponded to an axial resolution of 7.06 μm in air. Each A-scan spectrum was sampled by 2048 points

corresponding to a peak sampling frequency of 1720 MHz and an imaging depth of 6 mm in air. The beam size on the pupil plane was 0.36 mm, resulting in a theoretical beam diameter of 45.3 μm ($1/e^2$) on the retina plane when imaging an infant with an AL of 17 mm. The output power from the handheld probe was 1.68 mW, which is well below the ANSI Z80.36-2021 standards for 1060 nm light [52].

A schematic diagram of the contact handheld panretinal SS-OCT system is shown in Figure 5.1. A software-controlled linear stage allowing high-precision positioning was integrated into the system to adjust the length of the reference arm. The motorized translational stage with built-in encoders provided position information, which was recorded along with the OCT images. The stage had an adjustable length range of 100 mm, allowing optical path length matching on both the cornea and the retina planes in patients of different eye sizes. An electrically focused tunable lens (EL-3-10, Optotune, Switzerland), which had a correction focal length range from -77 mm to 77 mm, was placed after the collimator to adjust the focal length dynamically.

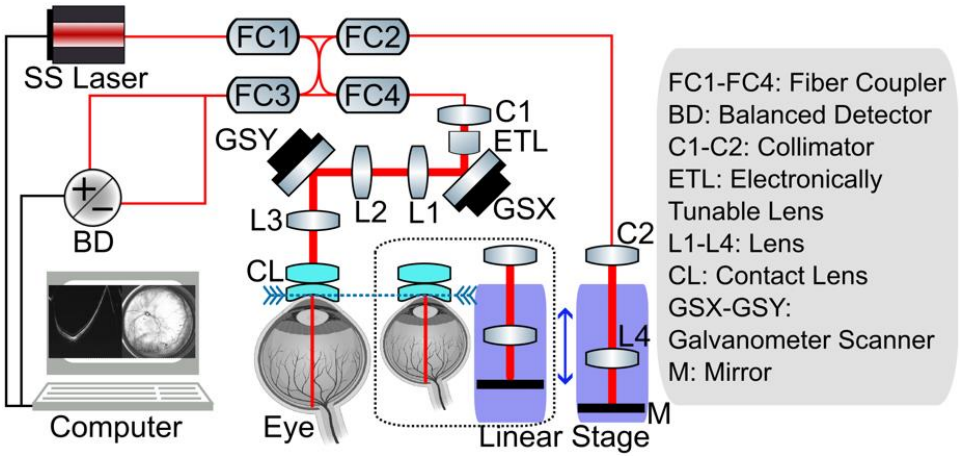

Figure 5.1 Schematic of contact handheld panretinal SS-OCT system. Swept-source laser (SVM10F-0210, Thorlabs Inc., USA); Split ratio of fiber coupler: FC1 (10/90), FC2 (50/50), FC3 (50/50), FC4 (20/80); Galvanometer scanner (Pangolin Laser System Inc., USA); Balanced detector (PDB482C-AC, Thorlabs Inc., USA); Linear stage (X-LHM100A-E03, Zaber Technologies Inc., Canada).

5.3.2 Portable Probe Setup

The transverse resolution of the OCT systems is determined by the numerical aperture (NA), and the optical aberrations in the imaging system and the ocular media. A retinal imaging system free of optical aberrations is diffraction-limited, which is predominantly determined by the beam size on the pupil plane and the refraction power of the eye. Ocular aberrations can vary significantly from person to person and can only be corrected by adaptive optics. However, in a low NA retinal imaging system, the ocular aberrations do not significantly impair the transverse resolution. While it is possible to design a diffraction-limited OCT imaging system with low NA over a moderate FOV, this task becomes increasingly difficult as the FOV expands. To meet the demand for ultrawide FOV, we first separated and placed the two scanners on the pupil conjugate planes with a set of relay telescopes (L1 and L2 in Figure 5.1, 4×AC254-035-B, Thorlabs Inc., USA). This ensured that the scanning beam pivot points of the two axes were overlapping, hence reducing vignetting artifacts. The telescope eyepiece was constructed with a pair of achromatic doublet lenses (L3 in Figure 5.1, 2×AC254-100-B, Thorlabs Inc., USA) and a contact ocular lens [CL in Figure 5.1 and Figure 5.2(A), Quad Pediatric, Volk Optical Inc., USA]. The Quad Pediatric lens was composed of an advanced double aspheric lens and a meniscus lens [Figure 5.2(A)]. The curvature of the meniscus lens was specifically designed for pediatric patients with small eyes, which maintained stability while ensuring the patients' comfort. The Quad Pediatric lens was commonly used in the application of indirect ophthalmoscopy with white light illumination. Therefore, the commercially available version has an anti-reflection (AR) coating for the visible wavelength range, which would greatly reduce the optical power when used in OCT imaging at 1060 nm. To improve the transmission in the infrared wavelength range, AR coating with

reflectivity < 0.5% from 950 nm to 1150 nm was applied on all the optical surfaces of the Quad Pediatric lens.

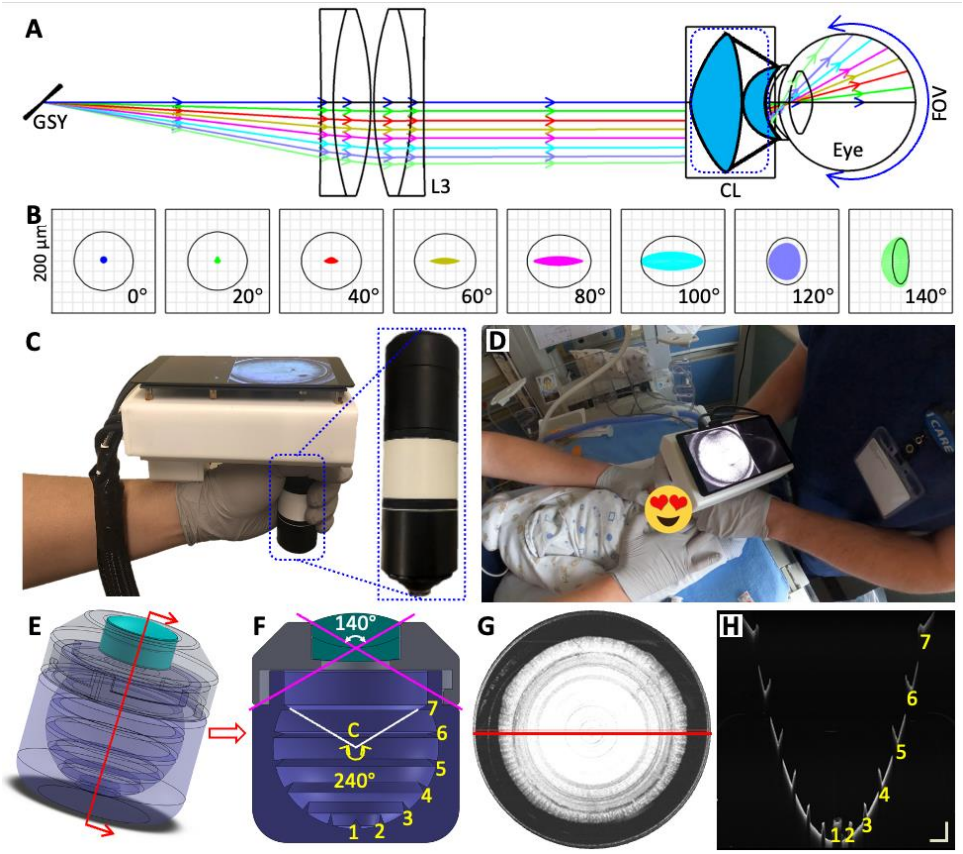

Figure 5.2 (A) 3D layout of telescope eyepiece design after the slow axis of the galvanometer scanner (GSY). (B) Spot diagrams of FOV from 0° to 140°. The black circle is the Airy disk. The complex double aspherical ocular lens induced some irregular beam profiles on the retina. (C) Photograph of the fully assembled portable probe. (D) Photograph of contact handheld SS-OCT being used to image premature infants in the OHSU neonatal intensive care unit. (E) SolidWorks rendering of phantom eye model for FOV calibration (radius=12 mm). (F) Cross-sectional view of the phantom eye. Seven circular rings extruded from the surface were marked. The interval between the rings was 40° measured from the center of the phantom eye (point "C"). (G) *En face* OCT image from the phantom eye. (H) Selected cross-sectional scan corresponding to the location of the red line in (G). Scale bars in (H) are 1 mm.

The novel optical design was developed and optimized in OpticStudio (Ansys Inc., USA). The spot diagrams were used to demonstrate and quantify the system's performance. Several

angular positions from 0° to 140° were chosen to investigate the influence of different FOVs on the performance of the system [Figure 5.2(B)]. The optimized Zemax simulation model was imported into CAD software (SolidWorks, Dassault Systèmes, France) for developing the mechanical design. The precise control over the distance between the lenses was delivered by the 3D printing [white parts in Figure 5.2(C)], which ensured that the system was always in optimum performance when the telescope eyepiece was removed for routine maintenance without the need of realignment.

5.3.3 Volumetric Imaging Field of View

The placement of the scanning pivot point [point "P" in Figure 5.3(B)] is of particular significance in the application of the panretinal OCT imaging system affecting the scanning FOV in all three dimensions. On the axial dimension, the light ray path difference between the central and the most peripheral ray [(r+d1-d2) in Figure 5.3(B)] determines the required imaging depth to fully accommodate the retina area being imaged. In this study, the eyeball was assumed to be an ideal sphere to simplify the model. At the same scanning angle [angle "θ" in Figure 5.3(B)], as the scanning pivot point moved posteriorly towards the retina, the curvature of the retina rendered in the cross-sectional scan would reduce, hence the required imaging range to fit the entire retina being scanned in one cross-section scan without aliasing artifact would gradually shorten. In general, cross-sectional scans have a flatter curvature when the scanning pivot point is placed towards the center of the eye [point "C" in Figure 5.3(B)]. In addition, the flatter retinal curvature would allow moving the entire cross-sectional scan towards the low-frequency part where the signal roll-off is at minimum, thus having a better signal-to-noise ratio (SNR). However, in panretinal OCT imaging, if the scanning pivot point is placed close to the center of the eye as in conventional OCT imaging, the OCT scanning beam entering the eye at large scanning angles will

be blocked by the iris, reducing the transverse FOV even when the pupil is fully dilated. With the contact approach, we could easily place the scanning pivot point on the pupil plane without manual adjustment of the working distance and achieve optimum transverse FOV. Commercial fundus camera (RetCam Envision, Natus Medical Inc., Canada) and scanning laser ophthalmoscope (Optos Inc., UK) measure the FOV from the center of the eyeball, whereas in our panretinal OCT scanner, we define our FOV as the scanning beam pivoting angle on the pupil plane.

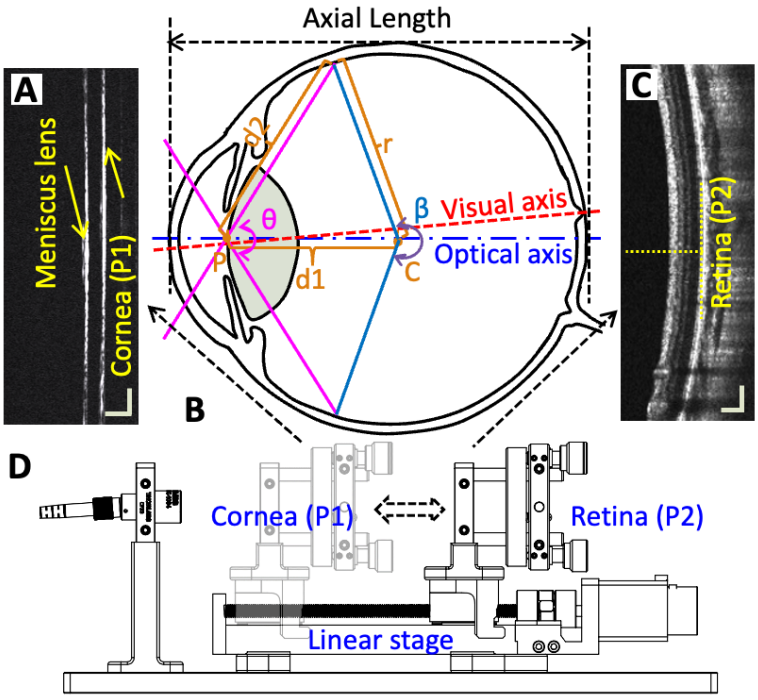

Figure 5.3 (A) Cross-sectional scan of the meniscus lens and corneal surface. (B). Schematic diagram of the human eye. P: scanning pivot point. θ: scanning angle. β: FOV measured from the center of the eyeball. C: center of the eye. r: radius of the eye. (C) Cross-sectional scan of the retina. (D) Schematic of the reference arm indicating the linear stage, stopped at the corneal position (P1) and retinal position (P2). Scale bars in (A) and (C) are 200 μm.

5.3.4 Scanning Protocol and Data Visualization

OCT images were acquired, processed, and displayed in real-time by our custom software OCTViewer, which was accelerated with a graphics processing unit (GPU) [49,50,67].

OCTViewer offers two scanning patterns, a high-speed alignment mode and a high-resolution data acquisition mode. The operator could toggle between these two modes as needed. The high-speed alignment mode operated at a 10 Hz volume rate with 400 A-scans per B-scan and 100 B-scans per volume. This scan rate provided real-time feedback, allowing us to locate the area of interest. Compared with the non-contact approach [79], the contact approach significantly reduced the alignment time due to the pre-setting of the scanning pivot point without needing to adjust the working distance. Once the area of interest was found, autofocus was performed within 1 second based on the brightness of the *en face* images using a hill-climbing algorithm [51]. When sufficient image brightness and contrast are achieved and patient motion is at a minimum, the operator could switch to the high-resolution data acquisition mode to save multiple raw OCT volumes for redundancy and quality control. In this mode, the scanning protocol consisted of 800 A-scans per B-scan and 780 B-scans per volume. Each volume acquisition time was 1.56 seconds. The short acquisition time could ensure the successful acquisition of images with minimum motion artifacts.

5.3.5 Axial Length Measurement

Pediatric eye AL growth is essential for monitoring the progression of childhood eye pathologies. The relationship between AL growth in infants and the severity of ROP has previously been discussed [98]. Moreover, AL growth is also a crucial parameter for monitoring myopia progression [99]. To assess AL in the myopia progression and monitor the eye growth of premature infants, accurate quantification of the morphological characterization is critical. Long-range SS-OCT with imaging depth covers from the anterior chamber to the posterior pole has been demonstrated for optical biometry [100]. However, due to the digitizer speed and bandwidth limitations, long-range OCT systems usually have a low A-scan sweeping speed, which is not ideal for handheld panretinal imaging applications. When the imaging depth could only cover part of

the eye, a non-contact OCT imaging approach cannot accurately determine the AL due to the lack of a fixed reference plane. In the contact handheld OCT system, the position of the corneal surface and the scanning pivot point were fixed at each imaging session, which could ensure the repeatability of measurements.

Unlike ultrasound, OCT measures the optical path length (OPL) rather than the acoustic path length to convert the eye's geometry length (GL). When converting GL from OPL, the mean refractive index (similar to the application of mean velocity in ultrasound) has to be applied [100]. The optical parameters of the Gullstrand eye model of newborn infants are listed in Table 5.1 [101,102]. The average refractive index was calculated based on the formula

$$n_{avg} = \frac{1}{d}\sum_{i=1}^{5} n_i \times d_i$$

where n_{avg} is the average refractive index, d is the axial eye length, n_i is a refractive index at different ocular segments, and d_i is the thickness of different ocular segments. The result is $n_{avg} = 1.357$.

The OPL change is the result of the GL change in the eye. Therefore, the average refractive index of the eye n_{avg} is also given by the OPL divided by the GL, which is

$$n_{avg} = \frac{OPL}{GL}$$

The position of the meniscus lens was fixed and pre-recorded [Figure 5.3(A)]. At the beginning of each imaging session, the reference arm position and the focus of the imaging beam were first adjusted on the corneal surface. OCT images and the reference arm position for the corneal surface were recorded. Then the reference arm was rapidly increased to match the retina position, where OCT data and reference arm position, where OCT data of the retina along with the reference arm position were saved as well. After the imaging session, the OPL was determined

according to the positional difference between the corneal apex and fovea along the visual axis [Figure 5.3(B)].

Table 5.1: Optical parameters of Gullstrand eye model of new-born infants

Ocular segment	Spacing (mm)	Refractive index
CT	d1=0.75	1.377
ACD	d2=1.85	1.336
LT	d3=3.7	1.43
VCD	d4=11.0	1.334
RT[a]	d5=0.15	1.346

Note:

a: the parameter of the retina from [102].

CT: Corneal Thickness. ACD: Anterior Chamber Depth. LT: Lens Thickness. VCD: Vitreous Chamber Depth. RT: Retinal Thickness.

5.3.6 Study Subjects

The 140° FOV contact handheld SS-OCT was used to image infants in the operating room and neonatal intensive care unit (NICU). These subjects were recruited from the Casey Eye Institute at Oregon Health & Science University (OHSU) between August 2021 and May 2022. Written informed consent for imaging from the infant's parents or guardians was obtained before initiating the study. The protocol was approved by the Institute Review Board/Ethics Committee of OHSU and adhered to all tenets of the Declaration of Helsinki.

5.4 Results

Sixty-seven infant subjects (Table 5.2) were recruited in this study, and 246 imaging sessions were performed with 99.6% of infants imaged successfully. Imaging was deferred in the

setting of clinical factors that would make imaging too time-consuming and stressful for infants, such as swollen eyelids due to continuous positive airway pressure (CPAP).

Table 5.2: Subjects' diagnostic information

	Infant subjects
Total subjects	67
Diagnosis	ROP (45)
	Retinoblastoma (4)
	Retinal Detachment (5)
	Coats Disease (2)
	Incontinentia Pigmenti (5)
	Lattice Degeneration (1)
	Familial Exudative Vitreoretinopathy (1)
	Persistent Fetal Vasculature (1)
	Retinal Hemangioblastoma (1)

Each imaging session, including an alignment process and image acquisition, was optimized to be completed within 2 minutes to reduce the discomfort of the patients. Before the imaging session, the subject was dilated with cyclopentolate hydrochloride and phenylephrine hydrochloride. Lubricant eye gel (Systane, Alcon, Switzerland) was applied to the cornea to prevent corneal abrasion to facilitate the coupling of the meniscus lens with the cornea. An eyelid speculum was placed to keep the eye open and ensure sufficient contact between the ocular surface and the meniscus lens, which could greatly speed up the imaging procedure. The meniscus lens was sterilized before each imaging session. During the imaging session, the operator gently rested the hand on the forehead of the baby to precisely control the pressure on the eyeball while imaging. When imaging uncooperative patients such as young children and infants with handheld retina

scanners, motion artifacts can be severe and have a significant impact on the image quality. Through the combination of high-speed laser, fast scanning pattern, real-time image feedback as well as contact lens design, we were able to minimize the influence of motion artifacts in our handheld panretinal OCT system.

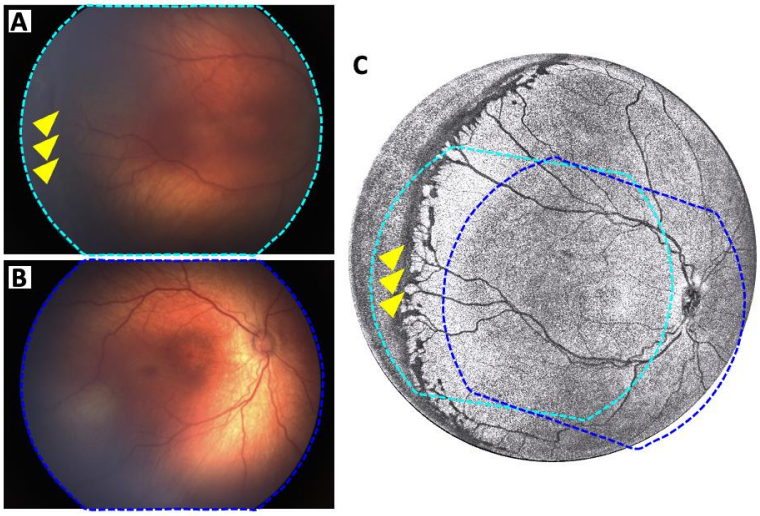

Figure 5.4 (A)-(B) RetCam color fundus images from an infant with ROP stage 3 at different locations. (C) *En face* OCT image from the same infant acquired by contact handheld panretinal SS-OCT imaging system. Yellow arrowheads in (A) and (C) point to the area of extraretinal neovascular proliferation.

ROP stage 3 is associated with significant vascular abnormalities, and delayed diagnosis might lead to blindness [103]. Early detection with an ultra-widefield imaging tool followed by prompt treatment could prevent vision loss. A comparison between RetCam color fundus images and *en face* OCT images from the same premature infant is shown in Figure 5.4. The dashed cyan and blue boxes in Figure 5.4(C) correspond to Figure 5.4(A) and Figure 5.4(B), respectively. The *en face* OCT image covered the retina area extended from the posterior pole to the retinal periphery, which was larger than the single RetCam fundus image, specified to have a 130° FOV. In addition, the image contrast at the area of extraretinal neovascular proliferation (yellow arrowheads) in the *en face* OCT image is much better than that in the RetCam fundus image.

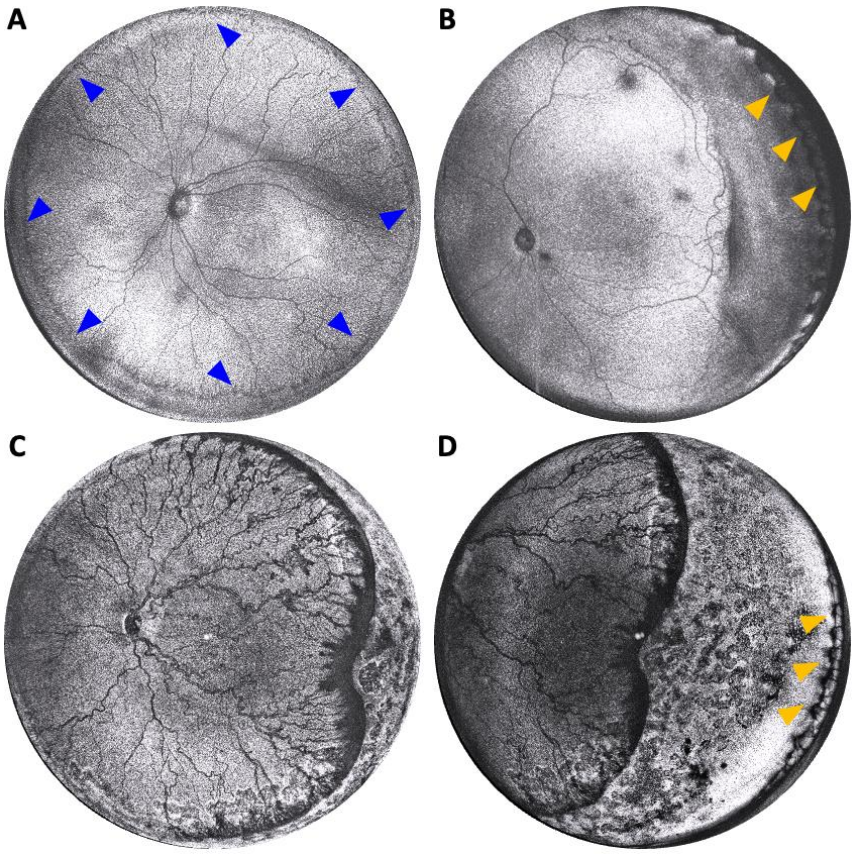

Figure 5.5 (A) *En face* OCT image from an infant with ROP stage 1. Blue arrowheads point to the demarcation line with the retinal vascular-avascular junction. (B) *En face* OCT image from an infant with ROP stage 2. The gray streak visible in the image is a motion artifact that occurred during image acquisition. (C)-(D) *En face* OCT images from the infant with ROP stage 3 at different locations after laser treatment. Yellow arrowheads in (B) and (D) point to the area of ora serrata.

En face OCT images from three infants with ROP at different stages were presented in Figure 5.5. A demarcation line separating the vascular and avascular retina [blue arrowheads in Figure 5.5(A)] was distributed all around zone I. To the best of our knowledge, this was the first time that entire the 360-degree demarcation line was visualized in a single OCT image. Some groups have reported that they could use a montage to take OCT to the peripheral retina. In addition, we were also able to identify the ora serrata on the nasal side by rotating the probe, which

was considered more difficult to observe than on the temporal side, as pointed by the yellow arrowheads in Figure 5.5(B) and Figure 5.5(D). *En face* OCT images in Figure 5.5(C) and Figure 5.5(D) were from the same infant but located in different areas. The utilization of handheld panretinal OCT is beneficial for clinicians in identifying and documenting disorders throughout the retina.

Six subjects with different severities of ROP were selected as representatives to calculate the AL according to the method described in the previous section. The result is listed in Table 5.3. One of the premature infants (Subject 6) was followed for two months to observe and record the development of the eye.

Table 5.3: Axial length of the eye from premature infants

	GA	PMA	Axial length (mm)
Subject 1	23w4d[a]	37w5d	17.17
Subject 2	26w6d	53w2d	18.13
Subject 3	23w	34w6d	17.59
Subject 4	25w2d	35w5d	17.31
Subject 5	24w4d	33w1d	17.12
Subject 6	23w5d	33w3d	17.82
		34w3d	17.93
		35w3d	18.01
		37w5d	18.11
		40w3d	18.37
		41w3d	18.70

Note:

[a]: 23w4d refers to 23 weeks and four days. Others are similar.

GA: Gestational age. PMA: Postmenstrual age.

5.5 Discussion

We have developed a 400 kHz handheld SS-OCT system with an unprecedented 140° FOV using a contact approach and demonstrated its significant value in the diagnosis and management of disease involving the peripheral retina. Our imaging system leverages a state-of-the-art MEMS-VCSEL laser, parallel computing with GPU, and novel optics design to achieve imaging of the entire retina beyond the equator, reaching the ora serrata. The panretinal FOV and high-speed imaging technique have great potential to improve the diagnosis of retinal diseases in adults and infants. This approach is particularly promising for pediatric applications, such as the assessment of ROP, and adult patients under sedation. Because premature infants cannot cooperate with the photographer for the imaging adjustment, the contact approach is conducive to minimizing the eye motion artifacts and eliminating shadow artifacts caused by the patient's eyelashes. The first significant achievement in our prototype is the unprecedented 140° FOV (pivoting angle on the pupil plane), which can capture the posterior pole and far peripheral retina in a single shot. In addition to the optical design, UWF imaging systems are limited by their imaging speed. To satisfy the Nyquist sampling theorem, 1) wider FOV demands more sampling points, and 2) higher optical resolution entails higher sampling density, both of which require higher imaging speed. In practice, even with ultrahigh-speed swept-source lasers, the lateral resolution is intentionally kept low (in the orders of 50 μm, which is not suitable for imaging detailed vasculature networks with OCT angiography). We have carefully considered the design criteria and trade-offs between the FOV, resolution, and image speed in our panretinal OCT system with priority on the FOV and imaging speed while sacrificing the transverse resolution. Our novel optical design enables panoramic view of the retina with adequate transverse resolution to visualize the peripheral retinal disease while maintaining high imaging speed to complete imaging session quickly, which is critical in

minimizing patient discomfort, motion artifacts, and significantly improving success rate and image quality.

The adequate visualization of the periphery has excellent utility in ocular disease surveillance, especially in clinically silent pathologies originating from a peripheral area and are generally not visualized with standard OCT imaging. Some studies regarding disease mechanisms and proof of concept were limited by available imaging technology. For example, early research in ROP utilizing time-domain OCT was often limited to the evaluation of the macula [104]. With the ability to sufficiently visualize the pathologies in the peripheral retina, we have started to conduct more sophisticated analyses to improve understanding regarding the role that peripheral pathology can play in retinal diseases, for instance, the previously unknown relationship between the peripheral fibrovascular ridge thickness and ROP stage classification [77,105]. The effect of therapeutic interventions for the prevention of severe ROP may also be explored. It is also possible to use the contact approach panretinal OCT to image adults for various ocular diseases that involve the peripheral retina, including diabetic retinopathy (DR), neovascular and non-neovascular age-related macular degeneration (AMD), vascular occlusion, and retinal detachment [106–108]. The slight discomfort of the contact approach could be justified especially in the case of retinal detachment, in which identifying the location and the exact cause of the detachment is critical.

In addition to the ability of comprehensive retinal screening, our handheld OCT with contact lens design enables measurement of axial eye length, a critical parameter required for quantitative evaluation of biomarkers on the retina. The contact lens in our OCT probe is a meniscus lens that matches the corneal curvature, a similar concept to the immersion method used in ocular ultrasound. By using lubricant eye gel that couples the cornea and the contact lens, and applying very light pressure, we do not expect significant compression exerted by the contact

imaging probe. However, curvature mismatches and differences in eye sizes may impact image quality for various reasons. Unfortunately, we do not have other meniscus lenses with different specifications to test now. Therefore, future studies are needed to validate the measurement results.

Our novel imaging technology holds tremendous promise in the detection and treatment assessment of ocular diseases, despite some limitations. One of the limitations is the need for a trained and skilled operator who can stably place the contact surface on the cornea to acquire images. Although the scanning pivot point is set up in advance to allow all the incident beams to pass through the pupil plane and avoid the vignetting artifacts, long imaging depth is still required to prevent aliasing especially when imaging adults. The fast spectrum sweeping speed and the long imaging range required for our application have pushed the digitizer's performance to the limit. Alternative OCT imaging technology such as circular ranging OCT might be needed to achieve shorter imaging time and longer imaging depth [109]. The optical performance in most of the scanning angles in the current system is already within or close to the diffraction limit. A larger beam size on the pupil will provide a better transverse resolution that will theoretically be suitable for OCT angiography application, which requires a larger aperture galvanometer scanner and a new optical design. However, a larger aperture galvanometer scanner has limited scanning speed, and an alternative scanning pattern might be required [110,111]. Moreover, the increase in numerical aperture may result in lower transverse resolution unless the optical design is optimized across all the scanning angles. Finally, a more accurate model eye with various axial eye lengths, as well as transverse resolution and FOV markers, would be very helpful in fully validating the system performance and calibrating the volumetric measurement.

5.6 Conclusion

We demonstrated a contact handheld SS-OCT system with an unprecedented single shot of 140° FOV, extending the imaging area to the peripheral termination of the retina at the ora serrata. The detailed morphologies of the peripheral retina acquired by our novel imaging technology are valuable in many clinical applications, such as ROP, retinoblastoma, Coats disease, retinal detachment, *etc.* Alongside visualizing the pathologies in the peripheral retina, the handheld panretinal SS-OCT with contact approach may also be used to measure axial eye length, allowing for the quantitative assessment of disease progression and regression after treatment. Diseases such as retinoblastoma can be measured by tumor size.

As such, the visualization of the retinal periphery is increasingly used to diagnose pediatric ophthalmic diseases. The expanded FOV is conducive to identifying clinically inapparent pathologies in the peripheral retina. Clinicians particularly benefit from the peripheral OCT when assessing and diagnosing pathologies starting from the peripheral retina. Therefore, the introduction of the novel OCT imaging technology might herald an era in which the details in the peripheral retina will be depicted sufficiently and efficiently, opening a new window for understanding disease mechanisms.

CHAPTER 6. PANRETINAL OCT ANGIOGRAPHY FOR PEDIATRIC RETINAL IMAGING

6.1 Abstract

Comprehensive visualization of retina morphology is essential in the diagnosis and management of retinal diseases in pediatric populations. Conventional imaging techniques often face challenges in effectively capturing the peripheral retina, primarily due to the limitations in current optical designs, which lack the necessary field of view to characterize the far periphery. To address this gap, our study introduces a novel ultra-widefield optical coherence tomography angiography (OCTA) system. This system, specifically tailored for pediatric applications, incorporates an ultrahigh-speed 800 kHz swept-source laser. The system's innovative design achieves a 140° field of view while maintaining excellent optical performance. Over the last 15 months, we have conducted 379 eye examinations on 96 babies using this system. It demonstrates marked efficacy in the diagnosis of retinopathy of prematurity, providing detailed and comprehensive peripheral retinal angiography. The capabilities of the ultra-widefield handheld OCTA system in enhancing the clarity and thoroughness of retina vascularization assessments have significantly improved the precision of diagnoses and the customization of treatment strategies. Our findings underscore the system's potential to advance pediatric ophthalmology and broaden the scope of retinal imaging.

This work has been published in Biomedical Optics Express.

Shuibin Ni, Guangru Ben Liang, Ringo Ng, Susan Ostmo, Yali Jia, Michael F. Chiang, David Huang, Alison H. Skalet, Benjamin K. Young, J. Peter Campbell, and Yifan Jian, "Panretinal handheld OCT angiography for pediatric retinal imaging," Biomed. Opt. Express 15(5), 3412–3424 (2024).

6.2 Introduction

Optical coherence tomography (OCT) is a non-invasive imaging modality that provides high-resolution, cross-sectional images of the retina [5,74]. OCT angiography (OCTA), a recent advancement within the OCT field, allows for the visualization of retinal blood flow without the need for dye injection [18]. This is achieved by comparing sequential OCT cross-sectional scans acquired at the same position to detect changes in the optical signal, thereby distinguishing between the motion of blood cells and the static surrounding tissue. These technologies, especially with the integration of OCTA, have instigated a significant shift in ophthalmology, enhancing diagnostic capabilities by offering detailed structural and functional information about the retina [17]. Ultra-widefield imaging in OCT/OCTA has become an invaluable tool in managing complex ocular conditions in pediatric patients [12,76,78]. Traditional OCT/OCTA systems, primarily desktop models, however, have limitations in pediatric retinal examinations due to difficulties in imaging non-cooperative infants [73,75]. In response to these challenges, there have been explorations into handheld OCT prototypes for pediatric patient imaging [10–12,14–16,112]. Yet, these prototypes typically face limitations in extending the imaging area to the retinal periphery, a constraint largely attributed to the size and weight limitations of portable probe design, which in turn diminishes their clinical utility. Furthermore, the restricted imaging speed of these systems presents a barrier to the practical implementation of OCTA.

Retinopathy of prematurity (ROP) is a leading cause of childhood blindness worldwide [113]. This vasoproliferative disorder is characterized by progressive fibrovascular changes in both the posterior pole and the retinal periphery [12,71,114]. Identifying and classifying changes in the retinal vasculature are crucial for early and accurate diagnosis, serving as key indicators for treatment strategies [77]. Timely and precise diagnosis can make ROP treatment highly effective,

significantly reducing the risk of blindness associated with the condition [115–118]. The current standard for ROP management includes regular (weekly or bi-weekly) dilated binocular indirect ophthalmoscopy examinations with scleral depression and/or widefield digital fundus imaging (WDFI). However, ophthalmoscopic examinations can be subjective, with scleral depression specifically causing significant neonatal stress, and WDFI may have variable image quality and contrast for definitive ROP diagnosis. Handheld OCT may offer a more objective alternative for ROP detection. Additionally, ROP examinations pose medical risks for fragile neonates, including increased cardiopulmonary complications [119]. Therefore, methods that reduce examination duration and frequency could substantially benefit this patient group.

To overcome these obstacles, we introduced an innovative panretinal ultrahigh-speed handheld swept-source OCTA system, tailored for pediatric use. This system is engineered to facilitate faster, more thorough, and less stressful examinations, specifically benefiting pediatric patients. Equipped with an 800 kHz swept-source laser, the system utilizes a contact-based approach that effectively reduces alignment time and enhances image quality. A notable feature of this system is its ability to achieve a 140° field of view (FOV, visual angle measured from the pupil plane) while preserving superior optical performance. This attribute facilitates precise, panoramic visualization of the retina, which is integral for detailed structural examination and the accurate detection of neovascularization, thereby enriching the scope and efficacy of retinal assessments.

6.3 Methods

6.3.1 System Setup

The schematic diagram of the proposed panretinal ultrahigh-speed handheld OCTA system is shown in Figure 6.1. All new features of the system, compared to our previously developed

system [59,69,70], are highlighted with colored boxes in this figure. Building upon these earlier systems, we have refined the optical design of the probe, achieving a 140° FOV with superior optical performance. The system incorporates a swept-source laser, operating at an 800 kHz A-scan rate and a central wavelength of 1060 nm. The employed vertical-cavity surface-emitting laser (VCSEL) (Thorlabs Inc., USA) has a 70 nm (6 dB) tuning range, yielding an axial resolution of 7.06 µm in air. Notably, the laser operates with a bidirectional sweep at 100% duty cycle, providing an average output power of approximately 40 mW. The high output power of the VCSEL laser was pivotal in optimizing the fiber-based interferometer. This optimization ensured the delivery of a sufficient yet safe amount of imaging beam power to the patient's eye while maximizing collection efficiency. The system retains the 4-coupler interferometer configuration (the gray dashed box in Figure 6.1), comprising two 25/75 fiber couplers [FC1/FC4 (TW1064R3A2A, Thorlabs Inc., USA) in Figure 6.1] and two 50/50 fiber couplers [FC2/FC3 (TW1064R5A2A, Thorlabs Inc., USA) in Figure 6.1]. This arrangement allows for 25% of the power from FC4 to be delivered to the probe, which then collects 75% of the signal reflected from the sample. The handheld probe's output power is maintained at 4.75 mW, adhering to safety standards without posing any light hazard, as per the ANSI Z80.36-2021 [52].

Polarization state variation in the optical fiber patch cord within the sample arm during the alignment can impact the OCT signal-to-noise ratio due to polarization mismatch between the sample and reference arms. To address this, a two-paddle manual fiber polarization controller with a loop diameter of 18 mm (FPC020, Thorlabs Inc., USA), denoted as PC1 in Figure 6.1, was installed in the sample arm's path. Additionally, a two-paddle motorized fiber polarization controller (MPC220, Thorlabs Inc., USA), referred to as PC2 in Figure 6.1, was installed along the reference arm's path (the pink dashed box in the lower left corner of Figure 6.1). Automated

polarization state matching, based on the target *en face* image brightness, is performed before imaging sessions [69]. Additionally, a linear stage [LS (X-LHM100A-E03, Zaber Technologies Inc., Canada) in Figure 6.1], featuring a 100 mm travel range, is integrated to adjust the optical delay for imaging neonates with varying eye axial length.

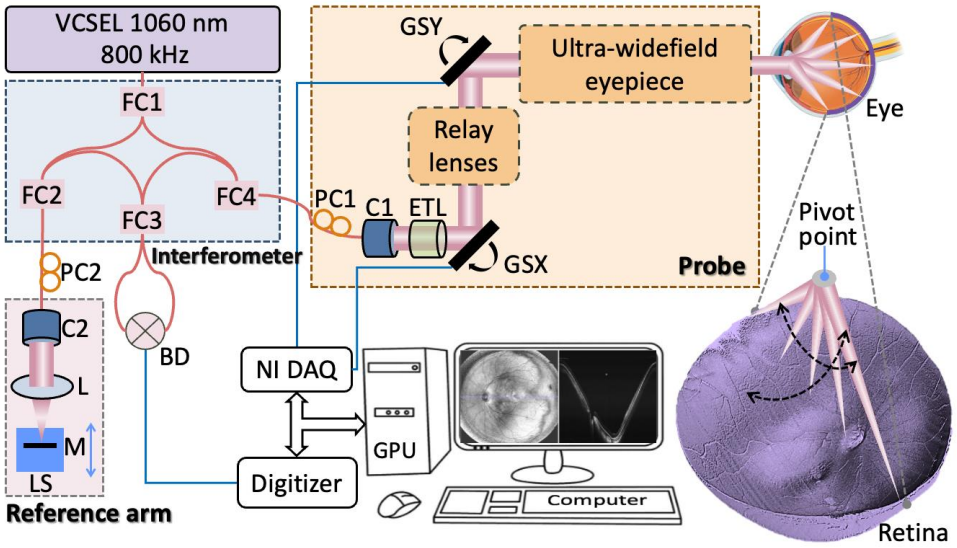

Figure 6.1 Illustrative diagram of the proposed panretinal ultrahigh-speed handheld OCTA system. The orange dashed box at the top center illustrates the elements integrated into the portable probe. The pink dashed box in the lower left indicates the reference arm. The lens group between the GSX and GSY is an ultra-compact telecentric relay lens system. The lens group between the GSY and the eye is the ultra-widefield eyepiece composed of off-the-shelf lenses. The right bottom corner represents the scanning beam on the 3D volume rendering retina. Key components include C1/C2: collimators; L: lens; ETL: electrically tunable lens; GSX/GSY: the fast/slow axes of the galvanometer scanners; M: mirror; PC1-PC2: polarization controller; FC1-FC4: fiber couplers; BD: balanced detector; LS: linear stage; VCSEL: vertical-cavity surface-emitting laser; GPU: graphics processing unit. Red lines illustrate fiber optics. Grey lines represent the electrical cables transmitting digital signals.

6.3.2 Portable Probe Optical Setup

The optical design of the portable probe was developed and optimized using Zemax OpticStudio software (Ansys Inc., USA). The design with ray tracing [as depicted in Figure 6.2(A)

and Figure 6.2(B)] encompasses an ultra-compact telecentric relay lens system and an ultra-widefield eyepiece. The relay lens group, positioned between the fast galvanometer scanner (GSX) and the slow galvanometer scanner (GSY) (Saturn 1B, Pangolin Laser Systems Inc., USA), ensures collimated light transmission with minimal beam deviation across both scanner planes. The ultra-widefield eyepiece, integral for attaining an extended FOV, is composed of a series of selected off-the-shelf lenses.

The block diagram of the custom-designed telecentric relay lens system is illustrated in Figure 6.2(E). The lens details in the relay lens system are listed in Table 6.1. The telecentric relay lens system is critical for correcting optical misalignment during 2-dimensional scanning. Typically, the two orthogonal scanners are placed 5-10 mm to each other. Because of this separation distance, the imaging beam position on the pupil plane when scanned at different angles cannot be overlapped. By separating the two scanners with a relay lens system, the two scanners are optically conjugated [42,69,80]. However, it is observed that the traditional relay lens design, using off-the-shelf optics, has not reached an optimal level of performance. The comparative results of the beam wandering on the GSY plane are shown in Figure 6.2(D). The result reveals that in the traditional design, there is a notable 7.25% offset in the beam wandering on the GSY plane during scanning. In contrast, the custom-designed telecentric relay lens system demonstrates a significantly reduced offset of only 1.07%, indicating a marked improvement in alignment. The custom-design telecentric relay lens system incorporates two identical doublet lenses [L1/L2 and L7/L8 as shown in Figure 6.2(E)] and two pairs of matching singlet lenses [L3/L6 and L4/L5 in Figure 6.2(E)]. The doublet lenses consist of a negative meniscus lens paired with a biconvex lens. The custom-designed telecentric relay lens system with ultra-compact dimensions [20 mm in diameter and 76 mm in length as shown in Figure 6.2(F)], was manufactured by Avantier Inc.,

USA. These lenses create an optical conjugation between the GSX and the GSY. The configuration ensures the footprints on both GSX and GSY are perfectly aligned, thereby partly addressing the iris vignetting artifact.

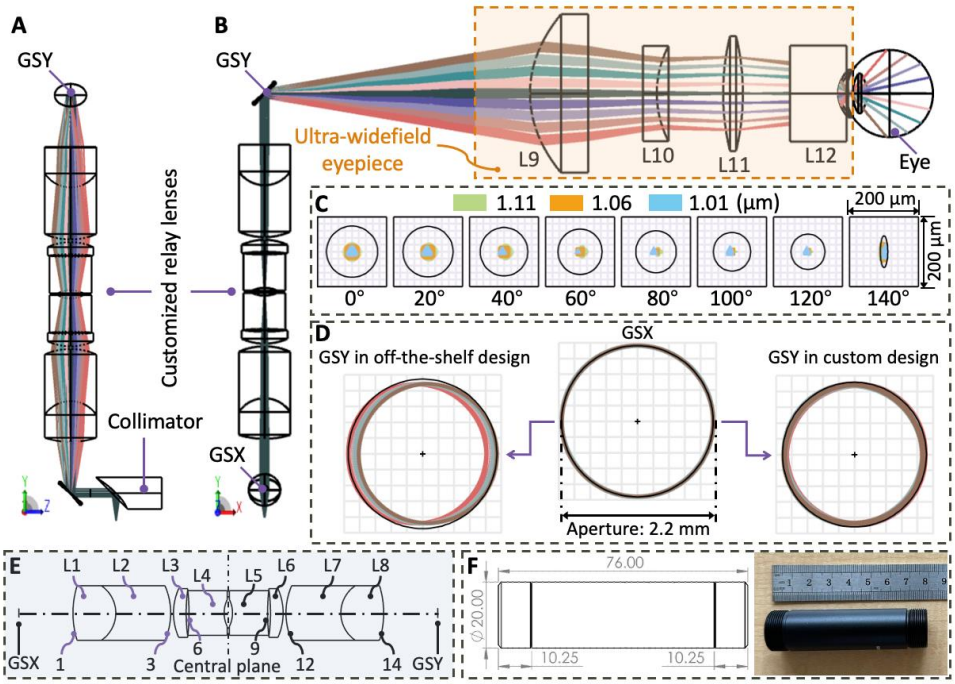

Figure 6.2 Detailed optical design of the portable probe. (A) The side view showcases the 3D configuration of the telecentric relay lens system in OpticStudio. (B) The front view displays the 3D arrangement of the whole sample arm in OpticStudio. L9-L11: off-the-shelf lenses from Edmund Optics Inc.; L12: Quad Pediatric lens from VOLK Optical Inc. (C) Optical performance on the retinal plane of a simulated eye model covering from a field of view ranging from 0° to 140° at 20° intervals. The black circles represent the Airy disk, with a central Airy radius of 73.6 μm. Notably, as the scanning angle extends towards the periphery, the incident beam's shape transitions from circular to elliptical form on the pupil plane, causing variations in the Airy disk size with increasing scanning beam angles. Scale markers are set at 200 μm. Color coding for the wavelength: green: 1100 nm; orange: 1060 nm; cyan: 1010 nm. (D) Comparison of scanning beam footprint diagrams on the GSY, contrasting beams relayed by the traditional design using off-the-shelf lenses [69,80] with those of the proposed custom design. (E) The block diagram of the telecentric relay lens system. The lens details are listed in Table 6.1. (F) On the left: the mechanical

configuration of the relay lenses. On the right: a photograph of the actual relay lenses produced. All dimensions are provided in millimeters.

The ultra-widefield eyepiece lens system, located between the GSY and eye, features a compact, lightweight design, ensuring an appropriate working distance to align with the pupil plane when the contact surface is placed on the cornea. The ultra-widefield eyepiece includes an aspheric lens [L9 in Figure 6.2(B)] with a 40 mm focal length (17-008, Edmund Optics Inc., USA), a plano-concave lens [L10 in Figure 6.2(B)] with a -50 mm focal length (68-001, Edmund Optics Inc., USA), and a double-convex lens [L11 in Figure 6.2(B)] with a 60 mm focal length (67-661, Edmund Optics Inc., USA). Additionally, a specialized contact lens (Quad Pediatric, VOLK Optical Inc., USA) was incorporated. The Quad Pediatric lens [L12 in Figure 6.2(B)] combines an advanced double aspheric lens and a meniscus lens, further enhanced with a custom anti-reflection coating. The coating, tailored to reduce reflectivity below 0.5% within the 950 nm to 1150 nm wavelength range, significantly improves sample light collection efficiency [79,80]. Figure 6.2(C) depicts a set of point spread functions (PSFs) corresponding to the ray traces from Figure 6.2(A) and Figure 6.2(B), representing a FOV ranging from 0° to 140° at 20° intervals. These PSF plots demonstrate diffraction-limited performance across the entire FOV at all wavelength ranges. However, the complex double aspherical ocular lens in L12 introduces some irregularities in the beam profile on the retina as the scanning angle extends towards the periphery. This effect can influence the size and shape of the PSF, and consequently, the size of the Airy disk in the spot diagram varies with the increasing FOV. Upon demagnification by the ultra-widefield eyepiece, the beam size on the pupil plane was measured at 0.35 mm. This results in a theoretical spot size of 46.4 μm (measured as the $1/e^2$ diameter) on the retinal plane, specifically when imaging an infant with an axial eye length of 17 mm.

Table 6.1: Lens data of the ultra-compact telecentric relay lens system (unit: mm)

Surface	Radius	Thickness	Material (Lens)
1	21.843	10.226	H-LAK7A (L1)
2	-7.812	13.108	H-ZF73GT (L2)
3	-16.059	0.676	
4	14.188	3.023	H-ZLAF92 (L3)
5	42.219	0.676	
6	-54.979	8.391	H-ZF39 (L4)
7	7.229	2	
8	-7.229	8.391	H-ZF39 (L5)
9	54.979	0.676	
10	-42.219	3.023	H-ZLAF92 (L6)
11	-14.188	0.676	
12	16.059	13.108	H-ZF73GT (L7)
13	7.812	10.226	H-LAK7A (L8)
14	-21.843	12.900	

6.3.3 Portable Probe Mechanical Setup and System Assembly

The simulation results from the optimized Zemax analysis were transferred into CAD software (SolidWorks, Dassault Systèmes, France) to develop the mechanical design. This integration facilitated the precision alignment of the lens system, achieved using custom-design lens tubes [illustrated as gray components within the orange dashed box in Figure 6.3(A)]. Additionally, a 5.5-inch AMOLED display with two separate imaging windows [Figure 6.3(B)-Figure 6.3(D)], facilitates the alignment process. Figure 6.3(E) illustrates the spatial arrangement of the essential components inside the probe. For robust protection and organization, the optical fiber, and various electrical cables, including galvo cable sets, electrically tunable lens driver cable,

HDMI cable for the display, and Micro-USB cable for display power, were bundled within a nylon protective sleeve sheath. The portable probe itself, excluding the fiber and electrical cables, weighs approximately 550 grams.

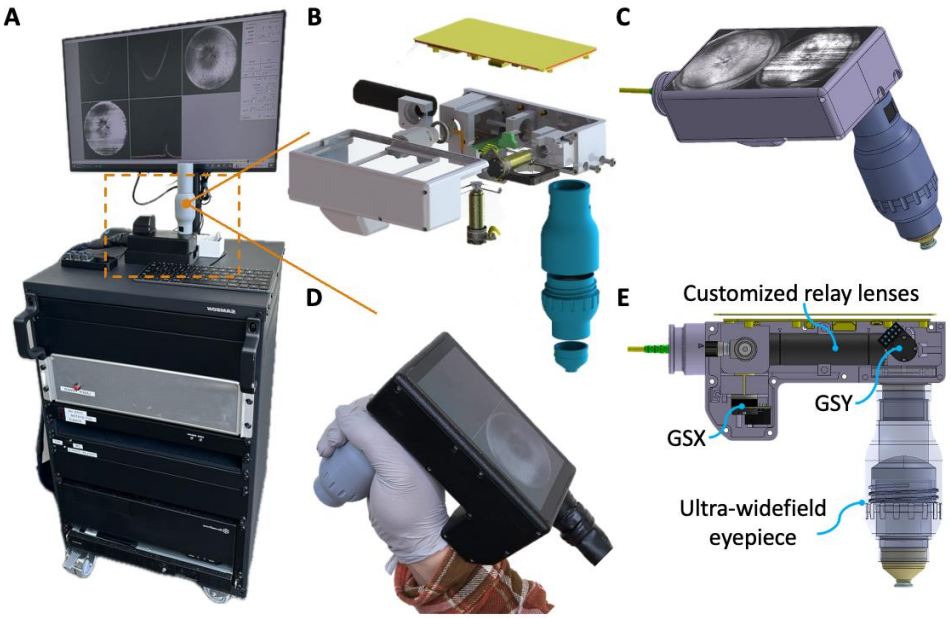

Figure 6.3 Integrated system and portable probe assembly. (A) Photograph showcasing the assembly panretinal handheld OCTA system. (B) Exploded view detailing the mechanical design of the probe. (C) 3D mechanical designs of the fully assembled portable probe. (D) Photographic depiction of the fully assembled portable probe. (E) Front view of the 3D mechanical design, showing key internal components of the probe.

The OCT engine of the imaging system was encased in a 19-inch rack enclosure, spanning 3 rack units (U) in height (EC3U, Thorlabs Inc., USA), while the electrical components were housed in a separate 2U 19-inch rack enclosure. These enclosures were then integrated into a portable OCT imaging cart, with the complete assembly presented in Figure 6.3(A). To enhance operational efficiency, a secondary keyboard, programmed with six shortcut keys for functions such as data saving, scanning mode toggling, auto-focus, auto-polarization control, and reference arm length adjustment, was connected to the system. This design choice streamlined the operation

process, reducing reliance on traditional mouse-based controls and thereby increasing operation efficiency.

6.3.4 Scanning Protocol and Data Visualization

In this project, we implemented three separate scanning protocols to meet imaging requirements. The first was a high-speed alignment mode operating at a volume rate of 10 Hz, designed for rapid identification and alignment of the target area. For high-resolution data acquisition, we employed two modes: an OCT mode for retinal structure imaging and an OCTA mode for angiographic volume capture. In the OCT mode, the protocol involved 800 A-scans per B-scan and 800 B-scans per volume, enabling a rapid volume acquisition in just 0.8 seconds. In contrast, the OCTA mode's protocol incorporated three repeated B-scans at each location, with 800 A-scans per B-scan, resulting in a total of 2400 B-scans per volume acquired in 2.4 seconds.

Both OCT and OCTA images were captured and processed using our custom-developed software, OCTViewer. This software was GPU-accelerated, facilitating real-time quality feedback and alignment processes [49–51]. Peripheral hardware controls, such as a motorized polarization controller, electrically tunable lens, and motorized reference arm, were integrated into the software package. The increased imaging speed for ultra-widefield OCTA necessitates a high-speed digitizer and generates substantial data volumes. In our 800 kHz OCTA system, each OCTA volume generates approximately 16 GB of unprocessed raw data.

For structural OCT images, numerical dispersion compensation was employed to address the dispersion mismatch between the reference and sample arms. A Hanning window was applied to the raw spectral data before Fourier Transformation, which reduces the sidelobes and improves the contrast of the structural OCT images. Additionally, a de-sinusoidal interpolation algorithm was utilized for each B-scan before generating the *en face* OCT image, which was then produced

using maximum intensity projection. OCTA B-scans were generated using the split-spectrum amplitude-decorrelation algorithm [24]. The algorithm was applied to three repeated B-scans instead of two at each specific retinal location to enhance the accuracy and reliability of the acquired data. The generation of *en face* OCTA images commenced with maximum intensity projection of auto-segmented inner retinal layers, which may be adjusted by manual correction to improve segmentation accuracy in some cases. For further processing of the *en face* OCTA images, a Gabor filter was applied to each image to enhance the OCTA signal by emphasizing key image features while reducing background noise [47,48]. In the final processing step, a customized color map was utilized for each *en face* image to improve visual interpretability [45].

6.3.5 Study Subjects

The panretinal handheld OCTA system was employed for imaging infants in both the operating room and the neonatal intensive care unit (NICU). Pediatric patients for this study were enrolled at the Casey Eye Institute at the Oregon Health & Science University (OHSU) from September 2022 to January 2024. The research was conducted under a single approval of the OHSU Institutional Review Board/Ethics Committee, which was sufficient for all aspects of the study. This approval was in strict compliance with the ethical guidelines outlined in the Declaration of Helsinki. Before initiating any study-related procedures, written informed consent was obtained from the parents or legal guardians of each infant participant, confirming their consent for their child's involvement in this imaging study. As per routine ROP examination, before each imaging session, infants were administered cyclopentolate hydrochloride and phenylephrine hydrochloride in both eyes. Then a standard pediatric speculum was placed [illustrated by green arrows in Figure 6.4(A)], and lubricant eye gel (Systane, Alcon, Switzerland) was instilled onto the corneal surface, to prevent corneal abrasion and ensure coupling between the lens meniscus and cornea. During the

imaging, the operator precisely controlled the pressure exerted on the eyeball by gently resting a hand on the infant's forehead.

6.4 Results

Over 15 months, we have conducted 379 eye examinations on 96 babies utilizing the imaging system. 99.5% of these imaging sessions yielded high-quality data suitable for reliable analysis. Each imaging session was streamlined to conclude within 2 minutes, which was crucial to minimize the discomfort of the patients and mitigate medical risks. Representative *en face* OCT images obtained during these pediatric examinations are illustrated in Figure 6.4. The system's high-speed alignment mode, equipped with real-time visualization, functions comparable to a fundus camera. Its deep depth of focus is instrumental in accurately locating the target area. For instance, Figure 6.4(A) displays an *en face* OCT image captured from the orbital area of an infant before the placement of the probe on the cornea. The OCT mode, with its rapid visualization capabilities (0.8 seconds), effectively minimizes the appearance of motion artifacts, as depicted in Figure 6.4(B) and Figure 6.4(C). By adjusting the probe incident angle appropriately, we successfully visualized the ciliary body and ora serrata, which were considered the peripheral limits of the retina. Notably, these images were acquired without the necessity for scleral depression.

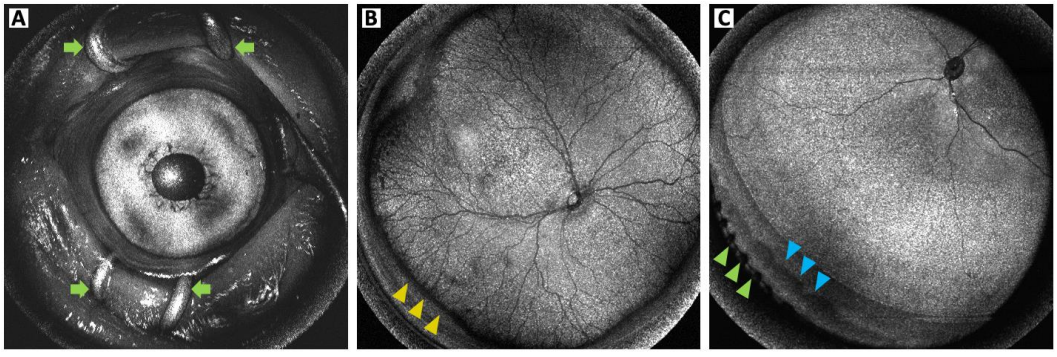

Figure 6.4 Representative *en face* OCT images from ROP examinations. (A) *En face* OCT image displaying the orbital region of an infant during the alignment process, with green arrows indicating the eye speculum used to keep the eyelids open and expose the ocular surface. (B) *En face* OCT image from an infant (born at 24 weeks gestation, 568 grams, and imaged at 35 weeks postmenstrual age) diagnosed with ROP zone II, stage 2, showing extraretinal neovascular proliferation at the retinal vascular-avascular junction (marked by yellow arrowheads). This proliferation was almost entirely captured around the retinal periphery into zone II in a single, non-montage image. (C) *En face* OCT image from an infant (born at 29 weeks gestation, 1344 grams, and imaged at 39 weeks postmenstrual age), showcasing the ability to capture the ora serrata (indicated by cyan arrowheads) and the ciliary body (highlighted by green arrowheads), without scleral depression.

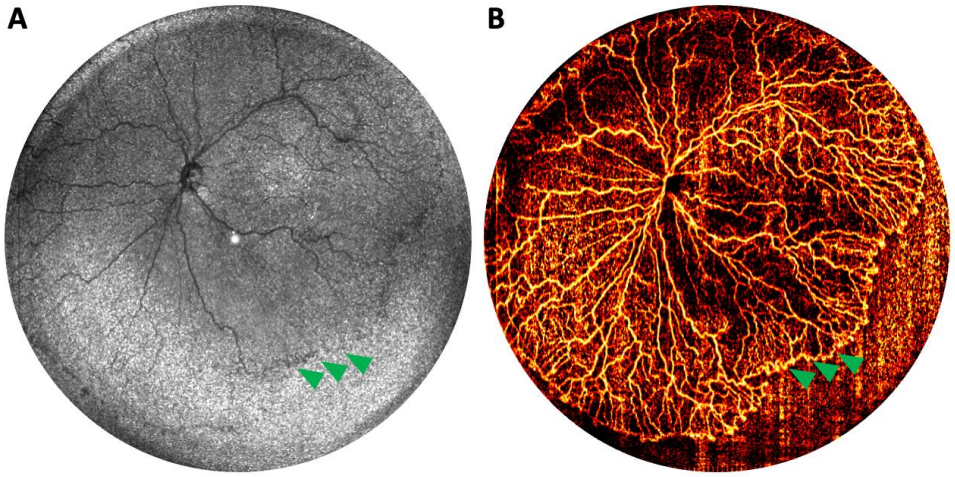

Figure 6.5 (A) *En face* OCT image of the right eye from an infant (born at 23 weeks gestation, 593 grams, and imaged at 38 weeks postmenstrual age) with ROP stage 1, where the fibrovascular ridge is marked by green arrowheads but is not distinctly visible in the structural *en face* image. (B) The corresponding *en face* OCTA heatmap enhances the visualization of the vascularized retina, providing greater clarity and detail.

Incorporating OCTA into our imaging system has significantly advanced our capability to delineate the vascular-avascular boundary in ROP. The feature proves particularly beneficial in scenarios where the fibrovascular ridge is not readily apparent during clinical evaluations or via

structural *en face* OCT imaging. The *en face* OCTA image showcases the junction with greater clarity and definition compared to the *en face* OCT structural image, as indicated by green arrowheads in Figure 6.5(A) and Figure 6.5(B). Delineation is imperative for determining the extent of retina vascularization, a task that is challenging with ophthalmoscopy in the absence of disease.

Neovascularization plays a pivotal role in the progression of ROP. During the ROP stage 2, as depicted in Figure 6.6(A), there is a proliferation of abnormal blood vessels at the junction of the vascular and avascular regions of the retina. The *en face* OCTA can effectively illustrate the neovascularization by projecting flow signals located within the vitreous, particularly from the slab positioned above the inner limiting membrane. As demonstrated in Figure 6.6(B), neovascularization in ROP extends beyond the ridge area. Previously, visualizing and quantifying these vascular changes posed significant challenges. However, advancements in imaging techniques may now enhance our understanding of the phenotypic patterns of ROP progression and its underlying physiological processes [120].

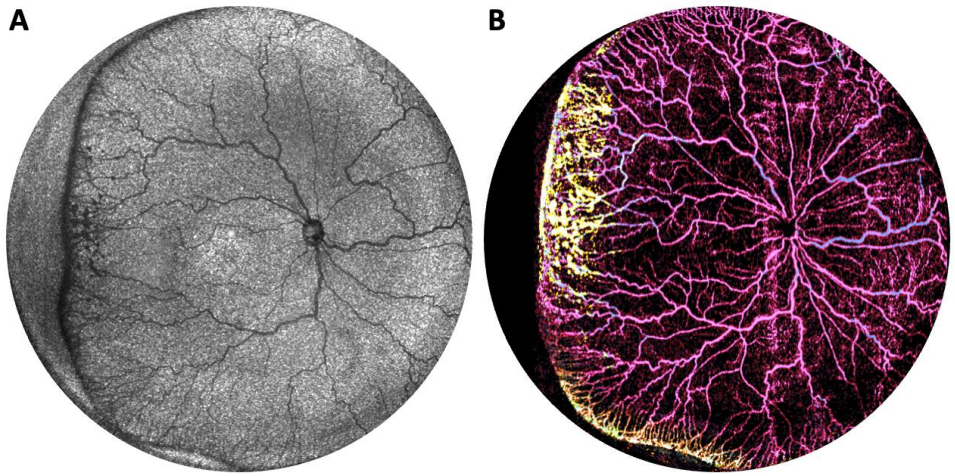

Figure 6.6 (A) *En face* OCT image of the left eye from the same infant as in Figure 6.5, presenting with ROP stage 2. (B) The corresponding *en face* OCTA heatmap illustrates the area of neovascularization with enhanced detail. Neovascular zones are highlighted by the presence of yellow vessels, indicating abnormal vessel growth into the vitreous region.

6.5 Discussion

The imaging of the peripheral retina poses a considerable challenge, especially in pediatric populations. Existing retinal imaging devices are primarily designed for adults, require high levels of patient cooperation, and are not ideally configured for pediatric use. Handheld WDFI systems have gained popularity in managing pediatric retinal diseases owing to their portability, but often compromise on image contrast and resolution. Standard OCT retinal imaging systems typically do not offer an imaging FOV exceeding 100°, limited by optical design, imaging speed limitations, and axial range. There is a critical demand for a dedicated, portable, handheld OCT retina scanner for pediatric applications. Several research groups, including ours, have been pioneering the development of faster OCT prototypes optimized for neonatal use. We are the only group to have successfully achieved ultra-widefield OCT imaging in non-sedated babies [69,79,121]. Our previously reported panretinal OCT imaging system, notable for its extensive FOV in a single capture, has proven effective in diagnosing various pediatric retinal diseases. It has facilitated sophisticated analyses of peripheral pathologies, uncovering previously unknown relationships, such as the correlation between peripheral fibrovascular ridge thickness and ROP stage classification [77,105].

Our earlier systems encountered challenges such as limited imaging speed and suboptimal optical design, which impeded the integration of OCTA mode in ultrawide imaging [79,80,122]. In this study, however, we have addressed these limitations by developing a faster OCT engine with improved optical performance. This has enabled the first successful implementation of ultra-widefield OCTA in premature infants. Compared to WFDI, our novel system offers a significantly larger FOV and enhanced image contrast, effectively highlighting peripheral pathologies. Our

results demonstrate that the panretinal ultrahigh-speed handheld OCTA system could help understand vascular growth dynamics in ROP.

Despite these advancements, our handheld OCTA system faces limitations. The contact imaging method necessitates skilled ophthalmic technicians for image acquisition, though this is similar to current WDFI systems. Although the scanning pivot point is pre-set to minimize vignetting artifacts, the lens design with a predetermined curvature and working distance cannot accommodate the rapid growth of the eyes in premature infants. Additionally, a long axial imaging range is essential to avoid aliasing, due to the time constraints in imaging uncooperative infants, we sometimes cannot precisely adjust the reference arm to match the axial eye length. Furthermore, the optical performance at most scanning angles is near or at the diffraction limit at the focal spot with a central radius of 73.6 μm. Increasing the beam size on the pupil in theory would improve transverse resolution for OCTA. However, this requires the integration of a larger aperture galvanometer scanner along with improvement in the optical design. A key consideration is that larger aperture galvanometer scanners have limited scanning speed, and an alternative scanning pattern might be required [110,111]. Moreover, an increase in numerical aperture could inadvertently compromise transverse resolution unless the optical design is thoroughly optimized. We conducted an optical simulation with a beam size triple that of the proposed system. This adjustment resulted in an improved central radius of the Airy disk, decreasing from 73.6 μm to 24.5 μm. However, the simulated spot diagram demonstrated a deterioration, as depicted in Figure 6.7. An enhanced optical design aimed at minimizing optical aberrations at larger scanning angles is imperative; meanwhile it should not result in a significantly heavier or bulkier system. Finally, retinal layer segmentation algorithms are not yet optimized for current ultra-widefield OCTA images [123,124]. Future work should focus on optimizing these algorithms. Addressing these

limitations and enhancing the current system's capabilities will further improve the utilities of ultra-widefield handheld OCTA in pediatric retinal imaging.

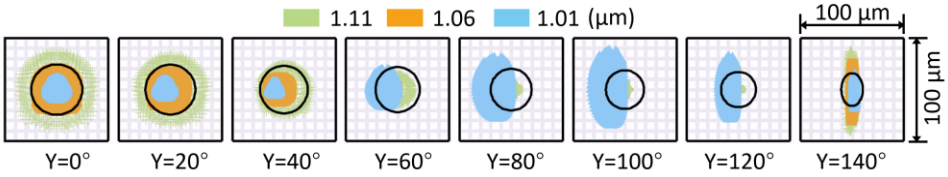

Figure 6.7 Optical performance evaluation with a beam size tripled compared to the proposed system) on the retinal plane covering from a field of view ranging from 0° to 140° at 20° intervals, utilizing the same settings in OpticStudio as in Figure 6.2. Scale markers are 100 μm. Wavelengths are color-coded as follows: green for 1100 nm, orange for 1060 nm, and cyan for 1010 nm.

6.6 Conclusion

We have successfully developed a panretinal ultrahigh-speed handheld swept-source OCTA system, specifically designed for pediatric retinal imaging. The advanced system incorporates an 800 kHz VCSEL laser source and can deliver an extensive 140° FOV. Its exceptional imaging proficiency, especially in capturing detailed peripheral retinal angiography, has demonstrated significant clinical value in the diagnosis of ROP. The system's broadened FOV enables clinicians to identify and evaluate various retinal pathologies, which might otherwise remain undetected in the periphery. Advanced technology provides essential insights for the accurate assessment and diagnosis of a range of ocular conditions affecting this critical eye region. Its application in pediatric ophthalmology is particularly beneficial, as early detection of retinal disorders can significantly influence the course of treatment and overall prognosis.

CHAPTER 7. APPLICATIONS

7.1 Retinopathy of Prematurity

Retinopathy of prematurity (ROP) is a complex eye disorder mainly affecting premature infants, with a significant risk of blindness. It occurs when the normal development of retinal blood vessels is disrupted, leading to abnormal, fragile vessels. These vessels can bleed, causing scarring and retinal detachment, severely impairing vision. The retina captures light and sends visual information to the brain, so retinal detachment can result in profound vision loss or blindness. Each year, 1-2 million infants are at risk for ROP, and 20,000-50,000 infants suffer preventable blindness due to missed, delayed, or incorrect diagnoses [125,126].

This chapter has been partially published in the following journals.

Shuibin Ni, Xiang Wei, Ringo Ng, Susan Ostmo, Michael F. Chiang, David Huang, Yali Jia, J. Peter Campbell, and Yifan Jian, "High-speed and widefield handheld swept-source OCT angiography with a VCSEL light source," Biomed. Opt. Express 12(6), 3553–3570 (2021).

Thanh-Tin P. Nguyen, **Shuibin Ni**, Shanjida Khan, Xiang Wei, Susan Ostmo, Michael F. Chiang, Yali Jia, David Huang, Yifan Jian, and J. Peter Campbell, "Advantages of Widefield Optical Coherence Tomography in the Diagnosis of Retinopathy of Prematurity," Front. Pediatr. 9, 797684 (2021).

Thanh-Tin P. Nguyen, **Shuibin Ni**, Susan Ostmo, Archeta Rajagopalan, Aaron S. Coyner, Mani Woodward, Michael F. Chiang, Yali Jia, David Huang, J. Peter Campbell, and Yifan Jian, "Association of Optical Coherence Tomography–Measured Fibrovascular Ridge Thickness and Clinical Disease Stage in Retinopathy of Prematurity," JAMA Ophthalmol. 140(11), 1121–1127 (2022).

Thanh-Tin P. Nguyen, **Shuibin Ni**, Guangru Liang, Shanjida Khan, Xiang Wei, Alison H. Skalet, Susan Ostmo, Michael F. Chiang, Yali Jia, David Huang, Yifan Jian, and J. Peter Campbell, "Widefield Optical Coherence Tomography in Pediatric Retina: A Case Series of Intraoperative Applications Using a Prototype Handheld Device," Front. Med. 9, 860371 (2022).

Shuibin Ni, Thanh-Tin P. Nguyen, Ringo Ng, Mani Woodward, Susan Ostmo, Yali Jia, Michael F. Chiang, David Huang, Alison H. Skalet, J. Peter Campbell, and Yifan Jian, "Panretinal Optical Coherence Tomography," IEEE Trans. Med. Imaging 42(11), 3219–3228 (2023).

ROP typically affects both eyes and is most common in infants born before 31 weeks of gestation or with a birth weight under 1250 grams. Its pathophysiology is multifactorial, involving genetic, environmental, and physiological factors. Key risk factors include premature birth, which interrupts retinal blood vessel development, and low birth weight, which correlates with incomplete retinal vasculature. Supplemental oxygen, although essential for preterm infants' survival, can disrupt normal vascular development, necessitating careful oxygen therapy management. The disease starts with oxygen-induced vessel loss and is followed by abnormal vessel proliferation driven by hypoxia and elevated vascular endothelial growth factor (VEGF).

The International Classification for ROP (ICROP) was introduced in 1984 [127], expanded in 1987, revisited in 2005, and the third edition was released in 2021 [103]. This classification system enabled the first large-scale treatment trial for ROP, the Cryotherapy for ROP (CRYO-ROP) study led by the Oregon Health & Science University (OHSU) [115]. The pivotal clinical trial demonstrated that cryotherapy significantly reduces the risk of retinal detachment and blindness in infants with advanced ROP. The findings of the CRYO-ROP study have had a lasting impact, guiding treatment protocols and improving outcomes for countless premature infants.

The primary goal of ROP treatment is to prevent the disease from progressing to stages where retinal detachment and significant vision loss can occur. ICROP provides a uniform language for describing ROP severity and extent, enabling consistent diagnosis and treatment across medical centers. ICROP categorizes ROP by the zone (anterior-posterior border of the non-vascularized retina), extent (number of clock hours of disease), stage (degree of vascular abnormality at the avascular border), and the presence or absence of arterial tortuosity and venous dilation in the posterior retina, called plus disease [53,127]. The Early Treatment for ROP

(ETROP) study further classified eyes into type 1 (severe, requiring treatment), type 2 (moderate), mild ROP (less than type 2 but with stage 1 disease), and no ROP [116].

Early detection of ROP is crucial for timely intervention and preventing vision loss. Screening programs are essential in neonatal care, involving regular eye examinations from a few weeks after birth until the retinal blood vessels are fully matured. The standard care involves weekly or bi-weekly dilated binocular indirect ophthalmoscopy with scleral depression. ROP examinations pose medical risks to fragile neonates, being physiologically stressful [128], and increasing the risk of cardiopulmonary complications. Minimizing exam duration and bright lights can reduce the risk. Additionally, these exams require pharmacologic pupillary dilation [129], which can lead to systemic complications and add time and cost to care [130]. The introduction of ultra-widefield handheld optical coherence tomography (OCT) and OCT angiography (OCTA) imaging systems has the potential to enhance the accuracy and efficiency of ROP diagnosis, allowing clinical diagnosis without pharmacologic dilation, bright light, or scleral depression.

The real-time *en face* visualization allows handheld OCT/OCTA imaging systems to function similarly to an ophthalmoscope, providing an adequate field of view (FOV) and improved contrast for visualizing the border between the vascular and avascular retina. Figure 7.1 shows posterior and peripheral images obtained using 55° and 105° FOV devices, as presented in Chapters 2 and 3, respectively. Typically, peripheral stage visualization with a small FOV requires scleral depression. We evaluated if combining scleral depression with 55° FOV handheld OCT could effectively detect and visualize the peripheral stage. In most cases, the peripheral stage could be objectively assessed. In most cases, such as those with swollen eyelids from continuous positive airway pressure (CPAP) or clinical instability, standard ophthalmoscopic examination to rule out significant disease while minimizing stress from research imaging. In these cases, *en face* OCT

often provided better sensitivity for detecting subtle changes at the vascular-avascular border, although this was not performed in a masked fashion.

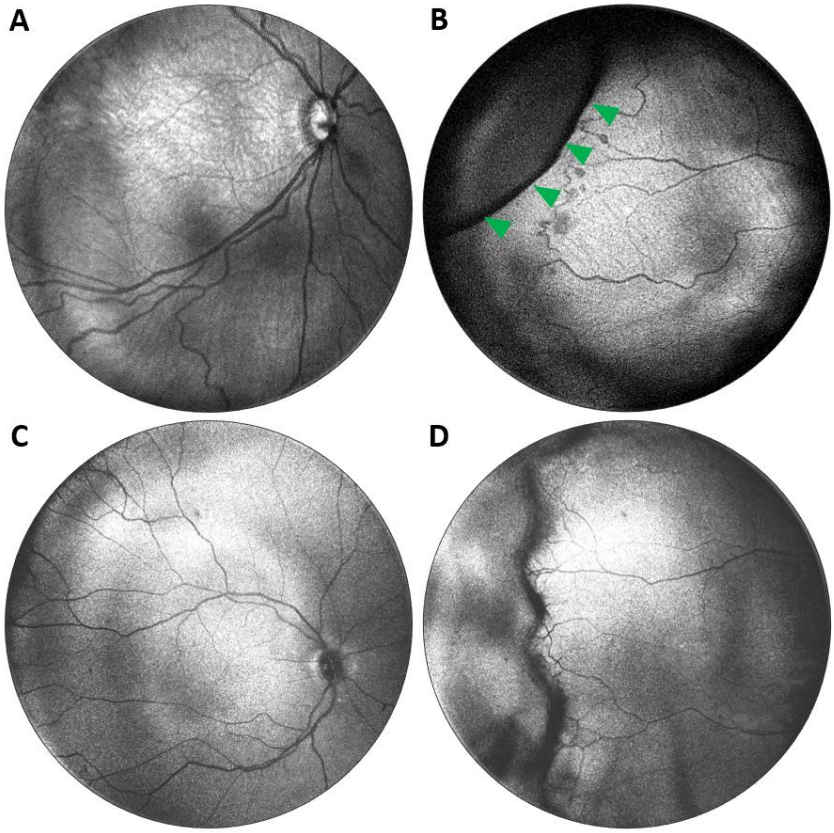

Figure 7.1 Posterior and peripheral *en face* images acquired using portable 55° and 105° FOV OCT systems. (A) and (B) display images captured with a 55° FOV system, while (C) and (D) show images from a 105° FOV system. Posterior images in (A) and (C) highlight the benefits of an expanded FOV. Peripheral images in (B) and (D) were obtained with the assistance of scleral depression. Green arrowheads point to the indentation created by the scleral depressor.

Serial evaluation of fundus photos is valuable for detecting disease progression [131]. *En face* visualization provides sufficient detail to assess changes in disease severity over time [Figure 7.2(A)-Figure 7.2(C)] through direct comparison with prior images. When evaluating intravitreal bevacizumab treatment, direct comparison of *en face* OCT images of the posterior pole and retinal

periphery showed a reduction in the stage and extent of peripheral disease and the degree of plus disease [Figure 7.2(D)-Figure 7.2(F)].

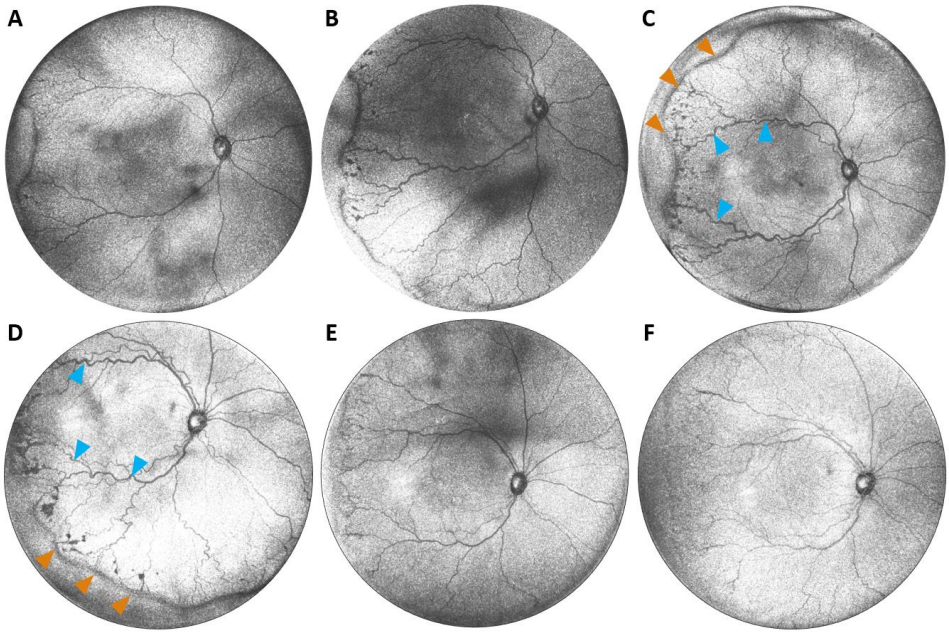

Figure 7.2 (A)-(C) Serial widefield OCT images taken over three consecutive weeks from a baby born at 25 weeks gestation (449 grams), captured at 36-, 37-, and 38-weeks postmenstrual age. These images display the posterior and peripheral retina in a single view, tracking the progression of arterial and venous tortuosity and fibrovascular proliferation. Cyan arrowheads mark areas of increased dilation and tortuosity, while orange arrowheads highlight the peripheral ridge, which has grown over time, along with popcorn neovascularization posterior to the ridge. (D)-(F) Serial images before and after treatment in the same infant at 38-, 39-, and 40- weeks postmenstrual age. (D) Posterior *en face* view immediately before treatment with 0.625 mg intravitreal bevacizumab. (E) Regression of disease one week after treatment. (F) Further regression two weeks after treatment. Cyan arrowheads indicate pre-treatment vascular tortuosity that improves post-treatment, and orange arrowheads highlight areas of pathologic neovascularization that become less dense post-treatment.

Accurate ROP diagnosis is essential for timely treatment and reducing blindness risk. However, ROP examination components are subjective and qualitative. Using the expanded FOV, we can evaluate whether OCT–derived retinal thickness measurements at the vascular-avascular

junction correlate with clinical ROP stage diagnosis. Figure 7.3(A)-Figure 7.3(C) shows the methodology for assessing ridge thickness. We compared OCT-derived ridge thickness to clinical ROP stage diagnosis using an ordinal scale, assessing repeatability with 20 repeated examinations from the same visit and comparing results using intraclass correlation coefficient (ICC) and coefficient of variation (CV). Comparison with ordinal categories was performed using generalized estimating equations. We have demonstrated that the peripheral stage is measurable as a continuous variable (OCT ridge thickness) and is associated with clinical stage diagnosis [77].

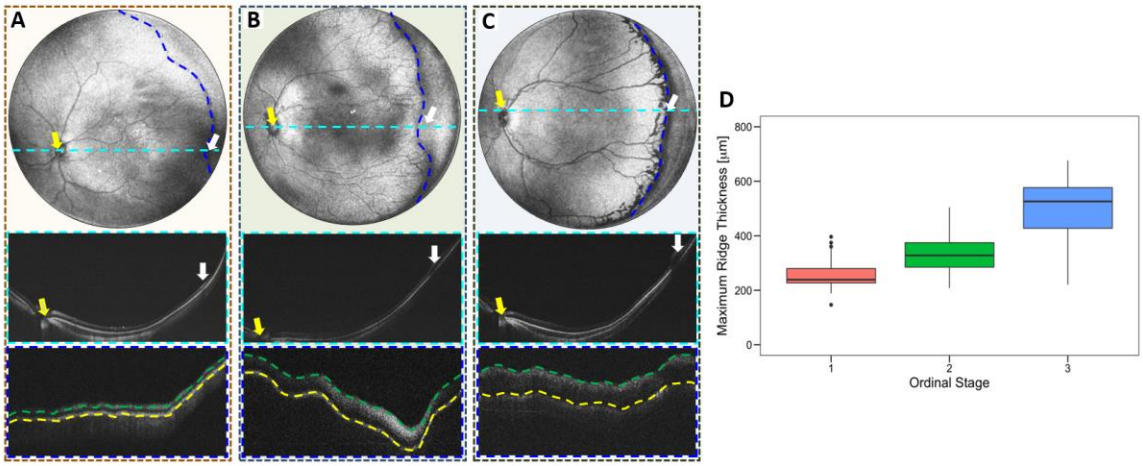

Figure 7.3 (A)-(C) Top row: OCT *en face* images with manual tracing of the fibrovascular ridge (blue dashed line). Corresponding B-scans (bottom row) are segmented between the retinal pigment epithelium (yellow dashed line) and inner ridge surface (green dashed line) to measure thickness. Middle row: B-scans from the optic nerve (yellow arrows) to the ridge, with the ridge peak indicated by white arrows. (A) to (C) depict stages 1, 2, and 3, respectively. (D) Plot of fibrovascular ridge axial thickness by ordinal stage labels. Higher ridge thickness on OCT correlates with higher stage labels ($P < .001$).

7.2 Retinoblastoma

Retinoblastoma is a rare but aggressive intraocular cancer affecting young children. While the mortality rate is less than 5% in high-income countries, it rises to about 70% in low- and middle-income countries due to the lack of timely screening and treatment [132–135]. Annually,

approximately 9,000 new cases are confirmed globally, with most affected children not surviving [132,136]. Retinoblastoma is hereditary, necessitating frequent screenings for children with a family history, especially during their first year of life.

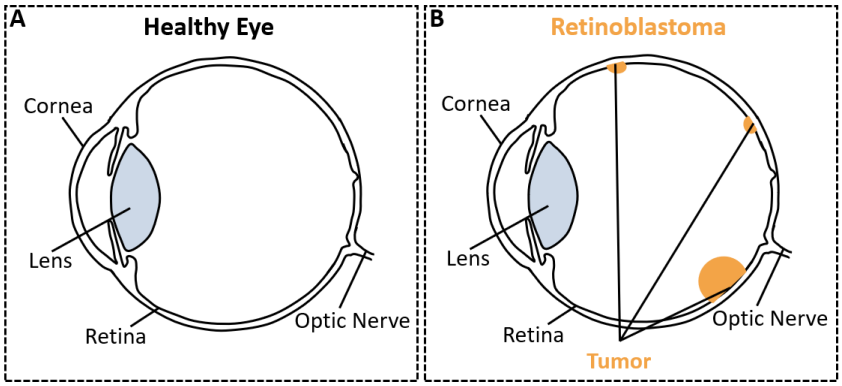

Figure 7.4 Diagram of a healthy eye and an eye affected by retinoblastoma.

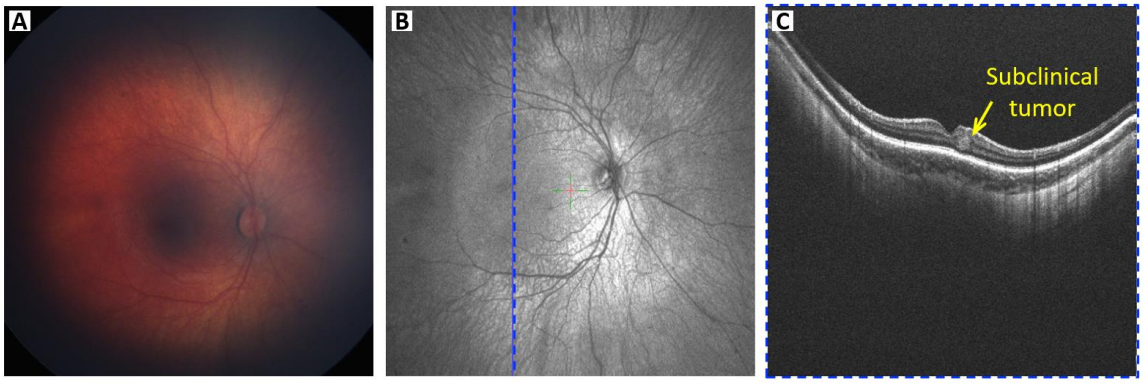

Figure 7.5 A pilot study using a panretinal handheld OCT imaging system successfully identified a subclinical tumor near the fovea in a 5-month-old patient with bilateral retinoblastoma. (A) The tumor was not visible in the fundus camera image. (B) An *en face* OCT image captured by the handheld OCT system. (C) A selected cross-sectional image corresponding to the blue line in (B). This advanced imaging technology allows for the early detection of otherwise invisible tumors.

Retinoblastoma can develop anywhere on the retina (Figure 7.4) and often leads to the formation of multiple tumors over time [137]. Comprehensive retinal evaluation is crucial to document and monitor the entire retinal area [137]. Current screening methods involve the use of a head-mounted ophthalmoscope and scleral indentation to examine the peripheral retina. This

process takes about 5-10 minutes per section, often requiring sedation for the child. In addition to indirect ophthalmoscopy, magnetic resonance imaging (MRI), and the ocular ultrasound are commonly used to diagnose retinoblastoma [138–140]. These traditional imaging tools suffer from inefficiencies related to imaging time, resolution, and FOV, limiting their effectiveness.

Besides that, conventional screening methods such as indirect ophthalmoscope and fundus cameras are insensitive to subclinical tumors [Figure 7.5(A)]. The doubling time of retinoblastoma tumors is estimated to be around 15 days [141]. This indicates that a tumor missed during routine screening can increase in size fourfold by the next month. Therefore, early detection is crucial to starting treatment immediately. Large tumors and tumors located near critical anatomy such as fovea or optic disc are treated with multimodal therapy, including chemotherapy, while smaller tumors located away from these structures can be treated with focal ablative therapy alone to avoid chemotherapy toxicity. Identifying residual visible tumors in treatment scars can be challenging with conventional imaging modalities. If these small tumors are unrecognized, they may result in recurrence and require more aggressive treatments, leading to vision loss or eye globe loss. The application of OCT imaging technology provides several advantages, such as detection of emerging subclinical tumors [Figure 7.5(B) and Figure 7.5(C)] and residual tumors in treatment scars [142–144].

However, traditional OCT devices are bulky and require patients to be positioned in front of the device, which can be challenging for young children. Handheld OCT devices overcome this issue by allowing clinicians to diagnose retinoblastoma without causing additional discomfort. However, existing handheld OCT devices have limitations in imaging speed, axial imaging range, and FOV, especially for the retinal periphery. Developing handheld OCT devices with ultrahigh-

speed and ultra-widefield capabilities would enable the capture of larger retinal areas at a faster rate, improving real-time monitoring and early tumor detection.

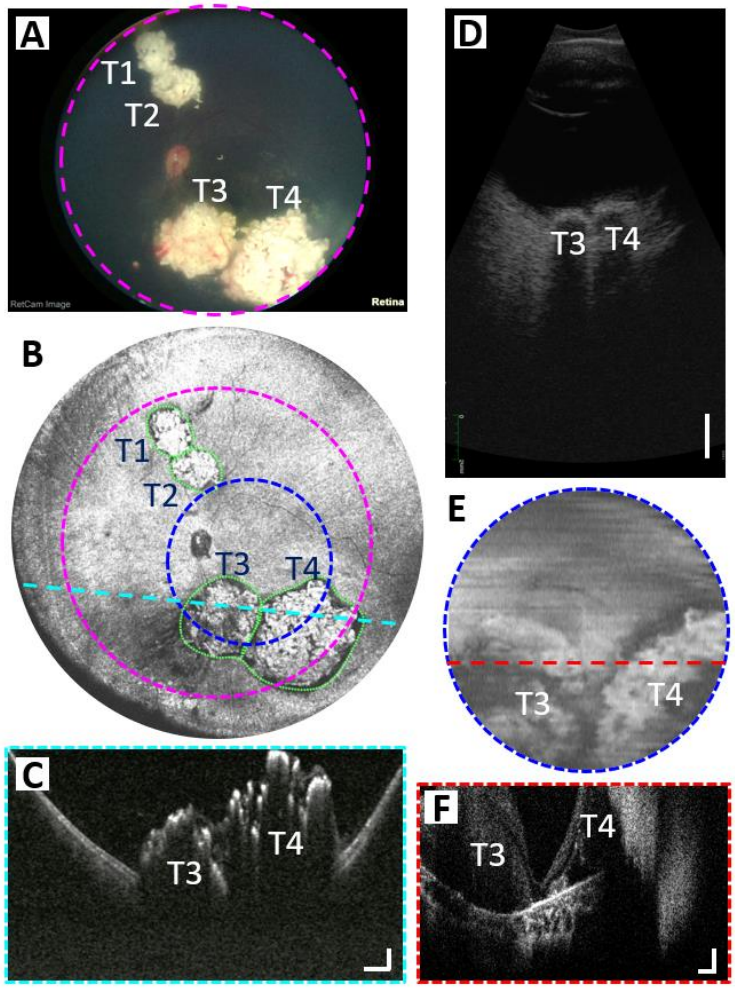

Figure 7.6 (A) RetCam color fundus image from a patient with multifocal retinoblastoma (tumors labeled as T1-T4). (B) *En face* OCT image obtained by our contact handheld SS-OCT system. (C) Selected B-scan image corresponding to the location of the dashed cyan line. Scale bars are 1 mm (horizontally) and 500 μm (vertically). (D) Selected ultrasound B-scan image. Scale bar is 5 mm. (E) *En face* OCT image taken by Leica handheld OCT (Envisu C2300, Leica Microsystems, Germany). The imaging area was marked by a dashed blue circle in (B). (F) Selected B-scan image corresponding to the location of the dashed red line. Scale bars are 500 μm (horizontally) and 200 μm (vertically).

Additionally, quantitative measurement of tumor volume is crucial for assessing tumor growth and treatment response. It provides a more comprehensive and accurate assessment of tumor growth compared to traditional methods that rely solely on measuring tumor diameter or thickness. It could also provide an early warning of treatment failure or disease progression. The treatment of retinoblastoma typically involves a combination of chemotherapy, radiation therapy, and surgical intervention, and measurement of the tumor size is crucial for monitoring disease progression, determining the best course of treatment, and improving the patient's prognosis. Currently, the measurement of tumor size in retinoblastoma relies on imaging modalities like ultrasound or MRI, which can be time-consuming, costly, and inconvenient for patients. However, the utilization of a contact handheld OCT device with ultrahigh-speed and ultra-widefield capabilities presents an opportunity to enhance the accuracy and efficiency of tumor growth assessment. This advanced device can capture multiple images of the retina within a shorter duration and cover a larger area of the retina. This could aid in the early detection of tumor growth or recurrence, enabling earlier intervention and better outcomes.

To demonstrate the panoramic imaging capability of our handheld OCT system proposed in Chapter 5, an 18-month-old patient with multifocal retinoblastoma was imaged under general anesthesia during routine follow-up care. RetCam color fundus image, representative ocular ultrasound B-scan (Eye Cubed I3 V-4, Ellex, Australia), and study OCT images are shown in Figure 7.6. The contact handheld panretinal OCT acquired quantitative three-dimensional images over the retina with significantly wider FOV compared to the commercially available handheld retinal imaging systems, such as Leica Envisu C-Class OCT and Natus RetCam. With Leica HH OCT, small portions of the tumors T3 and T4 were visible on the *en face* image and B-scan, due to the limited FOV and axial imaging range.

For this eye, the AL measured by the ocular ultrasound B-scan was 21.5 mm and by the contact handheld OCT system was 22.14 mm. The ocular ultrasound B-scan that was acquired with the 10 MHz posterior mode had an axial resolution of 50 μm and lateral resolution of 100 μm. The axial eye length measured on the ultrasound B-scan was from the anterior corneal vertex to the internal limiting membrane (ILM); whereas, with the OCT, the OPL was measured up to the retinal pigment epithelium (RPE) [102]. In addition, due to the lack of volumetric imaging capability, it is difficult to identify exactly where the ultrasound B-scan was taken on the retina, and the fovea was not present on the ultrasound B-scan, which also contributes to this discrepancy. In this eye, four retinoblastoma tumors were labeled as T1-T4, as shown in Figure 7.6(B). The raw OCT volume data was processed and rendered volumetrically. Then the corresponding sizes of the tumor were fitted according to the retinal curvature. The dimensions of the tumors were calculated and listed in Table 7.1.

In retinoblastoma care, documentation of tumor size and location as well as ongoing monitoring of tumor size and morphology are of critical importance in evaluating response to treatment and identifying tumor recurrence. Quantitative volumetric measurement using the contact handheld panretinal OCT system could significantly improve the reliability of clinical assessment for tumor control in retinoblastoma patients and lead to improved outcomes.

Table 7.1: Tumor size of retinoblastoma at different positions

	Length (mm)	Width (mm)	Height(mm)
Tumor 1 (T1[a])	6.37	3.05	1.41
Tumor 2 (T2)	5.2	4.04	1.08
Tumor 3 (T3)	5.48	4.71	1.56
Tumor 4 (T4)	9.08	7.14	2.84

Note:

[a]: The labels of the tumor (T1-T4) are shown in Figure 7.6(B).

7.3 Incontinentia Pigmenti

Incontinentia Pigmenti (IP) is a rare, X-linked dominant disorder caused by mutations in the NEMO gene. This disease predominantly affects females and is typically lethal in males who inherit the mutation. IP impacts multiple body systems, including the skin, hair, teeth, central nervous system, and eyes, with significant implications for ocular health [145]. The ocular manifestations of IP often involve the retina, leading to vascular occlusion, neovascularization, optic nerve atrophy, and in later stages retinal detachment [146]. Similar to ROP, preretinal neovascularization in IP is typically found in the retinal periphery at the border of the avascular retina [146,147].

Early detection and continuous monitoring of retinal changes in IP are crucial to preventing severe visual impairment. Traditional screening methods, such as indirect ophthalmoscopy and fundus photography, provide limited FOV and may miss subtle neovascular changes, particularly in the peripheral retina. Furthermore, these methods can be challenging to perform in infants and young children due to the need for patient cooperation and often require sedation. Handheld OCT imaging systems offer a significant advancement in the screening and management of IP. These devices provide high-resolution, cross-sectional images of the retina, allowing for detailed visualization of retinal layers and vascular structures. The portability and ease of use of handheld OCT imaging systems make them particularly suited for pediatric patients, enabling comprehensive retinal examination without the need for sedation.

Handheld OCT can capture detailed images of the retina, including the peripheral regions, where preretinal neovascularization is commonly found in IP. This capability is crucial for early detection and monitoring of retinal changes, allowing for timely intervention to prevent vision

loss. The ability to perform *en face* OCTA with handheld devices further enhances their utility, providing detailed maps of retinal blood flow and identifying areas of neovascularization and vascular occlusion.

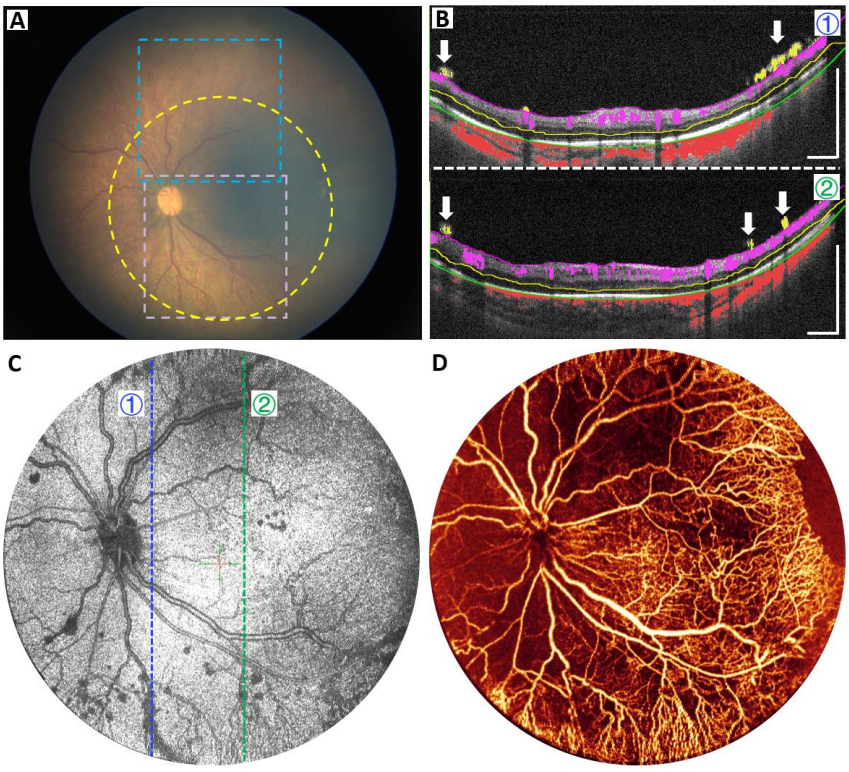

Figure 7.7 (A) RetCam fundus images of a 6-week-old baby presented with Incontinentia Pigmenti (IP). The cyan box and light purple box show the area of a 40° FOV (see Fig. 7.8). (B) Two selected B-scans reveal preretinal neovascularization (yellow vessels pointed by white arrows). (C) Handheld *en face* OCT image with 55° FOV in the blue circle of fundus photograph. (D) Corresponding OCTA of the inner retina.

Figure 7.7 and Figure 7.8 illustrate the application of a widefield handheld OCT/OCTA imaging system, proposed in Chapter 2, in a 6-week-old baby with IP. Figure 7.7 and Figure 7.8 show the RetCam fundus, *en face* OCT image, and OCTA with 55° FOV in different areas. Figure 7.8(A) and Figure 7.8(B) show the 40° FOV *en face* OCTA of the inner retina with the neovascular area from the cyan box and light purple box of the RetCam fundus [Figure 7.7(A)]. The inner

retina *en face* OCTA images were generated using the maximum projection method, with a customized purple color map applied for clarity. Neovascular OCTA signals above the internal limiting membrane (ILM) layer and within the vitreous were projected using a customized yellow color map, overlaid with the inner retina *en face* OCTA image. Vascular networks and pathologies were visualized more clearly without pronounced motion artifacts.

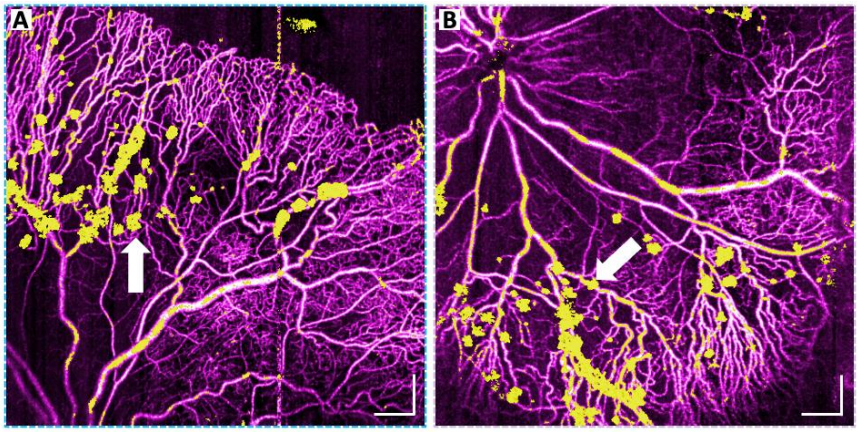

Figure 7.8 40° FOV *en face* OCTA of the inner retina showing neovascular area (yellow vessels pointed by white arrows) in the cyan box (A) and light purple box (B) of fundus photograph [Figure 7.7(A)]. Scale bars are 1 mm.

High-speed and widefield handheld OCT/OCTA imaging system represents a significant advancement in the early detection and management of retinal complications in IP. This device offer detailed imaging capabilities that are crucial for identifying and monitoring retinal vascular changes, allowing for timely and effective intervention. The integration of en face OCTA further enhances the ability to visualize retinal blood flow and neovascularization, providing a comprehensive tool for managing IP in pediatric patients.

7.4 Coats Disease

Coats disease is a rare, idiopathic retinal vascular disorder that primarily affects young males [148]. The disease is characterized by retinal telangiectasia and abnormal dilated retinal

vessels, and can lead to significant vision-threatening complications such as exudative retinal detachment, glaucoma, cataracts, *etc.* [133]. The etiology of Coats disease is unknown, but it is often unilateral and presents in childhood. The condition progresses through various stages, starting with retinal telangiectasia and leading to advanced retinal exudation and detachment if left untreated. The exudation associated with Coats disease results in the accumulation of lipid-rich subretinal fluid, causing exudative retinal thickening and potential detachment.

Early and accurate diagnosis of Coats disease is crucial for preventing severe visual impairment. Traditional diagnostic methods include indirect ophthalmoscopy and fluorescein angiography, which can identify retinal telangiectasia and exudation but may be limited in visualizing the full extent of retinal pathology, particularly in the retinal periphery. These methods can be challenging to perform in young children due to the need for patient cooperation and may require sedation. Ultra-widefield handheld OCT imaging systems offer a significant advancement in the diagnosis and management of Coats disease. This device provides high-resolution, cross-sectional images of the retina, allowing for detailed visualization of retinal layers and vascular structures. The portability and ease of use of ultra-widefield OCT imaging systems make them particularly suited for pediatric patients, enabling comprehensive retinal examination without the need for sedation.

The use of ultra-widefield handheld OCT in Coats disease allows for detailed imaging of the retinal periphery, where telangiectasia and exudation are commonly found. This capability is crucial for early detection and monitoring of retinal changes, facilitating timely intervention to prevent vision loss. Figure 7.9 demonstrates a representative example of Coats disease acquired by contact handheld panretinal OCT proposed in Chapter 5. Note that retinal telangiectasia in Coats disease is often associated with exudation, which can lead to exudative retinal thickening as

shown in Figure 7.9(B), and at times detachment. The ability to visualize these changes in detail highlights the value of panretinal OCT imaging in diagnosing Coats disease.

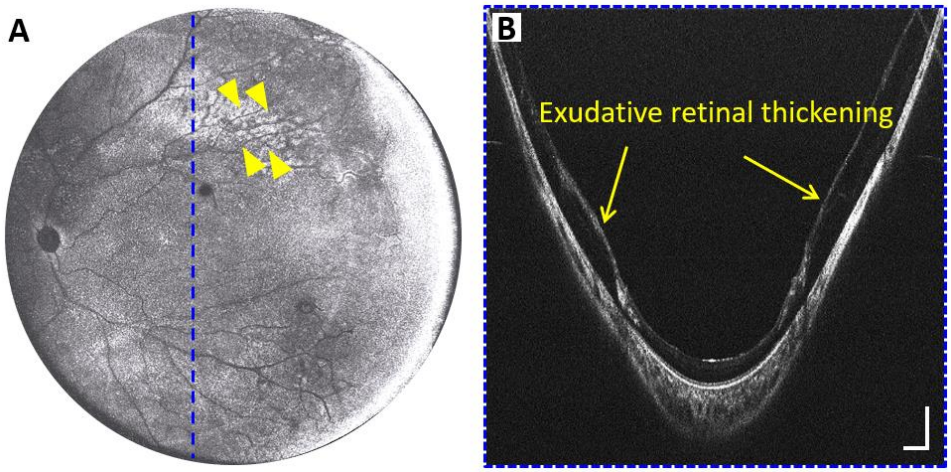

Figure 7.9 (A) *En face* OCT image from a patient with Coats disease (yellow arrowheads). (B) Selected cross-sectional scan with the regions of extramacular exudation and retinal thickening corresponding to the location of the dashed blue line in (A). Scale bars in (B) are 1 mm (horizontally) and 500 μm (vertically).

Ultra-widefield handheld OCT imaging system represents a significant advancement in the early detection and management of Coats disease. This device offers detailed imaging capabilities that are crucial for identifying and monitoring retinal vascular abnormalities and exudation, allowing for timely and effective intervention. The integration of panretinal imaging further enhances the ability to explore the retinal periphery, providing a comprehensive tool for managing Coats disease in pediatric patients.

7.5 Retinal Detachment

Retinal detachment (RD) is a sight-threatening condition in which the neurosensory retina separates from the underlying retinal pigment epithelium (RPE). Prompt identification and differentiation of the type of retinal detachment are crucial for guiding appropriate treatment [78]. There are three main types of retinal detachments: tractional, exudative, and rhegmatogenous (and

combined mechanism) in children [78]. Each type has different underlying mechanisms and requires distinct management strategies. Tractional retinal detachments (TRD) occur due to vitreoretinal traction from epiretinal neovascularization with fibrosis. Exudative retinal detachments (ERD) result from the accumulation of subretinal fluid without a retinal break, often due to inflammation or vascular abnormalities. Rhegmatogenous retinal detachments (RRD) are caused by a retinal break that allows fluid to pass from the vitreous cavity into the subretinal space.

Handheld OCT devices, especially those with widefield capability, provide a significant advantage in diagnosing and managing retinal detachments, particularly in pediatric patients. These portable devices facilitate the evaluation of various types of retinal detachments by capturing detailed cross-sectional scans and *en face* images of the retina. Figure 7.10 and Figure 7.11 provides examples of tractional retinal detachment (TRD) in children. The images were acquired by a widefield handheld OCT/OCTA imaging system proposed in Chapter 2. TRD is commonly related to peripheral epiretinal neovascularization with fibrosis, leading to vitreoretinal traction and macular dragging. Figure 7.10 reveals an early stage 4a detachment in ROP with tractional schisis but no subretinal fluid. This level of detail, achievable through OCT, is critical for clear detection and intervention. Figure 7.11 shows the distortion of normal retinal architecture and macular dragging due to TRD. Figure 7.12 illustrates an RRD with a large temporal retinal break in a 3-year-old girl. This type of detachment is characterized by a retinal tear allowing fluid to enter the subretinal space, which can be effectively visualized using OCT.

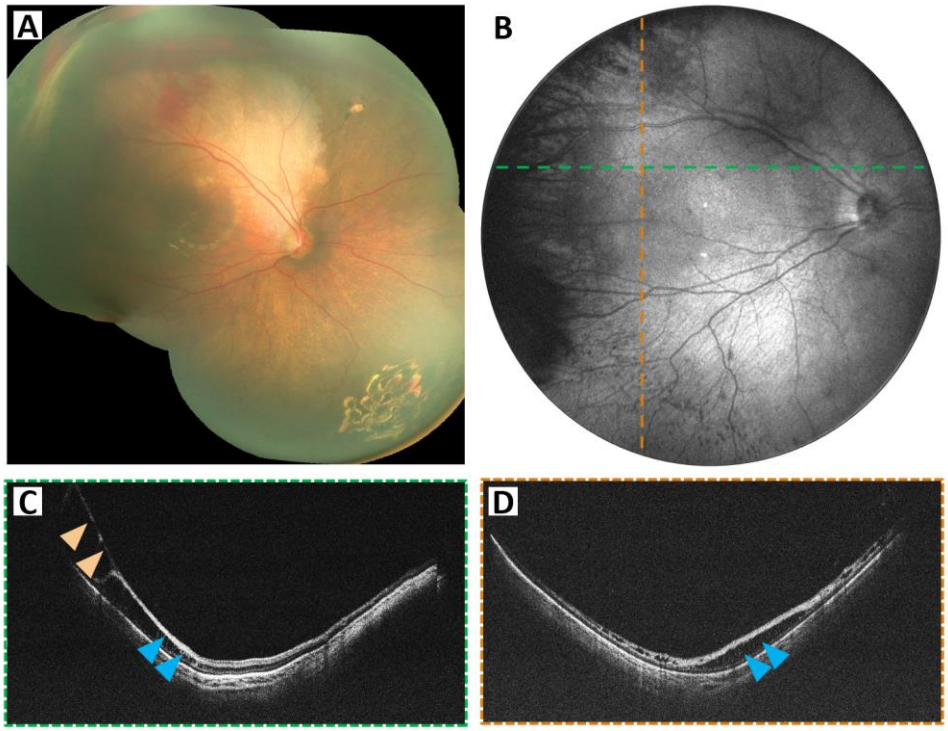

Figure 7.10 Widefield OCT evaluation of tractional retinal disease in a 4-month-old with Stage 4a ROP, born at 24 weeks gestation. (A) Montage of fundus photographs. (B) 105° FOV OCT *en face* image with dotted lines indicating the locations of the B-scans in (C) and (D). Orange arrowheads denote vitreoretinal traction, while cyan arrowheads indicate areas of schisis.

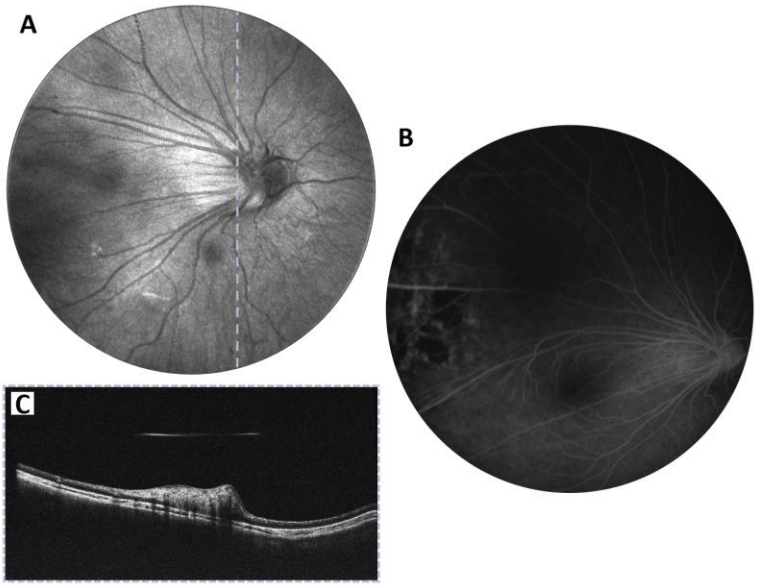

Figure 7.11 Widefield OCT evaluation of tractional retinal disease in a 3-year-old patient with FEVR. (A) Structural *en face* projection taken with the 55° FOV OCT imaging system. (B) Fluorescein angiography (FA) image. (C) B-scan corresponding to the dotted line in (A).

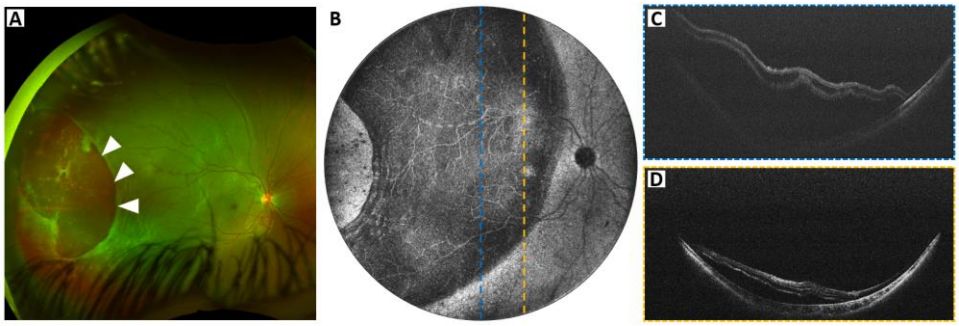

Figure 7.12 Evaluation of rhegmatogenous retinal detachment (RRD) in a 5-year-old girl using widefield OCT. (A) Ultra-widefield fundus photograph with white arrowheads marking a large temporal break. (B) 105° FOV OCT *en face* image, with dotted lines indicating the locations of the B-scans shown in (C) and (D).

Figure 7.13 shows an eye with an exudative retinal detachment, acquired by the handheld panretinal OCT system proposed in Chapter 5. The images capture the morphology of retinal elevation, which aids in distinguishing ERD from other types of detachments. Following treatment with topical corticosteroid and panretinal photocoagulation, the detachment improved, as shown in Figure 7.13(C) and Figure 7.13(D). However, the patient subsequently developed retinal traction, necessitating a pars plana vitrectomy (PPV). Figure 7.13(E)-Figure 7.13(J) demonstrate the utility of OCT to evaluate and monitor retinal repair post-operatively, highlighting the importance of OCT in ongoing patient treatment.

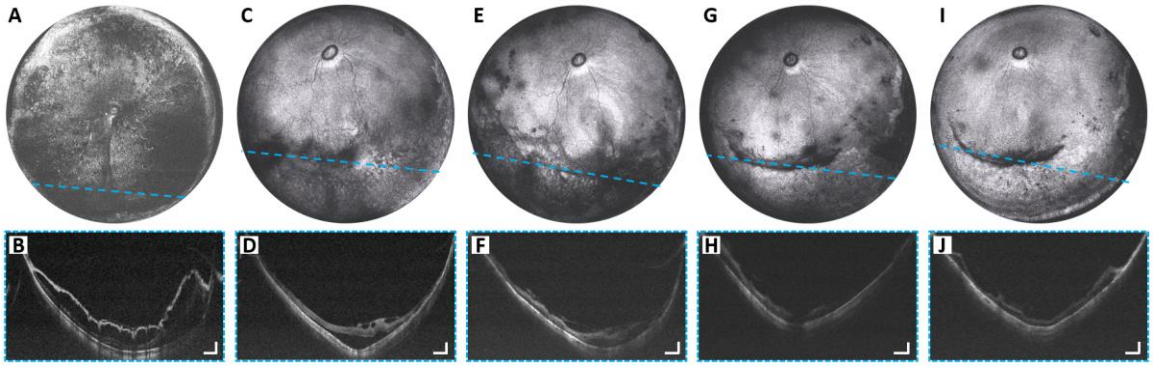

Figure 7.13 Morphological changes in the retina of the patient with retinal detachment with different therapeutic interventions. The images on the first row are *en face* OCT images. The images on the second row are selected cross-sectional scans. The dashed cyan lines indicate the location of the corresponding cross-sectional scans. (A)-(B) One week after panretinal photocoagulation laser treatment. (C)-(D) Three weeks after panretinal photocoagulation laser treatment. (E)-(F) Two weeks after PPV surgery. (G)-(H) Six weeks after PPV surgery. (I)-(J) Seven weeks after PPV surgery. The PPV surgery was performed six weeks after the panretinal photocoagulation laser treatment. Scale bars are 1 mm (horizontally) and 500 μm (vertically).

Handheld OCT devices, with their ability to provide widefield images, represent a significant advancement in the diagnosis and management of retinal detachments in pediatric patients. These devices allow for the detailed visualization of retinal structures, enabling the differentiation of traction, exudative, and rhegmatogenous detachments. This capability is crucial for guiding appropriate treatment and improving patient outcomes, particularly in the challenging pediatric population where traditional imaging methods may be less effective.

CHAPTER 8. FUTURE WORK AND CONCLUSION

8.1 Future Work

The earlier systems faced challenges such as limited imaging speed and suboptimal optical design, which hindered the integration of OCTA mode in ultrawide imaging [79,80,83]. The most advanced prototype has addressed these limitations by developing a faster OCT engine with improved optical performance, enabling the first successful implementation of panretinal OCTA in premature infants. This was achieved by using an optical relay to separate the optical scanners and two off-the-shelf aspherical lenses. Despite the unprecedented field of view (FOV), achieving the desired transverse resolution for imaging capillaries and small vessels remains challenging due to limited off-the-shelf optics options. Leveraging our expertise in designing and manufacturing advanced optical lenses for ophthalmic imaging, we demonstrated a desktop non-mydriatic and non-contact ultra-widefield OCT system (Chapter 4) with completely custom-designed lenses, achieving a 100° FOV with 20 μm transverse resolution [149]. Building on this success, in the future, we aim to develop completely custom-made optics for a next-generation panretinal handheld OCTA imaging system, enabling non-mydriatic imaging for pediatric patients. This approach is less invasive and more comfortable, enhancing the efficiency of the imaging process, particularly in clinical settings where patients' comfort is prioritized. Recent simulation results (Figure 8.1) indicate significant improvement in beam wandering compared to the most advanced prototype. The novel design, incorporating fully custom-made optics, condenses the scanning laser beam for all incident angles, ensuring they remain centered and smaller than the resting pupil diameter, thus facilitating non-mydriatic retinal imaging.

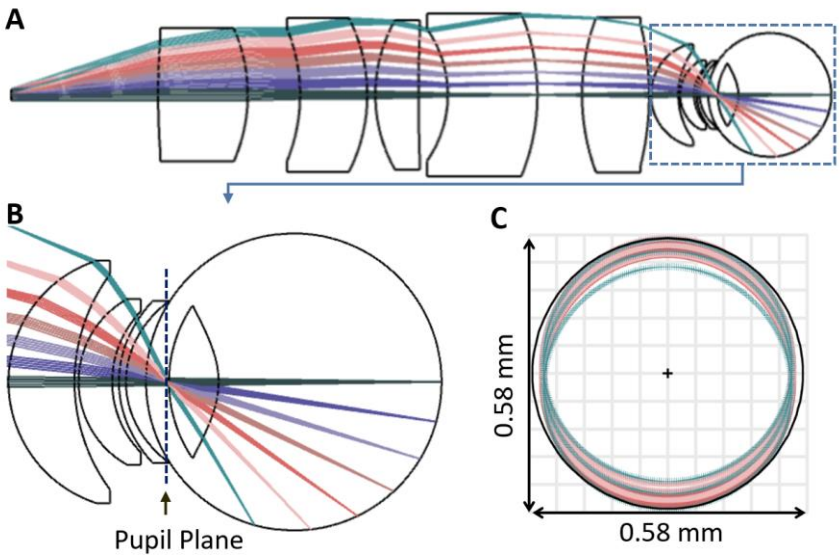

Figure 8.1 (A) Schematic diagram of the ultra-widefield handheld contact eyepiece design. (B) Detailed view of the footprint on the pupil plane. (C) Beam wandering on the pupil plane across the wavelength range of 1010 nm to 1110 nm. Scale bars indicate 0.58 mm.

Although the scanning pivot point is preset to minimize vignetting artifacts, the lens design with a predetermined curvature and working distance cannot accommodate the rapid growth of the eyes in premature infants. Additionally, the contact imaging method requires skilled ophthalmologists for image acquisition, like current wide-field digital fundus imaging systems. However, this contact-based approach allows maximal eye position control, reduces alignment time, minimizes optical aberrations, and enhances image quality. The contact-based lens design is critical for achieving the record-setting FOV but has two critical limitations: the fixed contact surface cannot be deep-cleaned efficiently, raising concerns about disease transmission, and the fixed curvature and position of the lens do not accommodate the varying size of neonatal eyes. This results in suboptimal placement of the beam scanning pivot point on the pupil plane, affecting non-mydriatic imaging consistency. In our latest panretinal handheld OCTA imaging system, the scanning beam pivot point aligns with the pupil plane only when eye parameters match the design

specifications, requiring a minimum pupillary size. Eyes with significant deviations from these parameters displace the scanning beam pivot, limiting the FOV due to the constriction of the non-dilated pupil. To address these issues, we plan to develop several sets of rigid gas permeable concave lenses that can be interchangeably fixed to the panretinal handheld OCTA system. The new design will feature a posterior surface of the gas-permeable lens that matches the corneal surface curvature, optimizing the working distance of the imaging probe and achieving non-mydriatic imaging.

Besides that, future work on the panretinal handheld contact OCT imaging system will also focus on enhancing its application for laser retinopexy in treating retinal tears. Diagnosing retinal tears requires clinicians to visualize the entire peripheral retinal up to the ora serrata. Our most advanced prototype has demonstrated the ability to image beyond the ora serrata (Figure 6.4) [83]. The goal is to further develop this prototype to diagnose retinal tears with minimal reliance on patient compliance and clinician technical skill, while also enabling laser photocoagulation using the same device. We plan to further refine our proprietary optical system to construct a prototype clinical ultra-widefield OCT-guided laser retinopexy system. This system will integrate the standard of care Iridex ophthalmic laser into our handheld imaging probe via a dichroic mirror and a 2D microelectromechanical systems (MEMS) scanner that generates treatment patterns.

There are three primary challenges to implementing panretinal OCT imaging effectively: imaging speed, axial image range, and axial resolution. The large retinal curvature in ultra-widefield imaging requires a long axial image range, necessitating numerous measurements that current signal capture electronics struggle to handle efficiently. For instance, achieving a 5 μm resolution over a 15 mm depth range requires 6000 measurements for each A-scan. Current technology can achieve an A-scan rate of 667 kHz or less, resulting in a minimum acquisition time

of 6 seconds or more for a comprehensive retinal scan, which is too slow for practical use. To address these challenges, future developments will focus on two main areas. The first is to implement Circular-Ranging (CR) OCT, which uses an optical frequency comb source to drastically reduce the number of necessary measurements [109,150,151]. In CR-OCT, the number of measurements is proportional to the sample's thickness, not the imaging depth range. This method reduces the required samples, allowing A-scan rates up to 16.7 MHz with a 4 Giga samples/second capture board, significantly improving imaging efficiency. The second area is the development of Stretched-Pulse Mode-Locked (SPML) frequency comb lasers [152–154]. These novel light sources, capable of retinal imaging at rates greater than 10 MHz (100 times faster than current FDA-approved OCT imaging systems), are crucial for effectively implementing the CR-OCT technique. They address the challenge posed by existing light sources, which cannot match the required speeds for CR-OCT, thus leveraging the data advantages offered by this innovative method. By focusing on these improvements, the aim is to create a more efficient and reliable ultra-widefield OCT system that can provide comprehensive retinal imaging and treatment in a clinically practical timeframe.

8.2 Conclusion

This dissertation outlines the comprehensive development of a handheld OCT imaging system designed for pediatric retinal imaging, aimed at achieving panretinal OCT/OCTA imaging. The research began with an initial prototype that, despite its limitations in FOV and optical performance, established a foundation for significant advancements in subsequent iterations. These iterations progressively improved imaging speed, FOV, optical performance, and usability. The first handheld prototype achieved a 400 kHz imaging speed and a 55° FOV but required enhancements to visualize the entire peripheral retina. Through iterative development, prototypes

were created with an expanded FOV of up to 140°, incorporating custom optics and innovative design modifications such as the contact approach. These modifications significantly improved alignment time, image quality, and success rates, particularly in infant imaging. The most advanced prototype utilized a customed-design lens group and dual aspherical lenses, delivering superior image quality and enabling panretinal OCTA.

These handheld systems proved effective in diagnosing and monitoring various pediatric retinal diseases, including retinopathy of prematurity, retinoblastoma, Coats disease, and retinal detachment. The ability to capture high-quality images and perform OCTA of both the posterior pole and peripheral retina in a single shot provides opportunities for early detection of these conditions. This dissertation underscores the transformative potential of handheld OCT and OCTA technology in pediatric ophthalmology. By addressing the limitations of traditional desktop OCT systems and existing portable devices, this research has paved the way for more effective and comprehensive retinal imaging in young patients. Their applications in pediatric ophthalmology are particularly beneficial, as early detection of retinal disorders can significantly influence treatment outcomes and overall prognosis.

REFERENCES

1. A. N. Kuo, R. P. McNabb, S. J. Chiu, M. A. El-Dairi, S. Farsiu, C. A. Toth, and J. A. Izatt, "Correction of ocular shape in retinal optical coherence tomography and effect on current clinical measures," Am. J. Ophthalmol. **156**(2), 304–311 (2013).
2. R. P. McNabb, J. Polans, B. Keller, M. Jackson-Atogi, C. L. James, R. R. Vann, J. A. Izatt, and A. N. Kuo, "Wide-field whole eye OCT system with demonstration of quantitative retinal curvature estimation," Biomed. Opt. Express **10**(1), 338–355 (2019).
3. B. Tan, R. P. McNabb, F. Zheng, Y. C. Sim, X. Yao, J. Chua, M. Ang, Q. V. Hoang, A. N. Kuo, and L. Schmetterer, "Ultrawide field, distortion-corrected ocular shape estimation with MHz optical coherence tomography (OCT)," Biomed. Opt. Express, BOE **12**(9), 5770–5781 (2021).
4. R. Grytz, M. El Hamdaoui, P. A. Fuchs, M. A. Fazio, R. P. McNabb, A. N. Kuo, C. A. Girkin, and B. C. Samuels, "Nonlinear distortion correction for posterior eye segment optical coherence tomography with application to tree shrews," Biomed. Opt. Express **13**(2), 1070–1086 (2022).
5. D. Huang, E. A. Swanson, C. P. Lin, J. S. Schuman, W. G. Stinson, W. Chang, M. R. Hee, T. Flotte, K. Gregory, C. A. Puliafito, and J. G. Fujimoto, "Optical coherence tomography," Science **254**(5035), 1178–1181 (1991).
6. J. Cehajic-Kapetanovic, K. Xue, R. Purohit, and C. K. Patel, "Flying baby optical coherence tomography alters the staging and management of advanced retinopathy of prematurity," Acta Ophthalmologica **99**(4), 441–447 (2021).
7. W. Jung, J. Kim, M. Jeon, E. J. Chaney, C. N. Stewart, and S. A. Boppart, "Handheld optical coherence tomography scanner for primary care diagnostics," IEEE Trans. Biomed. Eng. **58**(3), 741–744 (2011).
8. C. D. Lu, M. F. Kraus, B. Potsaid, J. J. Liu, W. Choi, V. Jayaraman, A. E. Cable, J. Hornegger, J. S. Duker, and J. G. Fujimoto, "Handheld ultrahigh speed swept source optical coherence tomography instrument using a MEMS scanning mirror," Biomed. Opt. Express **5**(1), 293–311 (2013).
9. D. Nankivil, G. Waterman, F. LaRocca, B. Keller, A. N. Kuo, and J. A. Izatt, "Handheld, rapidly switchable, anterior/posterior segment swept source optical coherence tomography probe," Biomed. Opt. Express **6**(11), 4516–4528 (2015).
10. F. LaRocca, D. Nankivil, T. DuBose, C. A. Toth, S. Farsiu, and J. A. Izatt, "In vivo cellular-resolution retinal imaging in infants and children using an ultracompact handheld probe," Nat. Photonics **10**, 580–584 (2016).
11. J. Yang, L. Liu, J. P. Campbell, D. Huang, and G. Liu, "Handheld optical coherence tomography angiography," Biomed. Opt. Express **8**(4), 2287–2300 (2017).
12. J. P. Campbell, E. Nudleman, J. Yang, O. Tan, R. V. P. Chan, M. F. Chiang, D. Huang, and G. Liu, "Handheld optical coherence tomography angiography and ultra–wide-field optical coherence tomography in retinopathy of prematurity," JAMA Ophthalmol. **135**(9), 977–981 (2017).
13. O. Nadiarnykh, V. Davidoiu, M. G. O. Grafe, M. Bosscha, A. C. Moll, and J. F. De Boer, "Phase-based OCT angiography in diagnostic imaging of pediatric retinoblastoma patients:

abnormal blood vessels in post-treatment regression patterns," Biomed. Opt. Express **10**(5), 2213–2226 (2019).
14. S. Song, K. Zhou, J. J. Xu, Q. Zhang, S. Lyu, and R. Wang, "Development of a clinical prototype of a miniature hand-held optical coherence tomography probe for prematurity and pediatric ophthalmic imaging," Biomed. Opt. Express **10**(5), 2383–2398 (2019).
15. C. Viehland, X. Chen, D. Tran-Viet, M. Jackson-Atogi, P. Ortiz, G. Waterman, L. Vajzovic, C. A. Toth, and J. A. Izatt, "Ergonomic handheld OCT angiography probe optimized for pediatric and supine imaging," Biomed. Opt. Express **10**(5), 2623–2638 (2019).
16. J. D. Malone, M. T. El-Haddad, S. S. Yerramreddy, I. Oguz, and Y. K. Tao, "Handheld spectrally encoded coherence tomography and reflectometry for motion-corrected ophthalmic optical coherence tomography and optical coherence tomography angiography," Neurophotonics **6**(4), 041102 (2019).
17. S. S. Gao, Y. Jia, M. Zhang, J. P. Su, G. Liu, T. S. Hwang, S. T. Bailey, and D. Huang, "Optical coherence tomography angiography," Invest. Ophthalmol. Vis. Sci. **57**(9), OCT27–OCT36 (2016).
18. R. F. Spaide, J. G. Fujimoto, N. K. Waheed, S. R. Sadda, and G. Staurenghi, "Optical coherence tomography angiography," Prog. Retin. Eye Res. **64**, 1–55 (2018).
19. E. D. Cole, E. M. Moult, S. Dang, W. Choi, S. B. Ploner, B. Lee, R. Louzada, E. Novais, J. Schottenhamml, L. Husvogt, A. Maier, J. G. Fujimoto, N. K. Waheed, and J. S. Duker, "The Definition, Rationale, and Effects of Thresholding in OCT Angiography," Oph. Retina **1**(5), 435–447 (2017).
20. W. Choi, E. M. Moult, N. K. Waheed, M. Adhi, B. Lee, C. D. Lu, T. E. de Carlo, V. Jayaraman, P. J. Rosenfeld, J. S. Duker, and J. G. Fujimoto, "Ultrahigh-speed, swept-source optical coherence tomography angiography in nonexudative age-related macular degeneration with geographic atrophy," Ophthalmology **122**(12), 2532–2544 (2015).
21. E. M. Moult, N. K. Waheed, E. A. Novais, W. Choi, B. Lee, S. B. Ploner, E. D. Cole, R. N. Louzada, C. D. Lu, P. J. Rosenfeld, J. S. Duker, and J. G. Fujimoto, "Swept-source optical coherence tomography angiography reveals choriocapillaris alterations in eyes with nascent geographic atrophy and drusen-associated geographic atrophy," Retina **36**(Suppl 1), S2–S11 (2016).
22. M. Zhang, T. S. Hwang, J. P. Campbell, S. T. Bailey, D. J. Wilson, D. Huang, and Y. Jia, "Projection-resolved optical coherence tomographic angiography," Biomed. Opt. Express **7**(3), 816–828 (2016).
23. A. Mariampillai, M. K. K. Leung, M. Jarvi, B. A. Standish, K. Lee, B. C. Wilson, A. Vitkin, and V. X. D. Yang, "Optimized speckle variance OCT imaging of microvasculature," Opt. Lett. **35**(8), 1257–1259 (2010).
24. Y. Jia, O. Tan, J. Tokayer, B. Potsaid, Y. Wang, J. J. Liu, M. F. Kraus, H. Subhash, J. G. Fujimoto, J. Hornegger, and D. Huang, "Split-spectrum amplitude-decorrelation angiography with optical coherence tomography," Opt. Express **20**(4), 4710–4725 (2012).
25. J. Fingler, D. Schwartz, C. Yang, and S. E. Fraser, "Mobility and transverse flow visualization using phase variance contrast with spectral domain optical coherence tomography," Opt. Express **15**(20), 12636–12653 (2007).
26. R. K. Wang, S. L. Jacques, Z. Ma, S. Hurst, S. R. Hanson, and A. Gruber, "Three dimensional optical angiography," Opt. Express **15**(7), 4083–4097 (2007).

27. R. A. Costa, M. Skaf, L. A. S. Melo, D. Calucci, J. A. Cardillo, J. C. Castro, D. Huang, and M. Wojtkowski, "Retinal assessment using optical coherence tomography," Prog. Retin. Eye Res. **25**(3), 325–353 (2006).
28. J. Fujimoto and E. Swanson, "The development, commercialization, and impact of optical coherence tomography," Invest. Ophthalmol. Vis. Sci. **57**(9), OCT1–OCT13 (2016).
29. J. F. De Boer, R. Leitgeb, and M. Wojtkowski, "Twenty-five years of optical coherence tomography: the paradigm shift in sensitivity and speed provided by Fourier domain OCT [Invited]," Biomed. Opt. Express **8**(7), 3248–3280 (2017).
30. T. S. Hwang, M. Zhang, K. Bhavsar, X. Zhang, J. P. Campbell, P. Lin, S. T. Bailey, C. J. Flaxel, A. K. Lauer, D. J. Wilson, D. Huang, and Y. Jia, "Visualization of 3 distinct retinal plexuses by projection-resolved optical coherence tomography angiography in diabetic retinopathy," JAMA Ophthalmol. **134**(12), 1411–1419 (2016).
31. T. S. Hwang, S. S. Gao, L. Liu, A. K. Lauer, S. T. Bailey, C. J. Flaxel, D. J. Wilson, D. Huang, and Y. Jia, "Automated quantification of capillary nonperfusion using optical coherence tomography angiography in diabetic retinopathy," JAMA Ophthalmol. **134**(4), 367–373 (2016).
32. J. P. Campbell, M. Zhang, T. S. Hwang, S. T. Bailey, D. J. Wilson, Y. Jia, and D. Huang, "Detailed vascular anatomy of the human retina by projection-resolved optical coherence tomography angiography," Sci. Rep. **7**, 42201 (2017).
33. T. T. Hormel, Y. Jia, Y. Jian, T. S. Hwang, S. T. Bailey, M. E. Pennesi, D. J. Wilson, J. C. Morrison, and D. Huang, "Plexus-specific retinal vascular anatomy and pathologies as seen by projection-resolved optical coherence tomographic angiography," Prog. Retin. Eye Res. **80**, 100878 (2021).
34. S. Makita, Y. Hong, M. Yamanari, T. Yatagai, and Y. Yasuno, "Optical coherence angiography," Opt. Express **14**(17), 7821–7840 (2006).
35. N. J. Crane, S. W. Huffman, M. Alemozaffar, F. A. Gage, I. W. Levin, and E. A. Elster, "Evidence of a heterogeneous tissue oxygenation: renal ischemia/reperfusion injury in a large animal model," J. Biomed. Opt. **18**(3), 035001 (2013).
36. S. H. Chavala, S. Farsiu, R. Maldonado, D. K. Wallace, S. F. Freedman, and C. A. Toth, "Insights into advanced retinopathy of prematurity using handheld spectral domain optical coherence tomography imaging," Ophthalmology **116**(12), 2448–2456 (2009).
37. A. C. Lee, R. S. Maldonado, N. Sarin, R. V. O'Connell, D. K. Wallace, S. F. Freedman, M. Cotten, and C. A. Toth, "Macular features from spectral-domain optical coherence tomography as an adjunct to indirect ophthalmoscopy in retinopathy of prematurity," Retina **31**(8), 1470–1482 (2011).
38. M. I. Seider, D. S. Grewal, and P. Mruthyunjaya, "Portable optical coherence tomography detection or confirmation of ophthalmoscopically invisible or indeterminate active retinoblastoma," Ophthalmic Surg. Lasers Imaging Retina **47**(10), 965–968 (2016).
39. K. Zhou, S. Song, A. Legocki, Y. Cheng, L. Ding, K. A. Rezaei, R. K. Wang, and M. T. Cabrera, "Quantitative handheld swept-source optical coherence tomography angiography in awake preterm and full-term infants," Transl. Vis. Sci. Technol. **9**(13), 19 (2020).
40. F. LaRocca, D. Nankivil, S. Farsiu, and J. A. Izatt, "Handheld simultaneous scanning laser ophthalmoscopy and optical coherence tomography system," Biomed. Opt. Express **4**(11), 2307–2321 (2013).
41. Y. Jian, R. J. Zawadzki, and M. V. Sarunic, "Adaptive optics optical coherence tomography for in vivo mouse retinal imaging," J. Biomed. Opt. **18**(5), 56007 (2013).

42. X. Wei, T. T. Hormel, Y. Guo, and Y. Jia, "75-degree non-mydriatic single-volume optical coherence tomographic angiography," Biomed. Opt. Express **10**(12), 6286–6295 (2019).
43. J. Polans, B. Keller, O. M. Carrasco-Zevallos, F. LaRocca, E. Cole, H. E. Whitson, E. M. Lad, S. Farsiu, and J. A. Izatt, "Wide-field retinal optical coherence tomography with wavefront sensorless adaptive optics for enhanced imaging of targeted regions," Biomed. Opt. Express **8**(1), 16–37 (2016).
44. M. J. Ju, M. Heisler, A. Athwal, M. V. Sarunic, and Y. Jian, "Effective bidirectional scanning pattern for optical coherence tomography angiography," Biomed. Opt. Express **9**(5), 2336–2350 (2018).
45. X. Wei, T. T. Hormel, S. Pi, Y. Guo, Y. Jian, and Y. Jia, "High dynamic range optical coherence tomography angiography (HDR-OCTA)," Biomed. Opt. Express **10**(7), 3560–3571 (2019).
46. Y. Jia, S. T. Bailey, T. S. Hwang, S. M. McClintic, S. S. Gao, M. E. Pennesi, C. J. Flaxel, A. K. Lauer, D. J. Wilson, J. Hornegger, J. G. Fujimoto, and D. Huang, "Quantitative optical coherence tomography angiography of vascular abnormalities in the living human eye," Proc. Natl. Acad. Sci. U.S.A **112**(18), E2395–E2402 (2015).
47. X. Wei, A. Camino, S. Pi, T. T. Hormel, W. Cepurna, D. Huang, J. C. Morrison, and Y. Jia, "Real-time cross-sectional and en face OCT angiography guiding high-quality scan acquisition," Opt. Lett. **44**(6), 1431–1434 (2019).
48. X. Wei, T. T. Hormel, Y. Guo, T. S. Hwang, and Y. Jia, "High-resolution wide-field OCT angiography with a self-navigation method to correct microsaccades and blinks," Biomed. Opt. Express **11**(6), 3234–3245 (2020).
49. Y. Jian, K. Wong, and M. V. Sarunic, "Graphics processing unit accelerated optical coherence tomography processing at megahertz axial scan rate and high resolution video rate volumetric rendering," J. Biomed. Opt. **18**(2), 26002 (2013).
50. J. Xu, K. Wong, Y. Jian, and M. V. Sarunic, "Real-time acquisition and display of flow contrast using speckle variance optical coherence tomography in a graphics processing unit," J. Biomed. Opt. **19**(2), 026001 (2014).
51. A. Camino, R. Ng, J. Huang, Y. Guo, S. Ni, Y. Jia, D. Huang, and Y. Jian, "Depth-resolved optimization of a real-time sensorless adaptive optics optical coherence tomography," Opt. Lett. **45**(9), 2612–2615 (2020).
52. American National Standard Institute, "Ophthalmics - light hazard protection for ophthalmic instruments," ANSI Z80.36 (2021).
53. International Committee for the Classification of Retinopathy of Prematurity, "The international classification of retinopathy of prematurity revisited," Arch. Ophthalmol. **123**(7), 991–999 (2005).
54. S. K. Sikkink, S. Biswas, N. R. A. Parry, P. E. Stanga, and D. Trump, "X-linked retinoschisis: an update," J. Med. Genet. **44**(4), 225–232 (2007).
55. R. A. Avery, E. I. Hwang, H. Ishikawa, M. T. Acosta, K. A. Hutcheson, D. Santos, D. J. Zand, L. B. Kilburn, K. N. Rosenbaum, B. R. Rood, J. S. Schuman, and R. J. Packer, "Handheld optical coherence tomography during sedation in young children with optic pathway gliomas," JAMA Ophthalmol. **132**(3), 265–271 (2014).
56. R. S. Maldonado, J. A. Izatt, N. Sarin, D. K. Wallace, S. Freedman, C. M. Cotten, and C. A. Toth, "Optimizing hand-held spectral domain optical coherence tomography imaging for neonates, infants, and children," Invest. Ophthalmol. Vis. Sci. **51**(5), 2678–2685 (2010).

57. D. Demian, V.-F. Duma, C. Sinescu, M. L. Negrutiu, R. Cernat, F. I. Topala, G. Hutiu, A. Bradu, and A. G. Podoleanu, "Design and testing of prototype handheld scanning probes for optical coherence tomography," Proc. Inst. Mech. Eng. **228**(8), 743–753 (2014).
58. G. L. Monroy, J. Won, D. R. Spillman, R. Dsouza, and S. A. Boppart, "Clinical translation of handheld optical coherence tomography: practical considerations and recent advancements," J. Biomed. Opt. **22**(12), 1–30 (2017).
59. J. Polans, D. Cunefare, E. Cole, B. Keller, P. S. Mettu, S. W. Cousins, M. J. Allingham, J. A. Izatt, and S. Farsiu, "Enhanced visualization of peripheral retinal vasculature with wavefront sensorless adaptive optics optical coherence tomography angiography in diabetic patients," Opt. Lett. **42**(1), 17–20 (2017).
60. A. Camino, P. Zang, A. Athwal, S. Ni, Y. Jia, D. Huang, and Y. Jian, "Sensorless adaptive-optics optical coherence tomographic angiography," Biomed. Opt. Express **11**(7), 3952–3967 (2020).
61. K. S. K. Wong, Y. Jian, M. Cua, S. Bonora, R. J. Zawadzki, and M. V. Sarunic, "In vivo imaging of human photoreceptor mosaic with wavefront sensorless adaptive optics optical coherence tomography," Biomed. Opt. Express **6**(2), 580–590 (2015).
62. Y. Jian, S. Lee, M. J. Ju, M. Heisler, W. Ding, R. J. Zawadzki, S. Bonora, and M. V. Sarunic, "Lens-based wavefront sensorless adaptive optics swept source OCT," Sci. Rep. **6**(1), 27620 (2016).
63. H. R. G. W. Verstraete, M. Heisler, M. J. Ju, D. Wahl, L. Bliek, J. Kalkman, S. Bonora, Y. Jian, M. Verhaegen, and M. V. Sarunic, "Wavefront sensorless adaptive optics OCT with the DONE algorithm for in vivo human retinal imaging [Invited]," Biomed. Opt. Express **8**(4), 2261–2275 (2017).
64. M. J. Ju, M. Heisler, D. Wahl, Y. Jian, and M. V. Sarunic, "Multiscale sensorless adaptive optics OCT angiography system for in vivo human retinal imaging," J. Biomed. Opt. **22**(12), 121703 (2017).
65. T. DuBose, D. Nankivil, F. LaRocca, G. Waterman, K. Hagan, J. Polans, B. Keller, D. Tran-Viet, L. Vajzovic, A. N. Kuo, C. A. Toth, J. A. Izatt, and S. Farsiu, "Handheld adaptive optics scanning laser ophthalmoscope," Optica **5**(9), 1027–1036 (2018).
66. M. Heisler, S. Lee, Z. Mammo, Y. Jian, M. Ju, A. Merkur, E. Navajas, C. Balaratnasingam, M. F. Beg, and M. V. Sarunic, "Strip-based registration of serially acquired optical coherence tomography angiography," J. Biomed. Opt. **22**(3), 36007 (2017).
67. S. Borkovkina, A. Camino, W. Janpongsri, M. V. Sarunic, and Y. Jian, "Real-time retinal layer segmentation of OCT volumes with GPU accelerated inferencing using a compressed, low-latency neural network," Biomed. Opt. Express **11**(7), 3968–3984 (2020).
68. C. Gilbert and A. Foster, "Childhood blindness in the context of VISION 2020--the right to sight," Bull. World Health Organ. **79**(3), 227–232 (2001).
69. S. Ni, X. Wei, R. Ng, S. Ostmo, M. F. Chiang, D. Huang, Y. Jia, J. P. Campbell, and Y. Jian, "High-speed and widefield handheld swept-source OCT angiography with a VCSEL light source," Biomed. Opt. Express **12**(6), 3553–3570 (2021).
70. O. M. Carrasco-Zevallos, C. Viehland, B. Keller, R. P. McNabb, A. N. Kuo, and J. A. Izatt, "Constant linear velocity spiral scanning for near video rate 4D OCT ophthalmic and surgical imaging with isotropic transverse sampling," Biomed. Opt. Express **9**(10), 5052–5070 (2018).
71. B. A. Scruggs, S. Ni, T.-T. P. Nguyen, S. Ostmo, M. F. Chiang, Y. Jia, D. Huang, Y. Jian, and J. P. Campbell, "Peripheral OCT assisted by scleral depression in retinopathy of prematurity," Ophthalmology Science **2**(1), 100094 (2022).

72. Y. Miao, M. Siadati, J. Song, D. Ma, Y. Jian, M. F. Beg, M. V. Sarunic, and M. J. Ju, "Phase-corrected buffer averaging for enhanced OCT angiography using FDML laser," Opt. Lett. **46**(16), 3833–3836 (2021).
73. J. P. Kolb, T. Klein, C. L. Kufner, W. Wieser, A. S. Neubauer, and R. Huber, "Ultra-widefield retinal MHz-OCT imaging with up to 100 degrees viewing angle," Biomed. Opt. Express **6**(5), 1534–1552 (2015).
74. J. G. Fujimoto, E. A. Swanson, and D. Huang, "Optical coherence tomography-history, evolution, and future prospects: 2023 Lasker-DeBakey Clinical Medical Research Award," JAMA **330**(15), 1427–1428 (2023).
75. N. Choudhry, J. Golding, M. W. Manry, and R. C. Rao, "Ultra-widefield steering-based spectral-domain optical coherence tomography imaging of the retinal periphery," Ophthalmology **123**(6), 1368–1374 (2016).
76. T.-T. P. Nguyen, S. Ni, S. Khan, X. Wei, S. Ostmo, M. F. Chiang, Y. Jia, D. Huang, Y. Jian, and J. P. Campbell, "Advantages of widefield optical coherence tomography in the diagnosis of retinopathy of prematurity," Front. Pediatr. **9**, 797684 (2021).
77. T.-T. P. Nguyen, S. Ni, S. Ostmo, A. Rajagopalan, A. S. Coyner, M. Woodward, M. F. Chiang, Y. Jia, D. Huang, J. P. Campbell, and Y. Jian, "Association of optical coherence tomography–measured fibrovascular ridge thickness and clinical disease stage in retinopathy of prematurity," JAMA Ophthalmol. **140**(11), 1121–1127 (2022).
78. T.-T. P. Nguyen, S. Ni, G. Liang, S. Khan, X. Wei, A. Skalet, S. Ostmo, M. F. Chiang, Y. Jia, D. Huang, Y. Jian, and J. P. Campbell, "Widefield optical coherence tomography in pediatric retina: a case series of intraoperative applications using a prototype handheld device," Front. Med. **9**, 860371 (2022).
79. S. Ni, T.-T. P. Nguyen, R. Ng, S. Khan, S. Ostmo, Y. Jia, M. F. Chiang, D. Huang, J. P. Campbell, and Y. Jian, "105° field of view non-contact handheld swept-source optical coherence tomography," Opt. Lett. **46**(23), 5878–5881 (2021).
80. S. Ni, T.-T. P. Nguyen, R. Ng, M. Woodward, S. Ostmo, Y. Jia, M. F. Chiang, D. Huang, A. H. Skalet, J. P. Campbell, and Y. Jian, "Panretinal Optical Coherence Tomography," IEEE Trans. Med. Imaging **42**(11), 3219–3228 (2023).
81. A. S. Neubauer, M. Kernt, C. Haritoglou, S. G. Priglinger, A. Kampik, and M. W. Ulbig, "Nonmydriatic screening for diabetic retinopathy by ultra-widefield scanning laser ophthalmoscopy (Optomap)," Graefe's Arch. Clin. Exp. Ophthalmol. **246**(2), 229–235 (2008).
82. M. S. Oğüt, N. Bozkurt, E. Ozek, H. Birgen, H. Kazokoğlú, and M. Oğüt, "Effects and side effects of mydriatic eyedrops in neonates," Eur. J. Ophthalmol. **6**(2), 192–196 (1996).
83. S. Ni, G. B. Liang, R. Ng, S. Ostmo, Y. Jia, M. F. Chiang, D. Huang, A. H. Skalet, B. K. Young, J. P. Campbell, and Y. Jian, "Panretinal handheld OCT angiography for pediatric retinal imaging," Biomed. Opt. Express **15**(5), 3412–3424 (2024).
84. D. A. Atchison and L. N. Thibos, "Optical models of the human eye," Clin. Exp. Optom. **99**(2), 99–106 (2016).
85. W. N. Charman and H. Radhakrishnan, "Accommodation, pupil diameter and myopia," Ophthalmic Physiol. Opt. **29**(1), 72–79 (2009).
86. R. J. Zawadzki, S. M. Jones, S. S. Olivier, M. Zhao, B. A. Bower, J. A. Izatt, S. Choi, S. Laut, and J. S. Werner, "Adaptive-optics optical coherence tomography for high-resolution and high-speed 3D retinal in vivo imaging," Opt. Express **13**(21), 8532–8546 (2005).

87. Y. Jian, J. Xu, M. A. Gradowski, S. Bonora, R. J. Zawadzki, and M. V. Sarunic, "Wavefront sensorless adaptive optics optical coherence tomography for in vivo retinal imaging in mice," Biomed. Opt. Express **5**(2), 547–559 (2014).
88. J. Polans, B. Jaeken, R. P. McNabb, P. Artal, and J. A. Izatt, "Wide-field optical model of the human eye with asymmetrically tilted and decentered lens that reproduces measured ocular aberrations," Optica **2**(2), 124–134 (2015).
89. N. Koulisis, S. N. Moysidis, Y. Yonekawa, Y. L. Dai, B. Burkemper, E. H. Wood, I. Lertjirachai, B. Todorich, T. Z. Khundkar, Z. Chu, R. K. Wang, G. A. Williams, K. A. Drenser, A. Capone, M. T. Trese, and E. Nudleman, "Correlating changes in the macular microvasculature and capillary network to peripheral vascular pathologic features in familial exudative vitreoretinopathy," Ophthalmol. Retina **3**(7), 597–606 (2019).
90. M. P. Blair, J. N. Ulrich, M. Elizabeth Hartnett, and M. J. Shapiro, "Peripheral retinal nonperfusion in fellow eyes in coats disease," Retina **33**(8), 1694–1699 (2013).
91. S. K. Wang, N. F. Callaway, M. B. Wallenstein, M. T. Henderson, T. Leng, and D. M. Moshfeghi, "SUNDROP: six years of screening for retinopathy of prematurity with telemedicine," Can. J. Ophthalmol. **50**(2), 101–106 (2015).
92. C. J. Brady, S. D'Amico, and J. P. Campbell, "Telemedicine for Retinopathy of Prematurity," Telemed. J. E Health **26**(4), 556–564 (2020).
93. L. Ginner, C. Blatter, D. Fechtig, T. Schmoll, M. Gröschl, and R. A. Leitgeb, "Wide-Field OCT Angiography at 400 KHz Utilizing Spectral Splitting," Photonics **1**(4), 369–379 (2014).
94. R. Goyal, R. V. North, and J. E. Morgan, "Comparison of laser interferometry and ultrasound A-scan in the measurement of axial length," Acta Ophthalmol. Scand. **81**(4), 331–335 (2003).
95. A. C. Lee, M. A. Qazi, and J. S. Pepose, "Biometry and intraocular lens power calculation," Curr. Opin. Ophthalmol. **19**(1), 13–17 (2008).
96. M. Ruggeri, S. R. Uhlhorn, C. De Freitas, A. Ho, F. Manns, and J.-M. Parel, "Imaging and full-length biometry of the eye during accommodation using spectral domain OCT with an optical switch," Biomed. Opt. Express **3**(7), 1506–1520 (2012).
97. H.-J. Kim, M. Kim, M. G. Hyeon, Y. Choi, and B.-M. Kim, "Full ocular biometry through dual-depth whole-eye optical coherence tomography," Biomed. Opt. Express **9**(2), 360–372 (2018).
98. D. E. Laws, R. Haslett, D. Ashby, C. O'Brien, and D. Clark, "Axial length biometry in infants with retinopathy of prematurity," Eye (Lond) **8**(4), 427–430 (1994).
99. T. Tang, Z. Yu, Q. Xu, Z. Peng, Y. Fan, K. Wang, Q. Ren, J. Qu, and M. Zhao, "A machine learning-based algorithm used to estimate the physiological elongation of ocular axial length in myopic children," Eye and Vision **7**(1), 50 (2020).
100. I. Grulkowski, J. J. Liu, J. Y. Zhang, B. Potsaid, V. Jayaraman, A. E. Cable, J. S. Duker, and J. G. Fujimoto, "Reproducibility of a long-range swept-source optical coherence tomography ocular biometry system and comparison with clinical biometers," Ophthalmology **120**(11), 2184–2190 (2013).
101. W. Lotmar, "A theoretical model for the eye of new-born infants," Albrecht Von Graefes Arch. Klin. Exp. Ophthalmol. **198**(2), 179–185 (1976).
102. W. Haigis, B. Lege, N. Miller, and B. Schneider, "Comparison of immersion ultrasound biometry and partial coherence interferometry for intraocular lens calculation according to Haigis," Graefes Arch. Clin. Exp. Ophthalmol. **238**(9), 765–773 (2000).
103. M. F. Chiang, G. E. Quinn, A. R. Fielder, S. R. Ostmo, R. V. P. Chan, A. Berrocal, G. Binenbaum, M. Blair, J. P. Campbell, A. Capone, Y. Chen, S. Dai, A. Ells, B. W. Fleck, W.

V. Good, M. E. Hartnett, G. Holmstrom, S. Kusaka, A. Kychenthal, D. Lepore, B. Lorenz, M. A. Martinez-Castellanos, Ş. Özdek, D. Ademola-Popoola, J. D. Reynolds, P. K. Shah, M. Shapiro, A. Stahl, C. Toth, A. Vinekar, L. Visser, D. K. Wallace, W.-C. Wu, P. Zhao, and A. Zin, "International classification of retinopathy of prematurity, Third Edition," Ophthalmology **128**(10), e51–e68 (2021).

104. M. M. Joshi, M. T. Trese, and A. Capone, "Optical coherence tomography findings in stage 4A retinopathy of prematurity: a theory for visual variability," Ophthalmology **113**(4), 657–660 (2006).
105. T.-T. P. Nguyen, S. Ni, S. Khan, X. Wei, S. R. Ostmo, M. F. Chiang, Y. Jia, D. Huang, Y. Jian, and J. P. Campbell, "Quantification of fibrovascular ridge thickness in retinopathy of prematurity using swept-source optical coherence tomography," Invest. Ophthalmol. Vis. Sci. **63**(7), 802 (2022).
106. R. F. Spaide, "Peripheral areas of nonperfusion in treated central retinal vein occlusion as imaged by wide-field fluorescein angiography," Retina **31**(5), 829–837 (2011).
107. M. Kernt, I. Hadi, F. Pinter, F. Seidensticker, C. Hirneiss, C. Haritoglou, A. Kampik, M. W. Ulbig, and A. S. Neubauer, "Assessment of diabetic retinopathy using nonmydriatic ultra-widefield scanning laser ophthalmoscopy (Optomap) compared with ETDRS 7-field stereo photography," Diabetes Care **35**(12), 2459–2463 (2012).
108. C. S. Tan, F. Heussen, and S. R. Sadda, "Peripheral autofluorescence and clinical findings in neovascular and non-neovascular age-related macular degeneration," Ophthalmology **120**(6), 1271–1277 (2013).
109. M. Siddiqui, A. S. Nam, S. Tozburun, N. Lippok, C. Blatter, and B. J. Vakoc, "High-speed optical coherence tomography by circular interferometric ranging," Nat. Photonics **12**(2), 111–116 (2018).
110. S. Makita, M. Miura, S. Azuma, T. Mino, T. Yamaguchi, and Y. Yasuno, "Accurately motion-corrected Lissajous OCT with multi-type image registration," Biomed. Opt. Express **12**(1), 637–653 (2021).
111. S. Makita, S. Azuma, T. Mino, T. Yamaguchi, M. Miura, and Y. Yasuno, "Extending field-of-view of retinal imaging by optical coherence tomography using convolutional Lissajous and slow scan patterns," Biomed. Opt. Express **13**(10), 5212–5230 (2022).
112. Z. Duan, K. Huang, Z. Luo, K. Ma, G. Wang, X. Hu, J. Zhang, X. Luo, Y. Huang, G. Liu, X. Ding, P. Xiao, and J. Yuan, "Portable boom-type ultrahigh-resolution OCT with an integrated imaging probe for supine position retinal imaging," Biomed. Opt. Express **13**(6), 3295–3310 (2022).
113. A. L. Solebo, L. Teoh, and J. Rahi, "Epidemiology of blindness in children," Arch. Dis. Child. **102**(9), 853–857 (2017).
114. T. Chan-Ling, G. A. Gole, G. E. Quinn, S. J. Adamson, and B. A. Darlow, "Pathophysiology, screening and treatment of ROP: A multi-disciplinary perspective," Prog. Retin. Eye Res. **62**, 77–119 (2018).
115. Cryotherapy for Retinopathy of Prematurity Cooperative Group, "Multicenter trial of cryotherapy for retinopathy of prematurity," Arch. Ophthalmol. **106**(4), 471–479 (1988).
116. Early Treatment For Retinopathy Of Prematurity Cooperative Group, "Revised indications for the treatment of retinopathy of prematurity: results of the early treatment for retinopathy of prematurity randomized trial," Arch. Ophthalmol. **121**(12), 1684–1694 (2003).
117. C. Gilbert, "Retinopathy of prematurity: a global perspective of the epidemics, population of babies at risk and implications for control," Early Hum. Dev. **84**(2), 77–82 (2008).

118. H. A. Mintz-Hittner, K. A. Kennedy, A. Z. Chuang, and BEAT-ROP Cooperative Group, "Efficacy of intravitreal bevacizumab for stage 3+ retinopathy of prematurity," N. Engl. J. Med. **364**(7), 603–615 (2011).
119. S. J. Kim, A. D. Port, R. Swan, J. P. Campbell, R. V. P. Chan, and M. F. Chiang, "Retinopathy of prematurity: a review of risk factors and their clinical significance," Surv. Ophthalmol. **63**(5), 618–637 (2018).
120. X. Chen, R. Imperio, C. Viehland, P. R. Patel, D. Tran-Viet, S. Mangalesh, S. G. Prakalapakorn, S. F. Freedman, J. A. Izatt, and C. A. Toth, "A pilot optical coherence tomography angiography classification of retinal neovascularization in retinopathy of prematurity," Sci. Rep. **14**(1), 568 (2024).
121. S. Ni, T.-T. P. Nguyen, R. Ng, S. Ostmo, Y. Jia, M. F. Chiang, D. Huang, A. H. Skalet, J. P. Campbell, and Y. Jian, "140° field-of-view contact handheld swept-source OCT for pediatric peripheral imaging," in *Ophthalmic Technologies XXXIII* (SPIE, 2023), **12360**, pp. 82–85.
122. S. Ni, T.-T. P. Nguyen, R. Ng, S. Khan, S. Ostmo, Y. Jia, M. F. Chiange, D. Huang, J. P. Campbell, and Y. Jian, "Ultra-widefield handheld swept-source OCT for peripheral retinal imaging," in *Ophthalmic Technologies XXXII* (SPIE, 2022), **11941**, pp. 25–28.
123. Y. Guo, A. Camino, M. Zhang, J. Wang, D. Huang, T. Hwang, and Y. Jia, "Automated segmentation of retinal layer boundaries and capillary plexuses in wide-field optical coherence tomographic angiography," Biomed. Opt. Express **9**(9), 4429–4442 (2018).
124. Y. Guo, T. T. Hormel, S. Pi, X. Wei, M. Gao, J. C. Morrison, and Y. Jia, "An end-to-end network for segmenting the vasculature of three retinal capillary plexuses from OCT angiographic volumes," Biomed. Opt. Express **12**(8), 4889–4900 (2021).
125. J. D. Reynolds, V. Dobson, G. E. Quinn, A. R. Fielder, E. A. Palmer, R. A. Saunders, R. J. Hardy, D. L. Phelps, J. D. Baker, M. T. Trese, D. Schaffer, B. Tung, and CRYO-ROP and LIGHT-ROP Cooperative Study Groups, "Evidence-based screening criteria for retinopathy of prematurity: natural history data from the CRYO-ROP and LIGHT-ROP studies," Arch. Ophthalmol. **120**(11), 1470–1476 (2002).
126. C. Gilbert, A. N. J. Malik, N. Nahar, S. K. Das, L. Visser, S. Sitati, and D. S. Ademola-Popoola, "Epidemiology of ROP update - Africa is the new frontier," Semin. Perinatol. **43**(6), 317–322 (2019).
127. "An international classification of retinopathy of prematurity. The Committee for the Classification of Retinopathy of Prematurity," Arch. Ophthalmol. **102**(8), 1130–1134 (1984).
128. S. Mangalesh, N. Sarin, B. McGeehan, S. G. Prakalapakorn, D. Tran-Viet, C. M. Cotten, S. F. Freedman, M. G. Maguire, C. A. Toth, and BabySTEPS Group, "Preterm infant stress during handheld optical coherence tomography vs binocular Indirect ophthalmoscopy examination for retinopathy of prematurity," JAMA Ophthalmol. **139**(5), 567–574 (2021).
129. W. M. Fierson, American Academy of Pediatrics Section on Ophthalmology, American Academy of Ophthalmology, American Association for Pediatric Ophthalmology and Strabismus, and American Association of Certified Orthoptists, "Screening examination of premature infants for retinopathy of prematurity," Pediatrics **142**(6), e20183061 (2018).
130. H. Degirmencioglu, M. Y. Oncel, E. Calisici, B. Say, N. Uras, and U. Dilmen, "Transient ileus associated with the use of mydriatics after screening for retinopathy of prematurity in a very low birth weight infant," J. Pediatr. Ophthalmol. Strabismus **51 Online**, e44-47 (2014).

131. T. R. Rosenblatt, M. H. Ji, D. Vail, C. A. Ludwig, A. Al-Moujahed, M. V. Pasricha, N. F. Callaway, J. Kumm, and D. M. Moshfeghi, "Key factors in a rigorous longitudinal image-based assessment of retinopathy of prematurity," Sci. Rep. **11**(1), 5369 (2021).
132. H. Dimaras, K. Kimani, E. A. Dimba, P. Gronsdahl, A. White, H. S. Chan, and B. L. Gallie, "Retinoblastoma," The Lancet **379**(9824), 1436–1446 (2012).
133. H. Dimaras, T. W. Corson, D. Cobrinik, A. White, J. Zhao, F. L. Munier, D. H. Abramson, C. L. Shields, G. L. Chantada, F. Njuguna, and B. L. Gallie, "Retinoblastoma," Nat. Rev. Dis. Primers **1**(1), 1–23 (2015).
134. Global Retinoblastoma Study Group, "Global retinoblastoma presentation and analysis by National Income Level," JAMA Oncol. **6**(5), 685–695 (2020).
135. Global Retinoblastoma Study Group, "The global retinoblastoma outcome study: a prospective, cluster-based analysis of 4064 patients from 149 countries," Lancet Glob. Health **10**(8), e1128–e1140 (2022).
136. T. Kivelä, "The epidemiological challenge of the most frequent eye cancer: retinoblastoma, an issue of birth and death," Br. J. Ophthalmol. **93**(9), 1129–1131 (2009).
137. B. A. King, C. Parra, Y. Li, K. J. Helton, I. Qaddoumi, M. W. Wilson, and R. J. Ogg, "Spatiotemporal patterns of tumor occurrence in children with intraocular retinoblastoma," PLoS One **10**(7), e0132932 (2015).
138. P. de Graaf, S. Göricke, F. Rodjan, P. Galluzzi, P. Maeder, J. A. Castelijns, and H. J. Brisse, "Guidelines for imaging retinoblastoma: imaging principles and MRI standardization," Pediatr. Radiol. **42**(1), 2–14 (2012).
139. I. Aerts, L. Lumbroso-Le Rouic, M. Gauthier-Villars, H. Brisse, F. Doz, and L. Desjardins, "Retinoblastoma," Orphanet J. Rare Dis. **1**, 31 (2006).
140. L. M. Vasquez, G. P. Giuliari, W. Halliday, C. J. Pavlin, B. L. Gallie, and E. Héon, "Ultrasound biomicroscopy in the management of retinoblastoma," Eye (Lond) **25**(2), 141–147 (2011).
141. D. H. Abramson, A. C. Schefler, K. L. Beaverson, I. S. Rollins, M. S. Ruddat, and C. J. Kelly, "Rapid growth of retinoblastoma in a premature twin," Arch. Ophthalmol. **120**(9), 1232–1233 (2002).
142. J. L. Berry, D. Cobrinik, and J. W. Kim, "Detection and intraretinal localization of an 'invisible' retinoblastoma using optical coherence tomography," Ocul. Oncol. Pathol. **2**(3), 148–152 (2016).
143. S. E. Soliman, C. VandenHoven, L. D. MacKeen, E. Héon, and B. L. Gallie, "Optical coherence tomography-guided decisions in retinoblastoma management," Ophthalmology **124**(6), 859–872 (2017).
144. S. E. Soliman, C. VandenHoven, L. D. MacKeen, and B. L. Gallie, "Secondary prevention of Retinoblastoma Revisited: Laser Photocoagulation of Invisible New Retinoblastoma," Ophthalmology **127**(1), 122–127 (2020).
145. M. F. Goldberg, "The skin is not the predominant problem in incontinentia pigmenti," Arch. Dermatol. **140**(6), 748–750 (2004).
146. M. F. Goldberg and P. H. Custis, "Retinal and other manifestations of incontinentia pigmenti (Bloch-Sulzberger syndrome)," Ophthalmology **100**(11), 1645–1654 (1993).
147. R. C. Watzke, T. S. Stevens, and R. G. Carney, "Retinal vascular changes of incontinentia pigmenti," Arch. Ophthalmol. **94**(5), 743–746 (1976).
148. M. Sen, C. L. Shields, S. G. Honavar, and J. A. Shields, "Coats disease: An overview of classification, management and outcomes," Indian J. Ophthalmol. **67**(6), 763–771 (2019).

149. S. Ni, R. Ng, D. Huang, S. Chen, B. K. Young, J. P. Campbell, and Y. Jian, "Non-mydriatic ultra-widefield diffraction-limited retinal imaging," Opt. Lett. **49**(14), 3902–3905 (2024).
150. N. Lippok and B. J. Vakoc, "Resolving absolute depth in circular-ranging optical coherence tomography by using a degenerate frequency comb," Opt. Lett., OL **45**(2), 371–374 (2020).
151. B. E. Bouma, J. F. de Boer, D. Huang, I. K. Jang, T. Yonetsu, C. L. Leggett, R. Leitgeb, D. D. Sampson, M. Suter, B. Vakoc, M. Villiger, and M. Wojtkowski, "Optical coherence tomography," Nat. Rev. Methods Primers **2**, 79 (2022).
152. R. Khazaeinezhad, M. Siddiqui, and B. J. Vakoc, "16 MHz wavelength-swept and wavelength-stepped laser architectures based on stretched-pulse active mode locking with a single continuously chirped fiber Bragg grating," Opt. Lett. **42**(10), 2046–2049 (2017).
153. N. Lippok, B. E. Bouma, and B. J. Vakoc, "Stable multi-megahertz circular-ranging optical coherence tomography at 1.3 μm," Biomed. Opt. Express **11**(1), 174–185 (2020).
154. B. Lee, S. Jeong, J. Lee, T. S. Kim, B. Braaf, B. J. Vakoc, and W.-Y. Oh, "Wide-field three-dimensional depth-invariant cellular-resolution imaging of the human retina," Small **19**(11), 2203357 (2023).